



Royal Netherlands  
Meteorological Institute  
*Ministry of Infrastructure and the  
Environment*

# Investigating MSG-SEVIRI data as an additional predictor source in the KNMI probabilistic (severe) thunderstorm forecasting system

Valentijn van Gastel

De Bilt, 2012 | Intern rapport; IR 2012-01



Investigating MSG-SEVIRI data as an  
additional predictor source in the KNMI  
probabilistic (severe) thunderstorm  
forecasting system

Versie 1.0

Datum December 2011  
Status Definitief



# **Investigating MSG-SEVIRI data as an additional predictor source in the KNMI probabilistic (severe) thunderstorm forecasting system**

Valentijn van Gastel

Master Thesis  
Utrecht University  
Meteorology, Physical Oceanography and Climate  
December 2011

Supervisors KNMI  
Dr. Maurice Schmeits  
Dr. Rob Roebeling\*

Supervisor IMAU  
Dr. Aarnout van Delden

\*Presently at EUMETSAT



Universiteit Utrecht



Koninklijk Nederlands  
Meteorologisch Instituut  
Ministerie van Infrastructuur en Milieu



## Abstract

Thunderstorms can be a serious threat to society. In the Netherlands, the Royal Netherlands Meteorological Institute (KNMI) is responsible for issuing an extreme weather warning for severe thunderstorms, based on high total lightning intensity. To help forecasters decide whether they should issue an extreme weather warning, a Model Output Statistics (MOS) system was developed. This system uses logistic regression equations to predict both the probability of thunderstorms and the conditional probability of severe thunderstorms for twelve regions of 90 by 80 km<sup>2</sup> over the Netherlands, and makes forecasts for 6-h periods up to 2 days ahead. Predictors are obtained from ECMWF and HIRLAM model output and from ensembles of advected radar and lightning data, the latter only for the 0-6 h forecasts. The system has been operational since 2006 and runs during the warm half year, from mid-April to mid-October.

In this study we investigate an ensemble of Meteosat Second Generation (MSG) data as an additional predictor source for the 0–6 h projections of the MOS thunderstorm forecasting system. Cloud Physical Properties (CPPs), which are derived from MSG data, are advected using vectors derived from previous MSG images. Varying the magnitude and direction of these vectors creates the ensemble. A description is given of the relations between CPP and lightning intensity. Predictors are created based on these relations and investigated as additional potential predictors in the system, besides those used in the current system. CPP predictors are included in 4 of the 8 severe thunderstorm forecast equations. Equations including these predictors generally improve the forecast skill of the system compared to forecast equations without CPP predictors and the (updated) operational system. Another advantage of the new severe thunderstorm forecast equations arises due to their derivation using extended logistic regression. Forecasts can be made using the new system for any arbitrarily chosen lightning intensity threshold. The forecasts prove to be skillful up to very high lightning intensities, much higher than those used in the currently operational forecasting system. The new MOS system currently runs experimentally at KNMI and will become operational if it improves forecast skill over the coming year.



# Contents

<b>1. Introduction</b>	<b>6</b>
<b>2. Theoretical background</b>	<b>8</b>
2.1 Fundamental concepts	8
2.1.1 Cloud formation	8
2.1.2 Convection	9
2.1.3 Buoyancy and cloud particles	10
2.1.4 Favourable conditions for thunderstorm development	11
2.2 Ordinary thunderstorms	12
2.3 Classification of thunderstorms	13
2.4 Lightning and storm electricity	14
2.5 Thunderstorm climatology of the Netherlands	15
<b>3. Remote sensing of clouds, precipitation and lightning</b>	<b>16</b>
3.1 Radiation	16
3.1.1 Radiation basics	17
3.1.2 The global radiation balance	17
3.1.3 The effect of clouds on radiation	18
3.2 Remote sensing of clouds using satellites	19
3.3 Remote sensing using weather radar	21
3.4 Lightning detection	22
<b>4. Data and Methods</b>	<b>23</b>
4.1 Model Output Statistics	23
4.2 The predictand	25
4.3 Potential predictors	26
4.3.1 Numerical Weather Prediction model data	26
4.3.2 Ensemble of advected radar and lightning data	27
4.3.3 Ensemble of advected MSG data	27
4.4 Verification techniques	29
4.4.1 The reliability diagram	29
4.4.2 The Brier (skill) score	30
<b>5. Results</b>	<b>32</b>
5.1 Relation between cloud physical properties and lightning intensity	32
5.2 Selected predictors	34
5.3 Example case: September 10, 2011	37
5.4 Verification over 2011	41
5.4.1 Verification results of the MOS thunderstorm forecasting system	42
5.4.2 Verification results of the MOS severe thunderstorm forecasting system	43
<b>6. Summary and Conclusions</b>	<b>50</b>
<b>References</b>	<b>52</b>
<b>Appendix 1: Predictor acronyms</b>	<b>58</b>
<b>Appendix 2: Predictor coefficients of the MOS (severe) thunderstorm system</b>	<b>54</b>
<b>Appendix 3: Reliability diagrams of the 03 and 18 UTC severe thunderstorm forecasts</b>	<b>60</b>
<b>Appendix 4: Reliability diagrams of the M5MI <math>\geq</math> 300, 400, 500 severe thunderstorm forecasts</b>	<b>63</b>



# 1. Introduction

In the Netherlands thunderstorms appear quite frequently during the late spring, summer and early autumn. Lightning, associated with thunderstorms, can be a threat to society. It may cause damage to property, electric utilities, endanger humans and livestock and is a threat to aviation. Thunderstorms are associated with deep moist convection. General ingredients for the initiation of thunderstorms are known to be: potential instability, high levels of moisture in the atmospheric boundary layer and a source of lift to initiate convection (Johns and Doswell, 1992). The interaction between these conditions on different scales causes the formation of thunderstorms.

Forecasting thunderstorms is however one of the most difficult tasks for meteorologists, mainly due to the fact that lightning or lightning intensity is not available as direct Numerical Weather Prediction model output (Lilly, 1990). Meteorologists have however tried to assess thunderstorm risk since the late 1940's using parameters deduced from vertical temperature, moisture and wind profiles (Haklander and Van Delden, 2003). Initially these parameters have been calculated from rawinsonde data and were later derived from NWP model output. At KNMI, automated probabilistic forecasts have been developed from the beginning of the 1980's to predict the occurrence of a thunderstorm. The technique used to develop these forecast equations is referred to as Model Output Statistics (MOS) (Glahn and Lowry, 1972).

MOS improves on aspects of conventional NWP forecasts by post-processing raw NWP output (Wilks, 2006). The technique is based on multiple linear or logistic regression equations. Past values of a predictand to be forecast and a matching collection of potential predictors, which have to be known prior to the forecast time are required for the development of the equations. These predictors may come from historical observations, besides data from historical NWP forecasts. The predictand is a dichotomous event stating either 'yes' or 'no' whether the forecasted event has occurred. A forecasting procedure is developed using the set of historical data and can be used to forecast future values of the predictand on the basis of future predictor values.

As lightning intensity is not available as direct output from NWP models, MOS is considered to be a very useful technique to assess thunderstorm risk. The first MOS system developed at KNMI was used to predict the occurrence of a thunderstorm at one of ten observational stations in the Netherlands for a period of 0000-2400 UTC (Lemcke and Kruizinga, 1988). MOS forecast equations were derived using potential predictors from archived model forecasts of the European Centre for Medium-Range Weather Forecasts (ECMWF). A thunderstorm was said to have occurred if it had been reported within the period 0000 – 2400 UTC by at least one of ten stations in the Netherlands (the predictand).

As interest from society grew, a more sophisticated system was developed in 2004, referred to as INDECS (Schmeits et al., 2005). Remote sensor lightning observations had been operational for a number of years and it was now possible to use lightning data from the Surveillance et d'Alerte Foudre par Interférométrie (SAFIR) network as predictand (Wessels, 1998). This made it possible to make thunderstorm probability forecasts for regions of 90 km x 80 km over the Netherlands. Two predictands were defined for each region and time period: the probability of a thunderstorm event ( $\geq 2$  detected lightning discharges) and the conditional probability of a severe thunderstorm event ( $\geq 500$  detected lightning discharges), under the condition of a thunderstorm event. The potential predictor set consisted of indices computed from ECMWF model and High Resolution Local Area Modelling (HIRLAM) model data, the (co)sine of the day of the year and so called P27 scores (Kruizinga, 1979). The system increased temporal resolution to periods of 6 hours and made forecasts out to 48 hours in advance.

In 2006, an additional system was introduced, referred to as 'Kansverwachting Onweer ten behoeve van Uitgifte Weeralarm' (KOUW). In this new system, an 18-member ensemble of advected radar and lightning data was included as additional predictor sources for the 0-6 hour projections (Schmeits et al., 2008). Because of the addition of advected observations to the system, the runtime frequency of the system could be increased to 8 times a day. It was further different from the 2004 version in the

definition of severe thunderstorms. A severe thunderstorm was defined in KOUW under the condition of a thunderstorm event and included thresholds of 50, 100 and 200 detected lightning discharges in 5 minutes. KOUW runs out to 12 hours in advance at 6 hour time periods. INDECS and KOUW are currently operational at KNMI during the summer half year, from mid-April to mid-October.

For further development of KOUW, Schmeits et al. (2008) recommended to include Meteosat Second Generation (MSG) satellite data as an additional predictor source. MSG data could not be included during the initial development of KOUW as the MSG satellite has only been operational since 2004. MSG data has to date been available and archived for 7 years. This study addresses the recommendation made by Schmeits et al. (2008) and aims to improve the 0-6 hour projections of KOUW by including MSG data as an additional predictor source.

MSG products of interest to this study are Cloud Physical Properties (CPPs) derived from the Spinning Enhanced Visible and InfraRed Imager (SEVIRI) on board the MSG satellite (Roebeling, 2008). Cloud physical properties are retrieved using visible and near-infrared cloud reflectances and infrared cloud top temperatures, with Radiative Transfer Model (RTM) simulations and a CPP algorithm (Roebeling, 2008). The retrieval is done by the Satellite Application Facility on Climate Monitoring (SAF-CM), which was initiated by the European organisation for the exploitation of METeorological SATellites (EU-METSAT).

In 2009, a study at KNMI was devoted to the detection of Cb clouds, associated with thunderstorms, using CPPs (Carbajal et al., 2009). The results of this study were promising and show support to the idea of including MSG data for thunderstorm forecasting. In addition, previous studies have found strong relations between ice water content in clouds and thunderstorms (Petersen et al., 2006; Deierling et al., 2006). Ice water content can be derived from, or is associated with, several CPPs and it is thus expected that advected MSG data can improve the 0-6 h projections of KOUW. Furthermore, the range of MSG data around the Netherlands is substantially larger compared to lightning or radar data, making it possible to advect observations over longer distances. The main research question in this study is:

*Can predictors derived from an ensemble of advected MSG data improve the forecasting skill of the 0-6 hour thunderstorm forecasts of the current MOS system, operational at KNMI?*

New forecast equations are derived using data from the years 2008 – 2010. Verification is however done over a totally independent dataset of 2011. The forecast equations are compared to the operational forecast equations and forecast equations derived excluding MSG data to give an indication of the increase in forecast skill. Supplementary to the main research question, the following sub questions are addressed:

- *What is the relation between different cloud physical properties derived from MSG data and thunderstorms?*
- *How can advected cloud physical properties be used to forecast thunderstorms?*
- *Do thunderstorm forecasts including advected cloud physical properties have more skill compared to equations excluding advected cloud physical properties?*

The structure of this thesis is as follows. Chapter 2 provides important background information, needed to understand the formation and characteristics of thunderstorms. In chapter 3, the relevant remote sensing techniques are explained; the chapter presents useful background information on observational data used in this study. Remote sensing of clouds using satellite data is discussed but also remote sensing using weather radars and a lightning detection network. Chapter 4 presents how the data is used to create statistical thunderstorm forecasts, it explains the advection techniques and how the final equations are validated. In chapter 5 the verification of the system is presented and a summary and conclusion of the thesis is presented in chapter 6.

## 2. Theoretical background

Thunderstorms are characterized by the presence of lightning and its associated acoustic effect known as thunder. They are associated with deep, moist convection and strong vertical air motion. The type of cloud that gives rise to thunderstorms is referred to as a cumulonimbus cloud (Cb cloud). They are observed at low heights (0-2 km) and extend all the way to the top of the troposphere, up to heights of about 15 km.

This chapter provides the fundamental concepts necessary to understand thunderstorm development (2.1), explains the development of ordinary thunderstorms (2.2) and gives a description of lightning and storm electricity (2.3). A basic classification scheme of thunderstorm types is given in paragraph 2.4 and the final paragraph discusses thunderstorm climatology (2.5).

### 2.1 Fundamental concepts

#### 2.1.1 Cloud formation

Before considering large thunderstorm systems, it is important to understand the fundamental concepts of cloud formation. Clouds form when water vapor, which is present in air parcels, condenses. This happens when air is cooled to the temperature where it becomes saturated, the dew point temperature (Cotton, 1990).

A standard measure for the amount of water vapour that an air parcel contains is water vapour partial pressure ( $e$ ). It refers to the pressure exerted by only the water vapour part of the air parcel and is expressed in hPa. The maximum amount of water vapour that air parcels can hold is referred to as the saturation vapour pressure ( $e_s$ ). A parcel becomes saturated when  $e = e_s$ . Air parcels are subsaturated when  $e < e_s$  and supersaturated when  $e > e_s$ . The ratio of  $e$  to  $e_s$  can be expressed as Relative Humidity (RH) in percent:

$$RH = \frac{e}{e_s} * 100 \% \quad (2.1)$$

When air parcels cool,  $e$  remains constant and  $e_s$  decreases. The decrease of  $e_s$  with temperature is expressed by the Clausius-Clayperon relation (Iribarne and Godson, 1973). A graphical representation of the Clausius-Clayperon relation is presented in figure 2.1.  $e_s$  decreases with temperature, so that cooling air parcels experience an increasing relative humidity. Relative humidity increases until air parcels reach their dew point temperature and RH reaches 100%.

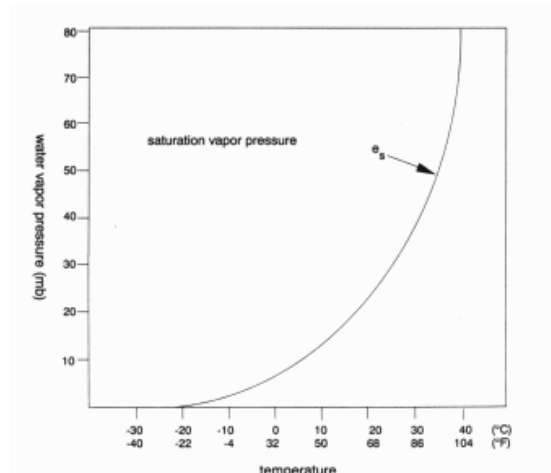


Figure 2.1 Clausius-Clayperon relation in graphical form. Water vapor pressure (mb) is plotted against temperature; saturation vapor pressure ( $e_s$ ) is indicated by a solid line. Source: Roelofs, 2010.

From RH levels of 100 % onward, water vapour is allowed to condense into water drops. It is not said however that water vapour condenses precisely at the dew point temperature. For the homogenous nucleation of water droplets, relative humidity levels of several hundred percents would be needed (Houze, 1993). Super saturation levels are rarely over 1% however. This is caused by Cloud Condensation Nuclei (CCN) on which cloud drops in the atmosphere grow, a process referred to as heterogeneous nucleation (Jacob, 1999). CCN are small (~0.02  $\mu\text{m}$ ), water attracting aerosol particles in the atmosphere. They originate from the condensation of gasses and action of the wind on the earth's surface and may have a natural or anthropogenic cause. Examples of CCN are: sea salt, soil dust, vegetation debris, organic carbon and sulphate. Because of the abundant presence of CCN in the atmosphere we can assume that clouds appear when air is cooled to the point where RH exceeds 100%.

The cooling of air particles in the atmosphere may happen in several different ways: by advection of warm air over a cold surface, by mixing of air parcels with different temperatures or by lifting of air to greater heights. Especially this latter mechanism is important for the formation of thunderstorms.

### *2.1.2 Convection*

Air parcels can be lifted to greater heights through mechanical or buoyant forces. Mechanical forces include orographic lifting or low-level wind shear. Buoyant forces arise in an unstable atmosphere, when air becomes warmer than its environment. Convection is a term describing rising air motion due to buoyant forces. Below we illustrate the process of convection, but first we need to understand how particles move vertically through the atmosphere.

When air parcels rise, they cool due to decreasing atmospheric pressure, which occurs at a certain rate of temperature decrease with height (Houze, 1993). The process is called adiabatic if air parcels exchange no heat with their environment. An unsaturated ascending air parcel experiences no heating or cooling within the system and follows a dry adiabatic lapse rate. The rate of temperature decrease with height of the dry adiabatic lapse rate is about 9.8 K/km, which remains approximately constant throughout the atmosphere. When an air parcel that follows the dry adiabatic lapse rate is cooled to its dew point temperature, it condenses. The level in the atmosphere at which air parcels start condensation is referred to as the Lifting Condensation Level (LCL). Beyond this level, phase changes occur and water vapour changes into liquid water. Phase changes are always accompanied by the release or absorption of heat within the system, which is caused by the fact that different phases of water contain different energy amounts. Heat is released in phase changes from water vapour to liquid water, called latent heat release. This causes condensating rising air parcels to cool at lower rate. Beyond the LCL, air parcels cool at the moist adiabatic lapse rate, which is about 4 - 6 K/km depending on moisture content.

As long as an air parcel is subsaturated it rises according to the dry adiabatic lapse rate and after it becomes saturated, rising air parcels follow the moist adiabatic lapse rate. Whether an ascending air parcel becomes or remains buoyant during its ascent can be understood by assessing the stability of the atmosphere. Atmospheric stability depends on environmental temperature decrease with respect to dry or moist adiabatic motion (Holton, 2004), shown in figure 2.2a. When the environmental lapse rate exceeds the dry adiabatic lapse rate, the atmosphere is absolutely unstable. An upward displaced air parcel is warmer than its environment, continues to be buoyant and accelerates away from its equilibrium position. In absolutely stable conditions on the other hand, the environmental temperature decrease is less than the moist adiabatic lapse rate. An upward displaced air parcel is cooler than its environment and will return to its original position. The atmosphere is referred to as conditionally unstable when it is stable with respect to dry adiabatic displacements but unstable with respect to moist adiabatic displacements. In conditionally unstable environments, saturated air parcels are able to rise as a convective cloud when they follow the moist adiabatic lapse rate.

Figure 2.2b illustrates a conditionally unstable atmospheric situation. An air parcel is heated at the earth's surface by the sun, it rises and cools dry adiabatically. When the air parcel has enough

momentum to reach the LCL, latent heat is released, which results in a warming of the air parcel. The air parcel follows the moist adiabatic lapse rate from here on and may ascend up to the level where the atmosphere becomes conditionally unstable, the Level of Free Convection (LFC). From here on, air parcels can rise freely as a convective cloud. The air parcel's ascent continues until it reaches a stable atmospheric level, called the Level of Neutral Buoyancy (LNB). At the LNB, the environmental lapse rate becomes stable with respect to the moist adiabatic lapse rate, vertical motion ceases and the cloud top height is attained.

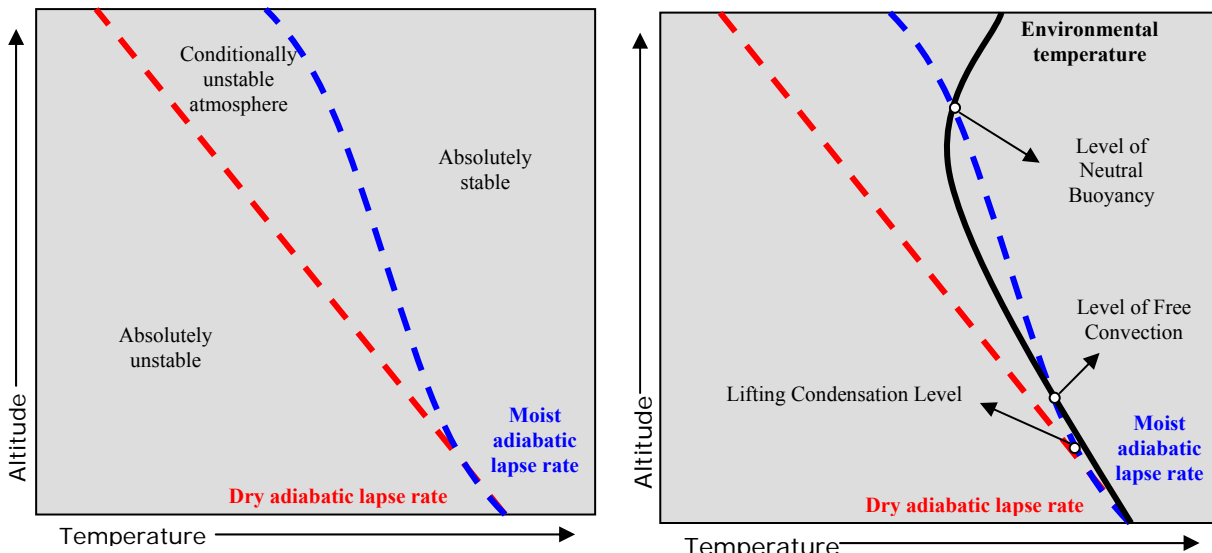


Figure 2.2 Left: atmospheric stability for different environmental lapse rates with respect to dry or moist adiabatic motion. Right: Example of a conditionally unstable atmospheric situation (Adapted from Cotton, 1990).

There is another form of atmospheric instability however that is associated with convective environments, called potential instability. In a potentially unstable atmosphere, equivalent potential temperature decreases with height. Potential temperature is the temperature that an air parcel would have if it was adiabatically brought down to a reference pressure (usually 1000 hPa). Equivalent potential temperature is the potential temperature that an air parcel would have if all its moisture were condensed and if the latent heat released during the process was used to warm the air parcel (Holton, 2004). If a layer with decreasing equivalent potential temperature is lifted, the bottom of that layer, given sufficiently large relative humidity, becomes saturated before the top of the layer. The bottom of the layer would thus cool at the moist adiabatic lapse rate while the top cools at the dry adiabatic lapse rate. The top cools faster than the bottom, making the layer unstable and creating a convective environment.

### 2.1.3 Buoyancy and cloud particles

Atmospheric instability causes air particles to become buoyant and initiates convection. Beyond the LCL, buoyancy of air particles is however affected by more than just temperature. Two other effects play an important role, which are the presence of hydrometeors and the pressure gradient force (Houze, 1993).

As cloud droplets increase in size from the LCL, they grow to eventually become precipitation particles and, when cooled enough, ice particles. Precipitation and ice particles in a cloud are called hydrometeors. They influence the buoyancy of air by producing a downward directed drag on cloud parcels, which is transmitted by the weight of hydrometeors on upward moving air. The greater the mass of condensed water in a cloud, the greater the drag exerted on upward moving air parcels.

Another important force affecting buoyancy is the pressure gradient force. The pressure gradient force is directed from high to low pressure. As pressure decreases with height in the atmosphere, an upward directed vertical pressure gradient force is always present. This force is nearly balanced by gravity

however (the hydrostatic balance), which explains why the atmosphere does not ‘overturn’. But acceleration of rising air parcels can have an influence on pressure distribution within a cloud. Non-hydrostatic pressures are observed when slow moving air parcels collide with faster moving air parcels and vice versa. This way, rising air in a cloud causes high pressures to develop at the top, when it encounters environmental air. In a similar way, a relatively low non-hydrostatic pressure develops at the bottom. This low pressure causes air to rush into the cloud.

Including hydrometers and the pressure gradient force, buoyancy of air can be approximated by (Houze, 1993):

$$B = g \left[ \frac{T^*}{T_0} - \frac{P^*}{P_0} + 0.61 q_0^* - q_H \right], \quad (2.2)$$

$T^* / T_0$  And  $P^* / P_0$  are temperature and pressure perturbations with respect to their reference environmental values.  $q_0^*$  Is the mixing ratio of water vapour and  $q_H$  is the mixing ratio of the hydrometeors. Temperature and pressure perturbations can both increase and decrease the value of buoyancy. Increasing water vapour mixing ratio value has a positive effect on buoyancy and an increasing hydrometer mixing ratio has a negative effect on buoyancy.

A third positive effect on buoyancy may also be mentioned, which is caused by the freezing process of water droplets (Doswell, 2001). As thunderstorm clouds extend high into the atmosphere, they inevitably encounter temperatures below 0 °C. Homogeneous ‘super-cooled’ water drops remain unfrozen until they reach temperatures below -40 °C. The freezing process is however speeded up, like in water droplet condensation, by the presence of CCN that bring freezing temperatures to just below 0 °C. Important to the droplet freezing process and ice crystal growth is the additional latent heat that is released. This latent heat contributes to the buoyancy of the cloud and gives the air parcels an additional ‘boost’ in their ascent. Consequently, cumulonimbus clouds often show a very fast vertical development once ice is observed within the cloud. Generally parcels will overshoot the LNB, from unstable regions into the stable regions of the atmosphere above the LNB. Beyond the LNB the air parcel experiences negative buoyancy and undergoes a damped oscillation.

#### 2.1.4 Favourable conditions for thunderstorm development

The development of thunderstorms depends on the presence of atmospheric conditions favourable for deep moist convection. Deep moist convection refers to strong updrafts that lift air parcels to the point of saturation, beyond which they remain positively buoyant. There are three main atmospheric conditions that are necessary for the initiation of this process. They are known to be the following (Johns and Doswell, 1992). Significant conditional or potential instability through a deep layer of the atmosphere, which causes parcels to be accelerated to great heights once they reach the LFC. A force of lift to accelerate parcels up to the LFC, so instability can be released. And a high moisture content of the air, which lowers the LFC and makes the air more buoyant by releasing latent heat.

Several indices have been developed to measure the susceptibility for deep moist convection given temperature and moisture content. One most frequently used measure is the Convective Available Potential Energy (CAPE), which is given by (Moncrieff and Miller, 1976):

$$CAPE = g \int_{LFC}^{LNB} \left( \frac{T_{V_{parcel}} - T_{V_{environment}}}{T_{V_{environment}}} \right) dz \quad (2.3)$$

CAPE is calculated by integrating the buoyancy ( $B$ ) from the LFC to the LNB and indicates the maximum kinetic energy available to an air parcel. Virtual temperature ( $T_v$ ) of a moist air parcel is the temperature that a dry air parcel would have if its pressure and density were equal to that of the moist air parcel. CAPE and other indices will be used in this research and are discussed in chapter 4.

## 2.2 Ordinary thunderstorms

Ordinary thunderstorms or single cell thunderstorms are distinguished by a well defined life cycle that lasts about an hour and consists of 3 stages: the cumulus stage, the mature stage and the dissipating stage (Kessler, 1986), shown in figure 2.3.

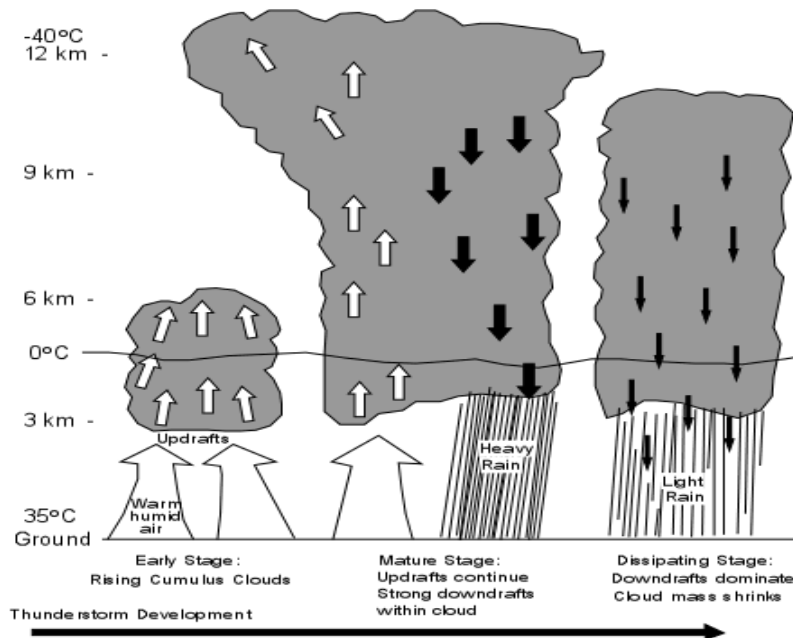


Figure 2.3 Illustration of 3 thunderstorm stages: the cumulus stage, the mature stage and the dissipating stage (From [www.earthsci.org](http://www.earthsci.org)).

The cumulus stage is characterized by the development of towering cumulus clouds in a region with low level convergence of warm and moist air. Updrafts dominate the system and different clouds may merge to form larger cloud systems. The merger often causes explosive growth of one of the merging clouds and precipitation may start to form in upper levels of the cloud.

The mature stage of a thunderstorm cloud begins with rain that settles in the lower layers of the cloud. The large Liquid Water Content (LWC), the mass of water within a cloud, causes the storm to create downdrafts in the interior. When precipitation particles reach lower levels, they partially evaporate, which cools the air and further enhances downdrafts. Downdraft air spreads horizontally at the earth's surface and lifts warm moist air from lower levels back into the cloud system. This way, the system can sustain itself. Latent heat release decreases the pressure in the mid levels of the cloud and helps create a pressure gradient force directed upward. This helps to draw warm moist air to the LFC and thus further helps sustain the system. At the interface between the downdraft air and the updraft air, a gust front forms. The winds at the earth's surface change rapidly in speed and direction, which can give extra fuel to the updraft of warm, moist air. At the top of the cloud system, updrafts spread horizontally as they enter the LNB, where ice crystals form an anvil cloud.

Precipitation intensity reaches a maximum during the mature stage of the thunderstorm. During this stage the thunderstorm is characterized by heavy rainfall and wind gusts, especially at the gust front. As the depth of the downdraft increases and the temperature of the downdraft air decreases, the gust front gets further away from the storm. At a certain point, when the gust front has moved to far ahead of the thunderstorm system, the air lifted at the front does not enter the system anymore. This is when the thunderstorm starts its dissipating stage. During the dissipating stage, updrafts weaken and downdrafts dominate the system. At the end of the lifecycle only light precipitation from the cloud top remains.

## 2.3 Classification of thunderstorms

The number, type and distribution of cells from which thunderstorms are built determines their types. Some storms contain only one kind of cell; others may contain a combination of different types of cells. An explanation is given below of the different thunderstorm types (Kessler, 1986). Figure 2.4 shows a classification of several thunderstorm categories, where non-severe thunderstorm types are indicated by green and severe thunderstorms by red.

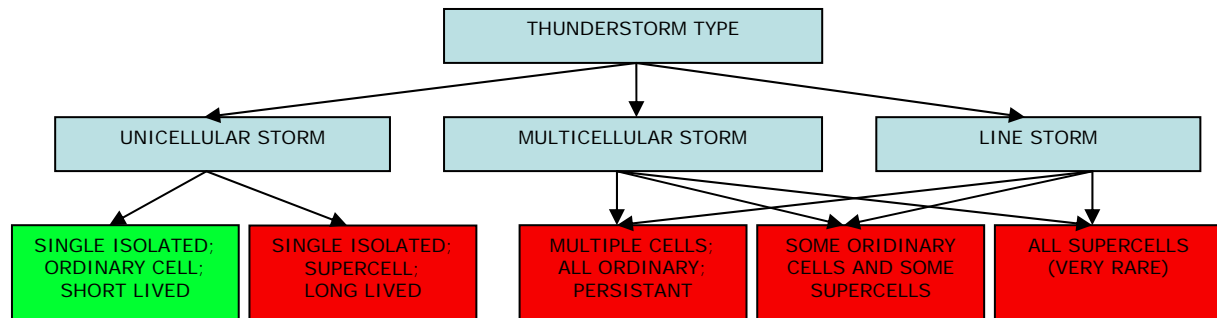


Figure 2.4 A simple classification of thunderstorm types. The primary classification relates to basic cell type, the secondary classification to entire storm complex (adapted from Kessler, 1986)

Unicellular storms occur in two different forms, ordinary thunderstorms and supercells. Ordinary thunderstorms, described in the previous section, have a single, isolated cell structure and go through a relatively short lifecycle. A much more violent and rare thunderstorm is the supercell thunderstorm. They are rotational storms that last up to days and are known for producing damaging hail and tornadoes. For a supercell to form, warm moist air is needed at lower levels with an inversion at greater heights. This so called capping inversion allows air above the inversion to cool and air below to warm making the atmosphere increasingly unstable. When the capping inversion finally weakens or moves, the supercell develops. Their rotation is derived through tilting of horizontal vorticity (local, instantaneous rotation) caused by wind shear. Strong updrafts lift rotating air and thereby, a deep rotating updraft is formed capable of producing the largest and most persisting tornadoes and the largest hailstones.

Multicellular storms and line storms consist of multiple cells that each undergo a lifecycle. In a multicellular storm, the systems organize as a cluster, whereas in a line storm, cells are laterally aligned. They may both have lifetimes of several hours and the damage produced by these storms may be significant, especially when supercells are embedded in the system. Line storms usually exhibit a bow shape, where thunderstorms align parallel to the front of the bow. They usually develop ahead or along a cold front which is associated with a mid latitude storm, often in the warm sector of the cyclone just ahead of the cold front. The region contains warm, moist air with strong vertical wind shear, which helps to organise thunderstorms into a line. In multicellular storms convection is organized in a random configuration. Multicellular storms experience ascending air in a broad region around the main convective cores. It requires sustained forcing from the environment to trigger formation, which is usually provided by low level convergence and moist air. When multicellular storms or line storms get large enough they are referred to as Mesoscale Convective Systems (MCS).

## 2.4 Lightning and storm electricity

What thunderstorms are best known for is the lightning and thunder that they produce. Any type of thunderstorm produces lightning, which is the result of build-up of electrical charge difference between the top and the bottom of a cloud. There is still debate over which process causes the division of the charge within a thunderstorm cloud. Two main theories are adopted to give an explanation for the electrification of thunderstorms: 1) attributes charge division to convection and 2) relates charge division to collision between cloud particles (Cotton, 1990).

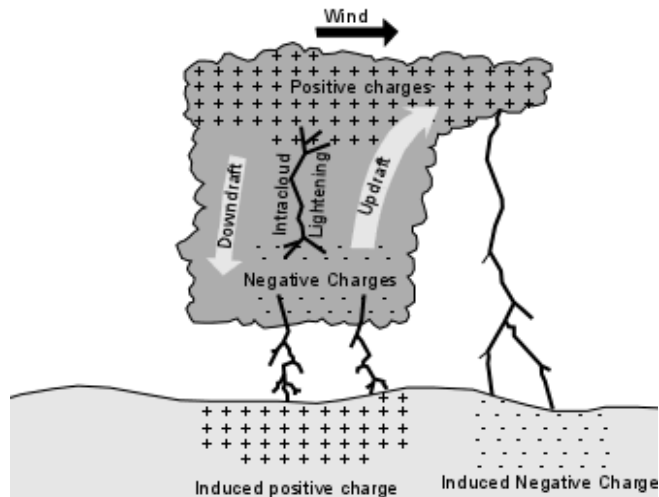


Figure 2.5 Illustration of charge separation within a cloud, responsible for lightning (From [www.earthsci.org](http://www.earthsci.org)).

In theory 1, a normal fair weather electrical field is assumed with positively charged ions at the earth's surface. The atmosphere on the other hand is assumed to have negatively charged ions under the influence of cosmic radiation. When updrafts associated with the convective cloud system carry positively charged ions from the surface into the cloud, they attract negatively charged ions in the atmosphere to the cloud edges. Negatively charged ions become attached to water droplets and ice crystals at the edge of the cloud forming a negatively charged layer at the cloud boundaries. Downdrafts near the cloud edges are then said to carry negatively charged particles downward, causing charge division within the cloud. The theory however only relies on particle motions within the cloud and cannot account for observations showing that lightning initiates at the onset of precipitation or that the centre of negative charge is at  $-15\text{ }^{\circ}\text{C}$  in a thunderstorm.

In theory 2, it is thought that the precipitation forming processes are responsible for charge separation within the cloud. The graupel-ice collision mechanism is most widely accepted. Graupel is precipitation that forms when super cooled water droplets condense on a snowflake (Rakov and Uman, 2003). The theory is based on experimental data that show the occurrence of charge transfer during collisions between ice crystals and graupel particles. The sign and magnitude of this charge transfer was found to be a function of LWC and temperature. Experiments show that the sign of charging of the graupel particle reverses between  $-10\text{ }^{\circ}\text{C}$  and  $-20\text{ }^{\circ}\text{C}$ . At temperatures Above this reversal temperature, graupel particles become negatively charged when they collide with ice crystals. This can explain the centre of negatively charged particles that is located around  $-15\text{ }^{\circ}\text{C}$ . Below the reversal temperature, graupel particles get positively charged, which may account for the vertical division of charge in the cloud.

Once the charge separation reaches a certain strength, lightning attempts to neutralize the separated charge. Lightning can occur between clouds (cloud-to-cloud), between the cloud and the ground (cloud-to-ground), or inside the cloud (intra-cloud). The heated channel of this lightning stroke may reach temperatures up to  $30,000\text{ K}$ , which causes expansion of the heated gasses and gives rise to a shock wave heard as thunder.

## 2.5 Thunderstorm climatology of the Netherlands

The Netherlands has a maritime environment with no significant orography. Convective instability is usually weak in such regions and a capping inversion is needed for the outbreak of deep, moist convection (Browning et al., 2007). Such an inversion can be present in the lower or middle troposphere and traps air underneath. In the summertime, the trapped air continues to be heated and a layer of warm moist air builds up beneath the inversion. If it becomes buoyant enough to penetrate the capping inversion, convective environments form, potentially turning into thunderstorms. This process can be stimulated by low-level convergence that causes the LCL to rise and the inversion to become thinner. Thunderstorms may furthermore develop in the Netherlands due to forced lifting of air along fronts or in cold air behind a cold front when it moves over a warm surface.

The total number of detected lightning discharges over the years indicates thunderstorm variability in the Netherlands. Such a plot is presented in figure 2.6 and shows data for the years 2004 – 2010. Most lightning is detected during the summer half year. The exact amount of detected discharges does however vary over the years, as they are largely dependant on the type of weather systems that are present.

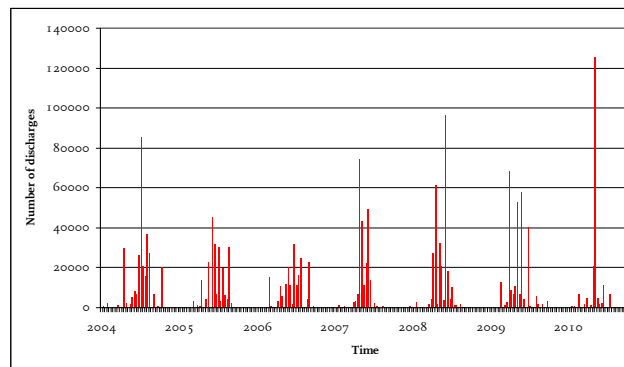


Figure 2.6 Total number of discharges per 10-day period over the years 2004 – 2010. Adapted from *Bosatlas van het klimaat* (2011).

Figure 2.7 shows the diurnal cycle of thunderstorms (2.7a) and severe thunderstorms (2.7b), where climatological thunderstorm probability is plotted versus time. A well-defined daily cycle is present; climatological probability increases throughout the day, reaches a maximum in the late afternoon and decreases again towards the night. This is a result of the mechanism described above that causes low level air to heat throughout the day and most thunderstorms to develop in the late afternoon.

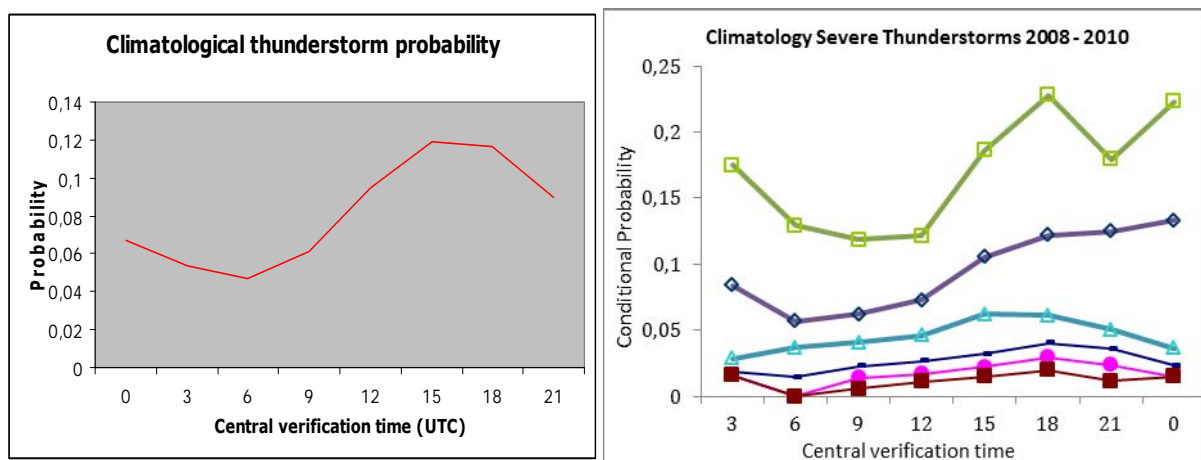


Figure 2.7 a: Climatological probability of thunderstorms versus central verification time from data of the summer half years of 2008 – 2010, averaged over 12 regions of the Netherlands. B: climatological probability of severe thunderstorms for thresholds of maximum 5 minute lightning intensity, equal to 50 (green), 100 (purple), 200 (turquoise), 300 (blue), 400 (pink) and 500 (red) versus central verification time from data of the summer half years of 2008 – 2010, averaged over 12 regions of the Netherlands.

### 3. Remote sensing of clouds, precipitation and lightning

Remote sensing refers to the acquisition of information about an object or phenomena from a distance. In meteorology one can use satellite to detect clouds and cloud physical properties, weather radars are used to detect precipitation areas and lightning detection networks have been developed to detect lightning. All these instruments use radiation either actively or passively. It is therefore important to address the basics of radiation, which is done in paragraph 3.1. Paragraph 3.2 discusses satellite measurements, paragraph 3.3 introduces radar measurements and paragraph 3.4 explains lightning detection.

#### 3.1 Radiation

##### 3.1.1 Radiation basics\*

All substances with a temperature above absolute zero emit radiation. The higher the temperature of a substance, the more radiative energy it can emit and the lower the wavelength of the emitted radiation. Wavelengths are defined as the difference between the crests of an electromagnetic field and are often used to specify radiative energy. Radiation can also be thought of as a particle that represents the movement of energy through space.

When a beam of radiation encounters a substance (such as a molecule), several interactions between the radiation and the substance are possible. Radiation can pass through the substance unchanged, which is referred to as perfect transmission. Radiation can be reflected and change direction, called scattering. Or radiation can be absorbed, which causes the energy to be transferred to the substance. Whether radiation passes through, is reflected or scattered by a substance depends on the wavelength of radiation and the physical properties of the substance.

Some substances are good absorbers and emitters at a certain wavelength while others are not. The absorption coefficient  $\alpha(\lambda)$  is defined as part of the radiation with wavelength  $\lambda$  that is absorbed by a substance. The emission coefficient  $\varepsilon(\lambda)$  is the ratio between radiation that is actually emitted and the maximum emitted radiation at a wavelength. Both can vary between 0 and 1.

Kirchoff's law of thermodynamics states that at thermal equilibrium, the emissivity of a substance is equal to its absorptivity,  $\alpha(\lambda) = \varepsilon(\lambda)$ . A perfect blackbody is defined as an object that absorbs all radiation: an object that has an absorptivity  $\alpha = 1$  for all wavelengths. According to Kirchoff's law, a perfect blackbody would have an emissivity of  $\varepsilon = 1$  at all wavelengths as well.

Plank's law describes the amount of energy emitted by a perfect blackbody at a certain wavelength:

$$E(\lambda, T) = \frac{C_1 \lambda^{-5}}{\exp\left(\frac{C_2}{\lambda T}\right) - 1} \quad (3.1)$$

Where  $C_1$  and  $C_2$  are constants with the values:  $C_1 = 3.7417 \cdot 10^{-16} \text{ Wm}^2$  and  $C_2 = 1.4388 \cdot 10^{-2}$ . T is temperature [K] and E is expressed in  $[\text{kW/m}^2]$ . Plank's law shows that as the temperature of a body rises, the peak of radiative energy shifts toward shorter wavelengths. Several spectra relating transmitted wavelength to radiative energy, using Plank's formula, are shown in figure 3.1a for different temperatures. Note that the scale for both temperature and spectral radiant energy is logarithmic.

*\*This section is largely based on Roelofs (2010)*

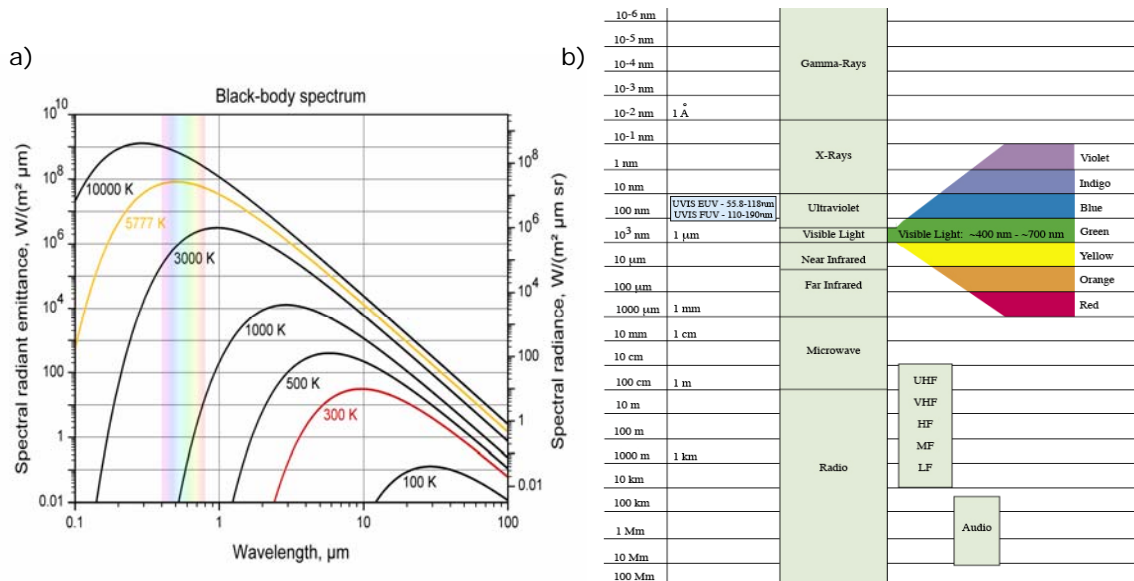


Figure 3.1 a) Blackbody spectrum that shows radiative energy over wavelength for different temperatures. The yellow line indicates the temperature of the sun; the red line indicates the temperature of the earth. b) the electromagnetic spectrum with names given to the various wavelength bands (From Laboratory for Atmospheric and Space Physics (LASP), Colorado, USA: [lasp.colorado.edu](http://lasp.colorado.edu)).

The yellow line in figure 3.1a indicates the temperature of the sun (5777 K) and the red line temperatures of the earth (300 K). Most radiative energy of the sun is between wavelengths of 0.1 and 4  $\mu m$ , referred to as short wave radiation. Most radiative energy of the earth is between wavelengths of 4 and 100  $\mu m$ , referred to as long wave radiation. Figure 3.1b shows the electromagnetic spectrum with names given to the various wavelength bands. Shortwave radiation that the sun emits is in the ultraviolet, visible light and near infrared part of the electromagnetic spectrum. The earth emits infrared radiation.

The theory of blackbodies is important to understand, as it provides the wavelength band that a substance with a certain temperature emits. In nature perfect blackbodies do not occur however. To retrieve the actual radiant energy of a substance, blackbody radiance needs to be multiplied by the emissivity coefficient of the substance:  $E_{emitted}(\lambda) = \epsilon(\lambda) * E_{BB}(\lambda)$ . Most surfaces on earth have an emission coefficient close to 1 for the long wave radiative part of the spectrum. This is however different for short wave radiation. Snow is an example of a perfect blackbody for emitted long wave radiation, while almost all shortwave radiation is reflected.

### 3.1.2 The global radiation balance

The earth's global mean radiation budget is shown in figure 3.2, values are given in  $W m^{-2}$ . In the earth's climate system, the sun is the most primary source of energy (Kiehl and Trenberth, 1997). Most of the sun's energy consists of wavelengths in the ultraviolet, visible and near infrared part of the electromagnetic spectrum, referred to as short wave radiation, as mentioned above. The average solar energy that is available at the top of the atmosphere is  $342 W m^{-2}$ . This radiation is redistributed throughout the climate system and about half of the short wave radiation is absorbed by the earth's surface. This energy is transferred back to the atmosphere by warming the air in contact with the surface (thermals), by evapotranspiration and by long wave radiation. In the long term, incoming shortwave radiation from the sun is balanced by outgoing long wave radiation. Greenhouse gasses and clouds absorb part of the outgoing long wave radiation by behaving as blackbodies in the infrared spectral region. They absorb and re-emit infrared radiation and thereby, they warm the earth's surface. The effect of clouds is counteracted by the fact that they reflect shortwave radiation from the sun back to space.

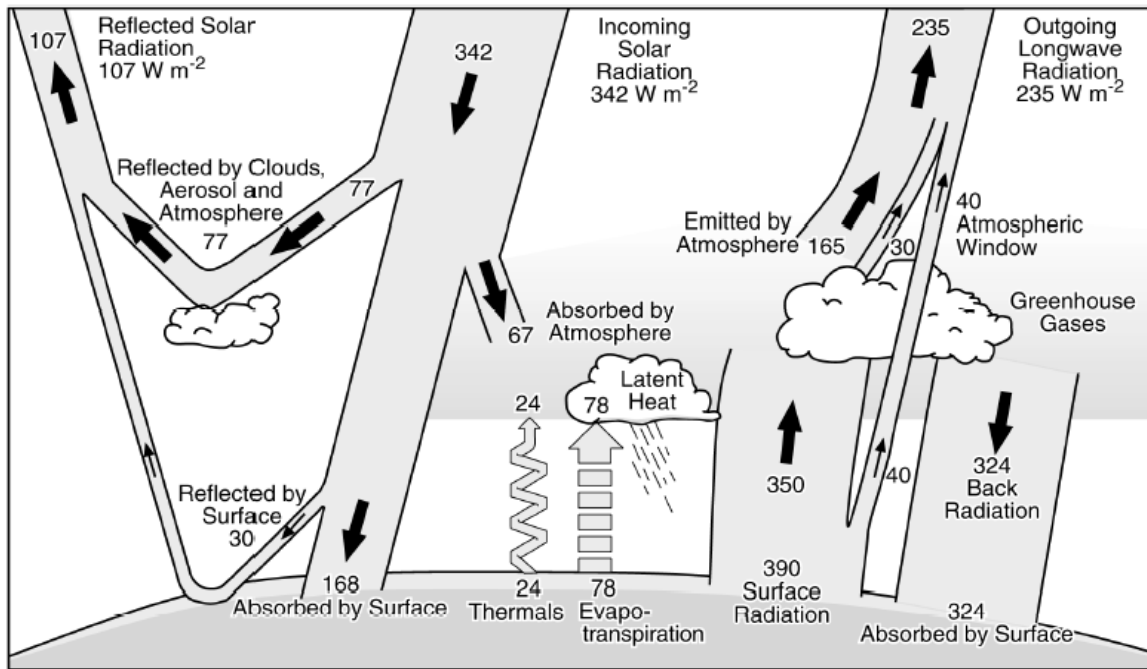


Figure 3.2 Energy balance at the earth, values are given in  $W m^{-2}$  (Kiehl and Trenberth, 1997).

### 3.1.3 The effect of clouds on radiation

Clouds have an important effect on the earth energy budget because they reflect, absorb and re-emit radiative energy, as stated above. The effects of an individual cloud are determined by its optical properties, such as their optical thickness, scattering albedo and emissivity. These can in turn be related to a cloud's micro- and macro physical properties (Roebeling, 2008). Micro physical properties include thermodynamic phase, particle size, droplet concentration and liquid water path. Macro physical properties include geometrical thickness, cloud base height, cloud top height and cloud fraction. Clouds physical properties determine how much shortwave radiation from the sun is reflected and how much long wave radiation is absorbed and emitted.

The cloud reflective properties have a cooling effect on the earth. This is referred to as cloud albedo forcing. When clouds have water droplets with high droplet number concentrations (low clouds), their albedo forcing is high and they have a large cooling effect. However, if clouds consist mostly of ice particle (high clouds), they have low droplet number concentrations and their cooling effect is reduced. Thunderstorm, or cumulonimbus clouds extend high into the atmosphere; they have high droplet number concentrations especially at the cloud base.

The warming effect of clouds by absorbing and re-emitting long wave radiation depends primarily on their position and blackbody behaviour (Roebeling, 2008). Low clouds that are present in the bottom 2 km of the atmosphere have temperatures close to those of the earth's surface. Therefore they emit comparable amounts of energy to outer space and have little effect on warming. High clouds, on the other hand, are a lot colder and emit significantly lower amounts of energy to outer space. They have a warming effect because they absorb radiation emitted by the earth, but emit substantially less to outer space. The effect that thunderstorm clouds have on long wave radiation depends on their cloud top heights. Colder cloud tops emit less radiation to outer space; they have a larger warming effect.

### 3.2 Remote sensing of clouds using satellites

Since the 1960's meteorologists have been able to use meteorological satellites for cloud observational studies. Meteorological satellites have passive sensors that measure radiation, which is naturally emitted by the earth's surface, the atmosphere and clouds. The instruments measure reflected, scattered and emitted radiation at different wavelengths throughout the day. Clouds are detected because they reflect shortwave radiation and absorb and re-emit long wave radiation based on their micro- and macro physical properties. This allows meteorologists to continuously survey clouds over large regions, even the whole globe.

#### 3.2.1 Meteosat Second Generation

Several countries operate meteorological satellites either independently or in collaboration. In this study we use data from Spinning Enhanced Visible and Infrared Imager (SEVIRI) onboard the Meteosat Second Generation (MSG) satellite. The European Space Agency (ESA) operates MSG in collaboration with European Organisation for the Exploitation of Meteorological Satellites (EUMETSAT). MSG was launched in 2002 and has a geosynchronous orbit, which means that the orbit has a fixed position relative to the earth. The satellite is situated over the equator and revolves around the earth at the same speed that the earth rotates around its axis. The position of the MSG satellite is chosen in such a way that it captures both Africa and Europe in its measurements (figure 3.3).

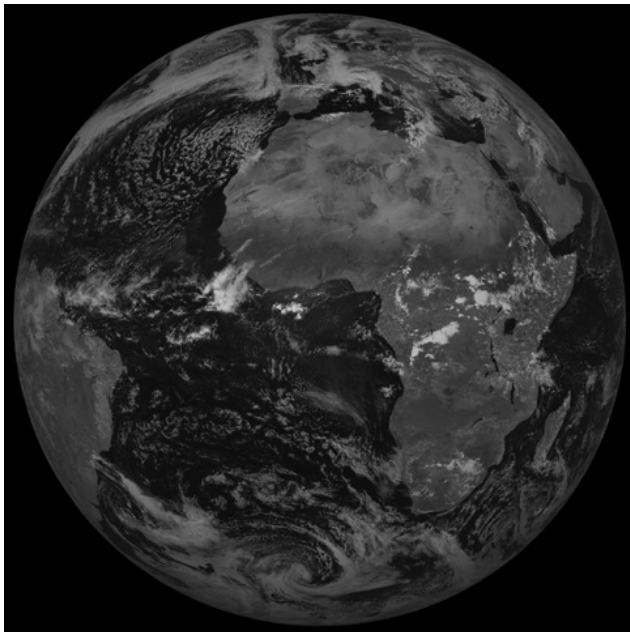


Figure 3.3 MSG – SEVIRI full disk image, 10.8  $\mu\text{m}$  channel. Source: <http://www.eumetsat.int>

The SEVIRI instrument is an imaging radiometer and has been employed on the MSG satellite to secure continuous observations of the earth's full disk (EUMETSAT, 2009). It builds up images from the Earth's surface and atmosphere at 12 different wavelengths and sends information back to the Earth every 15 minutes. The image sampling distance is 3 km at nadir view, except for the High Resolution Visible (HRV) channel, which measures at a 1 km resolution at nadir view. In larger, off nadir viewing angles the resolution gets coarser. A complete image of the Earth's full disk consists of 3712 x 3712 pixels, which are measured from south to north and east to west.

SEVIRI measures eight thermal infrared channels and four visible channels. The visible channels indicate the reflectance of sunlight from the Earth's surface and clouds. The remaining 8 channels monitor emitted thermal infrared wavelengths. The channels have been selected such that they provide good information on clouds, water vapour, carbon dioxide and ozone.

### 3.2.2 Cloud Physical Properties derived from satellite data

Because Cloud Physical Properties (CPPs) have such a profound effect on the radiation in the atmosphere, they can be estimated from SEVIRI measurements using an algorithm (Roebeling, 2008). CPPs are derived using a CPP algorithm of the Satellite Application Facility on Climate Monitoring (CM-SAF). The CPP algorithm is a two-step approach. In the first step, cloudy pixels are separated from non-cloudy pixels in a satellite image; cloud pixels are pixels that are (partly) filled with clouds and non-cloudy pixels represent clear skies. The separation of cloudy pixels from non-cloudy pixels is subsequently used to generate a cloud mask with 4 confidence intervals: clear certain, clear uncertain, cloud uncertain and cloud certain.

In the second step, reflectances of cloudy pixels are related to cloud physical properties using a Radiative Transfer Model (RTM). Several RTM models have been developed but the Doubling-Adding KNMI (DAK) RTM is used at KNMI (Stammes, 2001). An RTM models the effect that CPPs have on the path of radiation through the atmosphere. They are used to determine the expected satellite reflectances in the different channels for many different cloud situations. The result are databases of expected reflected light in the direction of the satellite, which are referred to as Look Up Tables (LUTs). CPPs be can derived from satellite information by comparing information in the LUTs to observed reflectances from the SEVIRI instrument.

The CPP algorithm retrieves several CPPs from different wavelength channels measured by the MSG satellite. The derived CPPs include the following: Cloud Optical Thickness (COT), Cloud Phase (CPH), Particle Effective Radius (REFF), Precipitation (Precip), Cloud Top Temperature (CTT), Cloud Column Height (CCH), Cloud Water Path (CWP), Cloud Depth (DCLD), Cloud Droplet Density (DNDV) and Downwelling Solar Radiation (SDS). Below the derivation of several CPPs is described.

Cloud Optical Thickness (COT) and particle size, defined as Effective Radius (REFF), are retrieved from visible (0.6  $\mu\text{m}$ ) and near-infrared (1.6  $\mu\text{m}$ ) wavelengths. The basis of these methods is that reflectances of clouds in the visible region (0.6 – 0.8  $\mu\text{m}$ ) are strongly dependent on COT, whereas reflectances in the near-infrared region (1.6 – 3.9  $\mu\text{m}$ ) are strongly dependant on particle size. Comparing the satellite observed reflectances at both wavelengths to LUTs for predefined COT and REFF values gives the observed values of COT and REFF (Jolivet and Feijt 2003). During the process, the retrieval of COT at the 0.6  $\mu\text{m}$  channel is used to update the retrieval of REFF at the 1.6  $\mu\text{m}$  channel. This process continues until the CPPs reach stable values. In the LUTs, interpolation for COT is done using polynomial interpolation and for REFF using linear interpolation.

Cloud Top Temperature (CTT) is derived in the CPP algorithm from the 10.6  $\mu\text{m}$  brightness temperature. The brightness temperature is the observed temperature assuming an emissivity of 1. For optically thick clouds the emissivity does approach 1 and brightness temperature can be regarded as the thermodynamic temperature of the upper part of the cloud. For optically thin clouds brightness temperatures also have a contribution from upwelling radiation from the surface below. This is corrected for using cloud absorbing optical thickness, which is related to COT.

Cloud Thermodynamic Phase (CPH) is determined using a consistency test of the observed difference in cloud reflection at 0.6  $\mu\text{m}$  and 1.6  $\mu\text{m}$ , and a threshold test of the 10.6  $\mu\text{m}$  brightness temperature. The consistency test compares the observed and simulated differences in cloud reflectance at 0.6 and 1.6  $\mu\text{m}$  wavelengths. This difference is mostly caused by the stronger absorption of ice particles over water particles at the 1.6  $\mu\text{m}$  wavelength. Pixels that are identified as ice clouds with CTTs lower than 265 K are then given the CPH 'ice', all others are considered to be water clouds.

From the CPPs above, different CPPs can be calculated using subsequent algorithms. An example is the Precipitation Properties (PP) algorithm. It uses CWP, REFF and CPH to detect precipitating clouds, while LWP and CTT are used to estimate precipitation rates. The detection of precipitating clouds is done in a three-step procedure (Roebeling et al., 2009), where clouds with CWP values

above a certain threshold value are considered as potentially precipitating clouds. Information from CPH is then used to separate ice and water clouds. All ice clouds are considered precipitating. For the remaining water clouds, information on droplet radius is used to differentiate between precipitating and non-precipitating clouds. Precipitation rates are derived using a parameterization proposed by Wentz and Spencer in 1988.

CPP retrievals are limited to solar zenith angles under  $72^\circ$ . Retrievals at larger angles are excluded because they show more inaccurate RTM simulations, a lower signal to noise ratio of the radiation observations and three dimensional cloud effects (Roebeling et al., 2009). CTTs can however be derived at higher zenith angles, as they are exclusively determined by the  $10.8 \mu\text{m}$  brightness temperature.

### 3.3 Remote sensing using weather radars

Another remote sensing instrument used for routine observations is the weather radar, which measures reflectivity from raindrops. The weather radar is an active system, unlike satellite remote sensing systems, which are passive. It sends out a pulse of electromagnetic radiation and then senses the radiative energy that is reflected back to the radar (Cotton, 1990). This can be accomplished when the radar switches alternately between emitting and receiving pulses of radiation using an antenna.

Weather radars operate in a microwave region at wavelengths between 5 and 10 cm. Radiation at these wavelengths is hardly effected by the presence of clear air or even small cloud droplets. Raindrops, hailstones and larger snow particles reflect the radiation quite strongly however (Rinehart, 2006). The more particles in the air and larger their size, the stronger this reflection will be. As electromagnetic radiation travels at a nearly constant speed ( $3 \times 10^8 \text{ m/s}$ ), the position of the reflecting precipitation particles can be estimated from the time it takes the signal to move from the transmitter and back. This way, a weather radar can sense the presence of precipitation 300 km away from its location. Scanning in a circle around the radar and raising the elevation angle of the antenna at different intervals can sample entire volumes of the atmosphere.

KNMI operates two weather radars in the Netherlands; in De Bilt and Den Helder. Figure 3.4 indicates the observation range of both radars. They measure every 5 min at 14 elevation levels between 0.3 and 25 degrees at a resolution of  $1 \times 1 \text{ km}^2$ .



Figure 3.4 Location of KNMI weather radars of De Bilt and Den Helder. The open circles represent the observation range of both radars (Roebeling, 2009).

### 3.4 Lightning detection

Aleksandr Popov developed the first lightning detection network at the end of the 19th century. The system worked using devices to detect very low frequency waves, which are emitted by lightning. It counts disturbances that exceed a certain threshold and with multiple of these devices, a detection network can be formed (Wessels, 1998).

KNMI uses the Surveillance et d'Alerte Foudre par Interférométrie Radioélectrique (SAFIR) lightning detection network. This system works using interferometry. The phase differences between signals detected by 7 antennas (figure 3.5) are associated with the direction of a signal. The exact location of the signal is determined using a triangular calculation from the signal direction at several stations. Two wavebands are measured; one for signal localization (around 110 MHz) and one for the distinction between Cloud-to-Ground (CG) and Cloud-to-Cloud (CC) lightning (around 4 MHz). Discrimination between CGs and CCs is achieved mainly by analysing the difference in disturbance length between the detected low frequency wave. CGs have a relatively long length of disturbance with respect to CCs. There are however CCs that can have longer disturbance lengths and they may wrongly be seen as CG's (Holle and Lopez, 1993). Raw data from the system is processed at KNMI. Signals are divided into 'traces', which refers to a bundle of signals that all belong to a certain lightning event. The data is saved every 5 minutes in an archive.

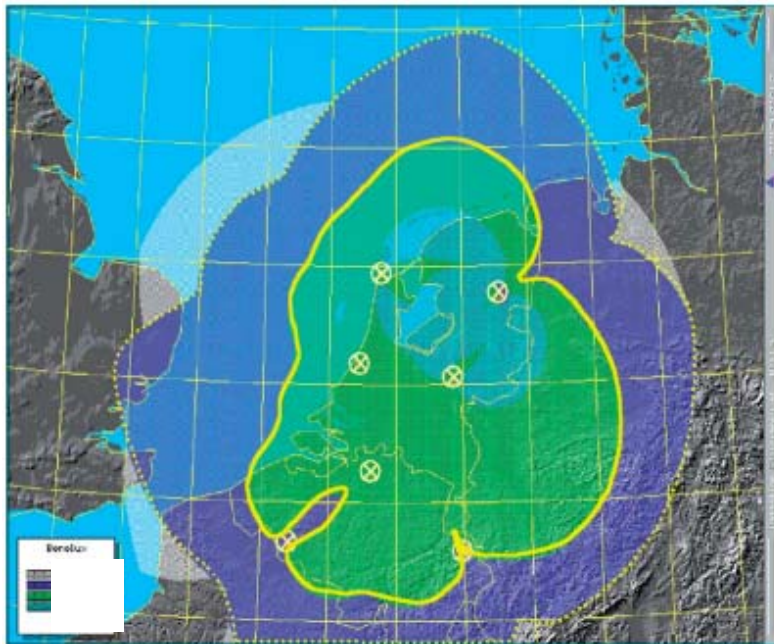


Figure 3.5 Lightning detection network used by KNMI. Detection stations (marked with a circle and cross) are located in De Kooy, Valkenburg, Deelen, Hoogeveen, Oelegem, Mourcourt and La Gilleppe. The colours show the accuracy of the location determination (from: KNMI handboek H20).

## 4. Data and Methods

In this study we investigate an ensemble of Meteosat Second Generation (MSG) data as an additional predictor source to the 0–6 h projections of the MOS thunderstorm forecasting system, operational at KNMI. New forecast equations are derived, many aspect of the system remain similar to those used in Schmeits et al. (2008) however.

In this chapter we discuss the data and methods used in this study. Paragraph 4.1 describes the technique used to derive new forecast equations. The following paragraph 4.2 explains the different data sources and will discuss how satellite data is advected. In the final paragraph, paragraph 4.3, the verification techniques used in the study are presented.

### 4.1 Model Output Statistics

Model Output Statistics (MOS) is the technique that is used in this study to derive forecast equations for thunderstorms. It is a post-processing technique that describes the statistical relationship between predictors from observed or forecasted weather elements and a predictand (Wilks, 2006). Using a logistic regression model, archived records of the predictors and predictand are used to develop probabilistic forecast equations for the occurrence of a certain event. These events (the predictand) can take on only two values (dichotomous), while a predictor can be of any type. The output of the logistic regression model is the probability of the occurrence of an event and provides a measure of forecast uncertainty.

Figure 4.1 contains an overview of the MOS technique and data used in this study. We use predictors from ECMWF and HIRLAM forecasts and predictors from ensembles of advected radar, lightning and MSG data. Logistic regression is used to derive MOS forecast equations for a thunderstorm event, defined as  $> 1$  detected lightning discharge by the SAFIR network. Extended logistic regression is used to derive forecast equations for a severe thunderstorm event, defined for Maximum 5-Minute lightning Intensity (M5MI) thresholds of 50, 100 or 200 discharges under the condition of a thunderstorm event. The used archive of predictors and the predictand is 3 years long, from 2008 to 2010. We use the summer half year only, defined as a period between April 16<sup>th</sup> and October 15<sup>th</sup>. From this dataset,  $\frac{2}{3}$  is used for the derivation of MOS equations and  $\frac{1}{3}$  is used for verification.

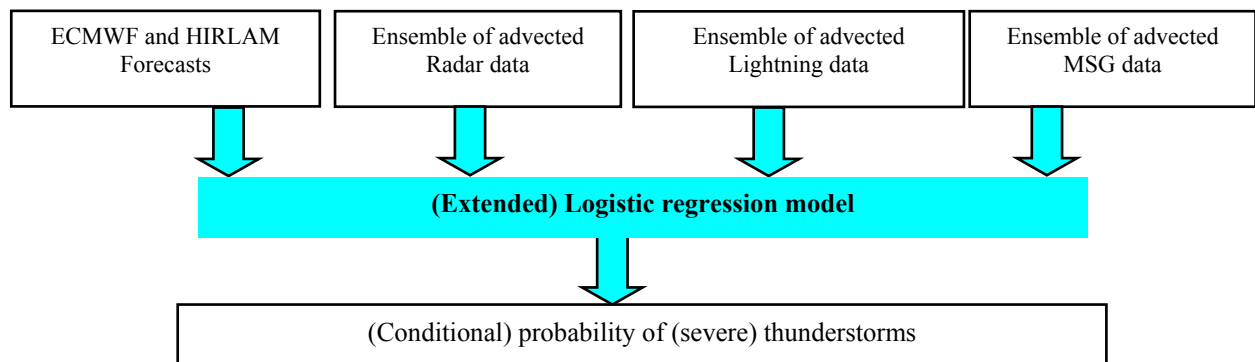


Figure 4.1 MOS system used to create (severe) thunderstorm forecast equations in this study.

Equations are derived for twelve regions of 90 by 80 km<sup>2</sup> over the Netherlands, shown in figure 4.2. In this study, we derive thunderstorm and severe thunderstorm equations for 0 – 6 h projections only. Equations are derived for 8 time intervals: 00 – 06, 03 – 09, 06 – 12, 09 – 15, 12 – 18, 15 – 21, 18 – 24 and 21 – 03 UTC. They are from here on referred to by their central verification time: as 03, 06, 09, 12, 15, 18, 21 and 00 UTC, respectively.

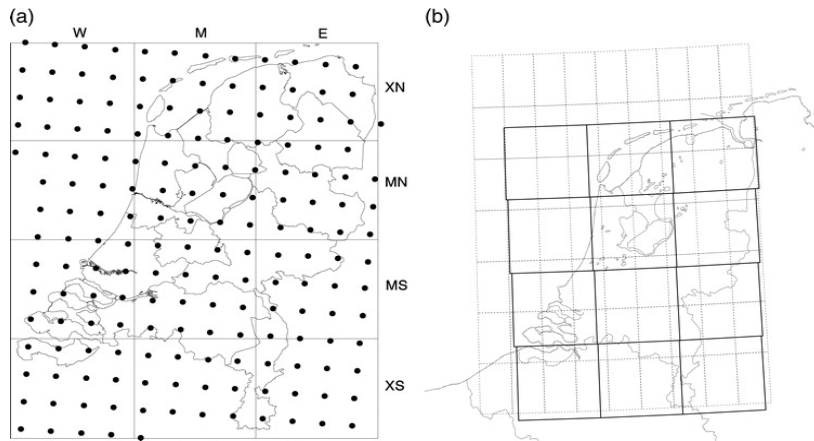


Figure 4.2a The Netherlands subdivided in twelve regions [west (W), middle (M), east (E), north (N), south (S) and extreme (X)]. Province boundaries are also indicated. The black dots represent Hirlam grid points with 22-km horizontal resolution. 4.2b Subdivisions as in a but in a different coordinate system, dotted rectangles, that show the ECMWF grid at a horizontal resolution of  $1/2^\circ$  (from Schmeits et al., 2008).

Logistic regression is used to derive MOS forecast equations for thunderstorm events. Extended logistic regression is however used for the derivation of severe thunderstorm forecast equations. Extended logistic regression has many advantages (Wilks, 2009) that will become apparent further on in this paragraph. The ordinary logistic regression technique is explained first; thereafter we will explain extended logistic regression.

Logistic regression gives the probability (Pr) that a dichotomous event (y) occurs using the formula (Wilks, 2006):

$$\Pr\{y\} = \frac{1}{1 + \exp[-(a_0 + a_1x_1 + a_2x_2 + \dots + a_nx_n)]} \quad (4.1)$$

Where  $x_i$  ( $i=1,2,\dots,n$ ) are the predictors and  $a_i$  ( $i=1,2,\dots,n$ ) the regression coefficients. Predictors are chosen using forward stepwise selection. In each step, a predictor is chosen that produces the best regression together with previously chosen predictors, but excluded from the equation if significance  $> 0.1$ . Predictors are added until none have a significance  $< 0.05$ . Regression coefficients are determined using the maximum likelihood method, in which residuals are assumed to be Bernoulli variables instead of constants (Wilks, 2006). An example of a logistic regression function is shown in figure 4.3. The example shows one predictor, X, used to forecast the probability of the predictand, P. The predictor can take on any value, the probability P is always between 0 and 1.

In the derivation of the MOS equations, data from all regions is pooled. Logistic regression is performed on  $\frac{2}{3}$  of the dataset, which is referred to as the training dataset. From the training dataset, predictors are chosen that create the most skilful thunderstorm forecast. The resulting equations are used for verification by calculating the predicted probabilities for the remaining  $\frac{1}{3}$  of the dataset. Because the forward stepwise selection procedure overfits greatly on the training dataset, predictors are entered separately afterwards until they show no further improvement of the forecasts on the verification dataset. The final equations consist of no more than 5 predictors.

In the currently operational MOS thunderstorm forecasting system, equations were derived using logistic regression for thunderstorms and severe thunderstorms events. There are some difficulties with this technique however as severe thunderstorms are defined as multiple thresholds of M5MI. Different equations have to be derived for separate threshold values, even though the same predictors are used for different thresholds. Forecasts for intermediate threshold values (e.g.  $M5MI \geq 150$ ) would have to be interpolated from the finite collection of MOS equations. In addition, fitting equations to

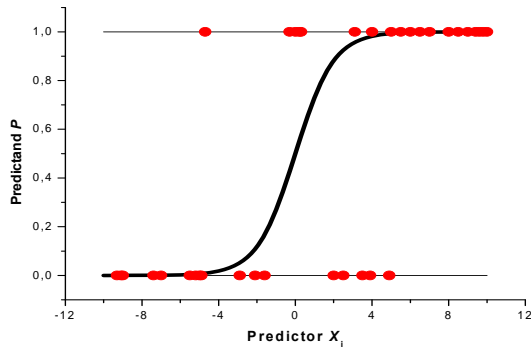


Figure 4.3 Example of a logistic regression function. Observations as a function of the predictor are indicated by red circles.

separate thresholds means that you are left with a relatively small number of yes-events, especially for higher thresholds. But the most severe deficiency of the technique is that the equations derived are not mutually consistent. Higher thresholds could in theory have higher probabilities for some forecasts.

These problems do not apply to thunderstorm forecasts as only one predictand threshold is used (detection of > 1 lightning discharge). The problems do however apply to severe thunderstorm forecasts and may be solved using extended logistic regression, as it gives forecasts for all possible thresholds using only one forecast equation (Wilks, 2009). This is achieved by including a function of the threshold as a predictor. Using extended logistic regression we make sure that forecasts are mutually consistent and all threshold values can be included to obtain forecast probabilities. Furthermore, the technique requires substantially fewer forecast equations and allows for fitting over a larger dataset.

The extended logistic regression formula has the form (Wilks, 2009):

$$\Pr(q) = \frac{1}{1 + \exp[-(a_0 + a_1 x_1 + \dots + a_n x_n + g(q))]} \quad (4.2)$$

Where  $g(q)$  indicates the addition of a function of the threshold,  $q$ , as a predictor. All predictors derived using extended logistic regression are selected similar to logistic regression, except for the fact that  $g(q)$  is included as a potential predictor. In extended logistic regression, severe thunderstorm datasets with different M5MI thresholds are added together.  $g(q)$  is usually an important predictor in the system as it is the only predictor that explains variance in the dataset due to different M5MI thresholds.

The final MOS system thus consist of two equations for each of the 8 forecast times. Thunderstorm forecasts are derived using ordinary logistic regression and severe thunderstorm forecasts are derived using extended logistic regression. The absolute probability of a severe thunderstorm event is obtained by multiplying the conditional probability of a severe thunderstorm by the thunderstorm probability.

#### 4.2 The predictand

As a source of predictands, total lightning data from the SAFIR lightning detection network is used. Both cloud-cloud and cloud-ground lightning discharges have been included. The dataset includes the total amount of lightning flashes in 6 hours and M5MI for twelve previously mentioned regions and for 6 hour time periods.

The predictand for a thunderstorm event is given a value of 0 for ‘no thunderstorm’ (detection of  $\leq 1$  lightning discharge) and a value of 1 for a ‘thunderstorm’ event (detection of > 1 lightning discharge).

A severe thunderstorm event is defined under the condition of a thunderstorm event. A value of 0 is given for M5MI below a certain threshold and a value of 1 for M5MI over that threshold. To derive severe thunderstorm forecast equations for the 15, 18, 21 and 00 UTC forecasts, we combine datasets including M5MI thresholds of 50, 100 and 200 discharges. This choice is based on the relatively high thunderstorm climatology during these times as shown in figure 2.7. During the forecast times of 03, 06, 09 and 12 UTC, severe thunderstorms are observed less frequently and severe thunderstorm forecast equations are derived using a dataset including M5MI thresholds of 25, 75 and 125 discharges.

### 4.3 Potential predictors

This section discusses the data used as potential predictors in the MOS thunderstorm forecasting system. As mentioned above, this data consists of indices calculated from numerical weather prediction model output and ensembles of advected radar, lightning and MSG data. This section explains how the data is used to create potential predictors for the MOS system.

#### 4.3.1 Numerical Weather Prediction model data

Numerical Weather Prediction (NWP) model output is one source of data that we use as potential predictors for the MOS system. NWP models do not contain thunderstorms or lightning as direct output. We do know however that thunderstorms are associated with an unstable atmosphere, high moisture levels and a source of lift. Therefore, indices have been developed from NWP data that may indicate these atmospheric conditions.

As in Schmeits et al. (2008) we use ECMWF NWP model output and thunderstorm indices from HIRLAM. Every 3 hours minimum, maximum and mean values of these potential predictors are calculated for each of the 12 regions. The ECMWF data has a resolution of  $\frac{1}{2}^\circ$ , with 91 vertical levels. We use the 12 UTC run, from which we use output between 12 and 33 h forecasts. HIRLAM output has a resolution of 11 km with 60 vertical levels. Every 6 h new output is available and we use data from the 6 and 9 h forecast.

Thunderstorm indices that have been selected most frequently are described below. References are given to the original papers in which they were documented. Pepler and Lamb (1986) can be consulted for a summary of the different indices.

Boyden Index (Boyden, 1963)

$$BOYD = 0.1 (Z_{700} - Z_{1000}) - T_{700} - 200$$

The Boyden Index describes the vertical temperature profile between 1000 and 700 hPa.  $Z_{700}$  and  $Z_{1000}$  are the geopotential heights of the 700 and 1000 hPa pressure level, respectively and  $T_{700}$  is the temperature ( $^\circ\text{C}$ ) at 700 hPa. The Boyden Index does not take moisture into account.

Bradbury Index (Bradbury, 1977)

$$BRAD = \theta_{w500} - \theta_{w850}$$

The Bradbury Index is also referred to as the potential instability index, as it describes the potential instability between the layers of 850 and 500 hPa.  $\theta_{w500}$  and  $\theta_{w850}$  are the wet-bulb potential temperature values at 500 and 850 hPa, respectively. Wet bulb temperature is defined as the lowest temperature that can be reached by an air parcel after adiabatic evaporation of water.

Convective Available Potential Energy (Moncrieff & Miller, 1976)

$$CAPE = g \int_{LFC}^{LNB} \left( \frac{T_{v_{parcel}} - T_{v_{environment}}}{T_{v_{environment}}} \right) dz$$

CAPE is calculated by integrating the buoyancy from the LFC to the LNB and indicates the maximum kinetic energy available to an air parcel that rises from the LFC to the LNB. Buoyancy is indicated by the part between brackets, where  $T_{v_{parcel}}$  is the virtual temperature of the air parcel and  $T_{v_{environment}}$  is the virtual temperature of the environment.

Modified Jefferson Index (Jefferson, 1966)

$$JEFF = 1.6 * \theta_{w925} - T_{500} - 0.5 (T - T_d)_{700} - 8$$

The Jefferson index assesses the latent instability in the 925 – 500 hPa layer. It uses the wet-bulb potential temperature at 925 hPa and includes the dew point temperature at 700 hPa, which is the temperature to which an air parcel must be cooled to condense to water and increases with decreasing relative humidity.

Showalter Index (Showalter, 1953)

$$SHOW = \theta_{ws500} - \theta_{ws850}$$

The showalter index is defined as the difference between the wet-bulb potential temperature at 850 hPa ( $\theta_{ws850}$ ) and the wet-bulb pseudopotential temperature at 500 hPa ( $\theta_{ws500}$ ).

#### 4.3.2 Ensemble of advected radar and lightning data

A second source of predictors consists of ensembles of advected radar and lightning data. Weather radar and lightning provide good areal coverage and high-resolution data. It is therefore very well suited for nowcasting. Nowcasting is a technique used by meteorologists where forecasts up to 6 hours ahead are developed by extrapolation of observed images. In this time range, extrapolation of observations is usually superior to NWP forecasts.

For the extrapolation of radar and lightning data, the speed and direction of specific weather systems is computed from previous radar images and HIRLAM 700 hPa wind vectors. The calculated vectors are used with initial images 20 minutes before a forecast time and extrapolated over the 6 hour time period. Vectors are varied 25 % in magnitude and 10° in direction to create a total ensemble of 18 members (Schmeits et al., 2008).

Individual ensemble members and characteristics of the whole ensemble are used as potential predictors. Predictors can describe a fraction of the ensemble showing over a certain threshold value. Lightning and radar ensemble predictors that were most frequently selected in the current MOS forecasting system are described below.

From the lightning ensemble data, the percentage of the ensemble members that show  $\geq 4$  lightning discharges in the 6 hour time period was a frequently selected predictor. This predictor can include the total ensemble, but may also be a binary predictor, stating ‘yes’ or ‘no’ whether at least one ensemble member shows  $\geq 4$  lightning discharges in 6 hours. Another frequently selected predictor was the M5MI from the total ensemble or from the HIRLAM advection ensemble.

From the radar ensemble data, the maximum percentage of the region occupied by more than 10 or 30 mm per hour radar pixels from a particular radar ensemble member was selected most frequently. The maximum percentage of the region occupied by radar pixels that show more than 10 or 30 mm per hour for the total advection ensemble was another frequently selected predictor.

#### 4.3.3 Ensemble of advected MSG data

In this research we add an ensemble of MSG derived CPPs as potential predictors to the MOS system. As mentioned in chapter 2, available CPPs are: Cloud Optical Thickness (COT), Cloud Phase (CPH),

Particle Effective Radius (REFF), Precipitation (Precip), Cloud Top Temperature (CTT), Cloud Column Height (CCH), Cloud Water Path (CWP), Cloud Depth (DCLD), Cloud Droplet Density (DNDV) and Downwelling Solar Radiation (SDS).

During daylight hours, the visible light channels from the SEVIRI instrument can be used and all CPPs are available. Whenever zenith angles are over  $72^\circ$  however, only CTTs are available. For the 12, 15 and 18 UTC forecast times, zenith angles are low enough and all CPPs can be used as potential predictors. For the forecast times 21, 00, 03, 06 and 09 UTC, zenith angles are too high and only CTTs are used as potential predictors. Initial images are available at 0815, 1115 and 1415 UTC for forecasts during the day and at 1730, 2030, 2330, 0230, 0530 UTC for forecasts during the night; these are the images used for extrapolation.

For the advection of CPPs, vectors are calculated from subsequent images in the MSG IR  $10.8 \mu\text{m}$  channel using a program called CINESAT ([www.cinesat.com](http://www.cinesat.com)). CINESAT is a software package that is used for analysis and processing of satellite images. The software allows users to calculate Atmospheric Motion Fields (AMF) from the input of two subsequent MSG images (Figure 4.3). AMFs contain displacement vectors, which describe how cloud structures move. Displacement vectors are saved in text files that hold vector information at different point coordinates. AMFs are subsequently interpolated over all grid points available to CPP data.

All CPPs have to be transformed to thunderstorm predictors for a region and time interval. For the parameters REFF, PRECIP, CCH, CWP, DCLD, DNDV the maximum is calculated per region, per 6 hour time period. For COT the temporal maximum regional average value is calculated per 6 hour time period. For CPH maximum amount of pixels representing ice clouds are taken per region, per 6 hour time period and for CTT and SDS minimum values are calculated per region, per 6 hour time period. From here on, the maximum values, maximum regional average value and minimum values will be referred to by CPP name.

Spatially interpolated data is used to advect CPPs in time. Varying vectors in length and direction creates the ensemble. For MSG data, vectors are changed by  $\pm 25\%$  in their x and y-direction and in length. A total ensemble of 9 members is created for each CPP parameter. Different ensemble members and statistics of the whole ensemble are used as potential predictors in the derivation of MOS equations. Maximum, minimum and mean values are calculated but the ensemble can be used in numerous different ways as a predictor source. Predictors for maximum CPP values indicate the fraction of the ensemble exceeding a certain threshold value (e.g. the fraction of the ensemble showing CCH over 10 km). Contrarily, predictors for minimum CPP values indicate the fraction of the ensemble below certain threshold values (for example the fraction of the ensemble with CTT under 220 K). All predictors are also used in binary form. Different predictors may be combined and can for example indicate the fraction of the ensemble showing CTTs under 220 K and precipitation values over 20 mm/h.

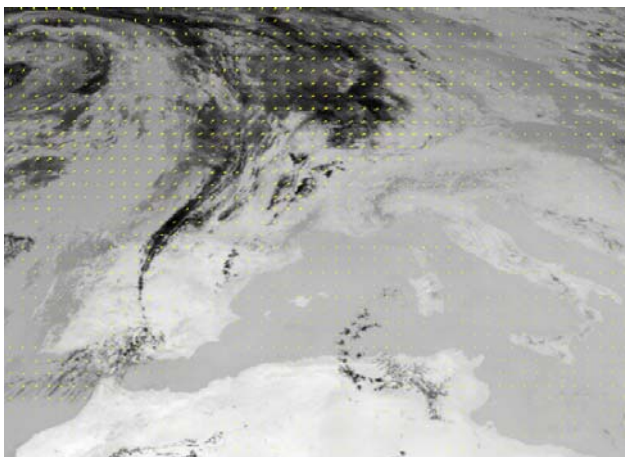


Figure 4.4 Atmospheric motion field calculated from subsequent IR  $10.8 \mu\text{m}$  satellite images for September 10, 2011.

## 4.4 Verification techniques

As indicated in section 3.2,  $\frac{1}{3}$  of the 2008 – 2010 dataset is used for verification purposes during the derivation of MOS forecast equations. Using the logistic regression function based on the training dataset, predicted probabilities are calculated for the verification dataset. These results are used to determine the final MOS equations. When the final MOS system is derived, it will subsequently be verified over a completely independent dataset of the year 2011. This section explains the verification techniques used in this study.

### 4.4.1 The reliability diagram

Predicted probabilities from the MOS equations can be plotted against observed frequencies in a reliability diagram. A reliability diagram provides a comprehensive appreciation of forecast quality, according to Wilks (2006). Figure 4.5 shows 5 characteristic forms of reliability diagrams, where calibration functions are plotted as black circles connected by a line. Comparing the calibration function to a perfectly reliable forecast, indicated by the 1:1 line, we can immediately recognize biases that are exhibited by a forecast.

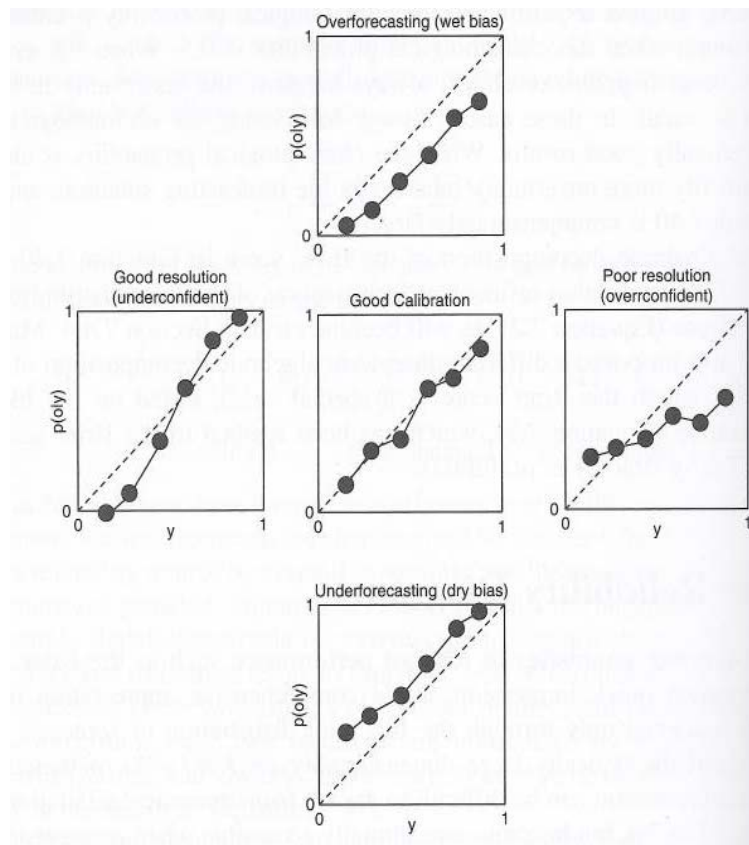


Figure 4.5 Example characteristic forms of reliability diagrams (Wilks, 2006).  $Y$  is the predicted probability,  $p$  the observed frequency of an event. The terms that are given to certain forecast patterns are shown on top.

The centre panel of figure 4.5 shows a well-calibrated forecast. The predicted probabilities are essentially the same as observed frequencies and the calibration line falls along the dashed 1:1 line. Although deviations are still visible, they are consistent with sampling variability. The forecast in the centre panel is said to have excellent reliability. Reliability is the squared difference in vertical distances between the black circles and the 1:1 line, weighted by number. The reliability term of the forecast is small, because these distances are small.

The top and bottom panel show forecasts that are overforecasting or underforecasting, respectively. In the top panel, the calibration line is completely to the right of the 1:1 line. This indicates that the

forecast consistently gives probabilities that are too high (overforecasting). The opposite of overforecasting is underforecasting, where forecasted probabilities are consistently too low. Both these forecasts are unreliable. The predicted probabilities do not correspond to the observed frequencies of the event.

Deficiencies of the forecasts in the left and right panel are more subtle. The magnitudes of biases exhibited by the forecast depend on the forecast itself. In the left panel, lower observed frequencies are overforecasted and higher observed frequencies are underforecasted. The reverse is true for the panel on the right. Another difference between the left and right two panels is resolution. In a forecast with a poor resolution, the observed relative frequencies depend only weakly on the forecasts. All forecasted probabilities are close to the climatological probability of the predictand. The right plot shows a forecast with a poor resolution, the left plot shows a forecast with a good resolution.

We can also indicate whether a forecast is underconfident or overconfident. This can be understood by introducing a forecast distribution, shown in figure 4.6. The left panel is an example of a forecast that deviates only little and rarely from its average value and reflects little confidence. A forecast reflecting high confidence is shown in the right panel. These forecasts are frequently extreme, having probabilities close to either 0 or 1. Whether a certain forecast confidence is justified, can be retrieved from the calibration function of the same forecast. In the right panel of figure 4.5, forecasts are too extreme. Forecast probabilities close to 1 suffer from overforecasting and forecast probabilities close to 0 suffer from underforecasting, making the forecast overconfident. Forecasted probabilities in the left panel of figure 4.5 are however not extreme enough and the forecast is classified as underconfident.

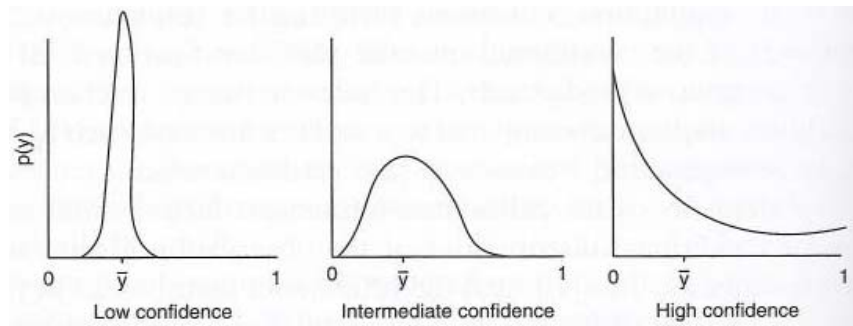


Figure 4.6 Examples of forecast distributions, reflecting forecaster confidence (Wilks, 2006).

#### 4.4.2 The Brier (Skill) Score

Besides the reliability diagram, it is convenient to introduce a scalar measure of forecast accuracy. The Brier score is such a measure and makes it easy to quickly verify how skilful a particular forecast system is. Essentially, the Brier score is just the mean squared error of a probability forecast system. It averages the squared differences between pairs of forecast probabilities and their observations, using the equation (Wilks, 2006):

$$BS = \frac{1}{n} \sum_{k=1}^n (y_k - o_k)^2, \quad (4.3)$$

Where  $k$  denotes the numbering of  $n$  forecast-observation pairs. Brier scores range from 0 to 1. Perfect forecasts have Brier scores of 0 and less accurate forecasts receive higher Brier scores. A Brier score close to 1 indicates an unskillful forecast. A decomposition of the Brier score gives scalar values of a forecast's reliability, resolution and uncertainty. We consider a verification dataset with a discrete number,  $I$ , of forecast values  $y_i$ , where  $N_i$  is the number of times each forecast  $y_i$  is used. If, for each forecast sample in  $I$ , its observed frequency is given by  $\bar{O}_i$  and overall sample climatology by  $\bar{O}$ , a decomposition of the Brier score is given by (Wilks, 2006):

$$BS = \frac{1}{n} \sum_{i=1}^I N_i (y_i - \bar{o}_i)^2 - \frac{1}{n} \sum_{i=1}^I N_i (\bar{o}_i - \bar{o})^2 - \bar{o}(1 - \bar{o}). \quad (4.4)$$

Where the terms on the right hand side represent reliability, resolution and uncertainty of the forecast, respectively. The reliability has to be as small as possible and the resolution term as large as possible, because low Brier scores indicate more accurate forecasts. The uncertainty term is not affected by the forecast and depends only on the overall sample climatology.

From the Brier score a skill score can be computed, referred to as the Brier Skill Score (BSS):

$$BSS = \frac{BS - BS_{ref}}{BS_{perfect} - BS_{ref}} = \frac{BS - BS_{ref}}{0 - BS_{ref}} = 1 - \frac{BS}{BS_{ref}}. \quad (4.5)$$

The BSS compares Brier scores computed from forecasts to reference Brier scores, which are the climatological relative frequencies of the predictand. In this study, that reference is the climatological frequency of (severe) thunderstorm events for a specific forecast time. The higher the BSS the better the forecast is with respect to climatology. Scores of 0 mean that the forecast is equally skillful as climatology. The maximum BSS is 100%.

## 5. Results

This chapter presents the results obtained in this study. The first paragraph gives a general overview of the relation between CPPs and detected M5MI. It is important to understand this relation to create the best possible predictors from advected CPP ensembles. Paragraph 5.2 presents predictors that were selected in the MOS (severe) thunderstorm forecast system from the 2008 – 2010 dataset. Predictors of MOS systems excluding CPP ensemble predictors will also be presented. They are required for the comparison of MOS systems in subsequent paragraphs. To illustrate the MOS forecasts that include CPP ensemble predictors, an example case of September 10, 2011 is presented in paragraph 5.3. The derived equations are verified over the summer half year of 2011 in paragraph 5.4. Brier Skill Scores (BSSs) for all MOS forecast systems are presented. The forecasts for 03 – 09 UTC and 18 – 00 UTC are discussed in more detail by presenting associated reliability diagrams.

### 5.1 Relation between cloud physical properties and lightning intensity

To get a better understanding of how different CPPs relate to lightning intensity, we present correlation coefficients between non-advected CPP values and M5MI for 15 – 21 UTC in table 5.1. Table 5.1 illustrates that some CPPs have higher correlations with M5MI compared to others. Cloud Optical Thickness (COT), Precipitation (PRECIP), Cloud Top Temperature (CTT) and Cloud Column Height (CCH) have the highest correlations coefficients, with values of 0.359, 0.337, -0.329 and 0.344, respectively. CCH, PRECIP and COT are positively correlated while CTT is negatively correlated.

	COT	CPH	REFF	PRECIP	CTT	CCH	CWP	DCLD	DNDV	SDS
M5MI	0.359	-0.139	0.054	0.337	-0.329	0.344	0.069	-0.063	-0.044	-0.138

Table 5.1 Correlation coefficients between different cloud physical properties and M5MI for the 15 – 21 UTC time period. Cloud physical properties include: Cloud Optical Thickness (COT), Cloud Phase (CPH), Particle Effective Radius (REFF), Precipitation (PRECIP), Cloud Top Temperature (CTT), Cloud Column Height (CCH), Cloud Water Path (CWP), Cloud Depth (DCLD), Cloud Droplet Density (DNDV) and Downwelling Solar Radiation (SDS).

Potential predictors have to be created from these variables for the MOS (severe) thunderstorm forecasting system. It is therefore desirable to get a more thorough understanding of the relation between CPPs and M5MI. For this purpose, scatter plots are presented between CPPs with the highest correlation coefficients and M5MI. Plots of CCH, PRECIP, CTT and COT versus M5MI are shown in figure 5.1 from the top left to bottom right, respectively.

Figure 5.1a shows that only high CCH values give high lightning intensities. This is physically plausible as thicker clouds may produce more severe thunderstorms. A cut-off value, above which M5MI is allowed to reach values up to 1100 discharges per 5 minutes seems to be present around CCH values of 10000 m. CTT shows a similar but reverse relation to M5MI; the lowest CTT values show the highest lightning intensities. A cut-off is present around 230 K. PRECIP has a less pronounced relation to M5MI. Relatively high M5MI values occur at precipitation amounts of 0 mm, as the CPP algorithm may detect no precipitation while thunderstorms are present. It is however notable that overall, high precipitation amounts show higher M5MI values. A relation between Cloud Optical Thickness and M5MI is the least obvious from the scatter plots. High M5MI values seem to occur at lower values of COT, which is not expected.

It is possible to create potential predictors for the MOS system using information from scatter plots. As we use ensembles of advected CPPs, predictors may for example describe the fraction of the ensemble with values above or below their cut-off values. For advected CCH ensembles, a predictor may indicate the fraction of the ensemble with CCH values over 10000 m. For advected CTT ensembles, a predictor may indicate the fraction of the ensemble with CTT values below 230 K. The chosen thresholds are arbitrary however and several different threshold values have been investigated. Combination predictors that use information of more than one CPP have also been created.

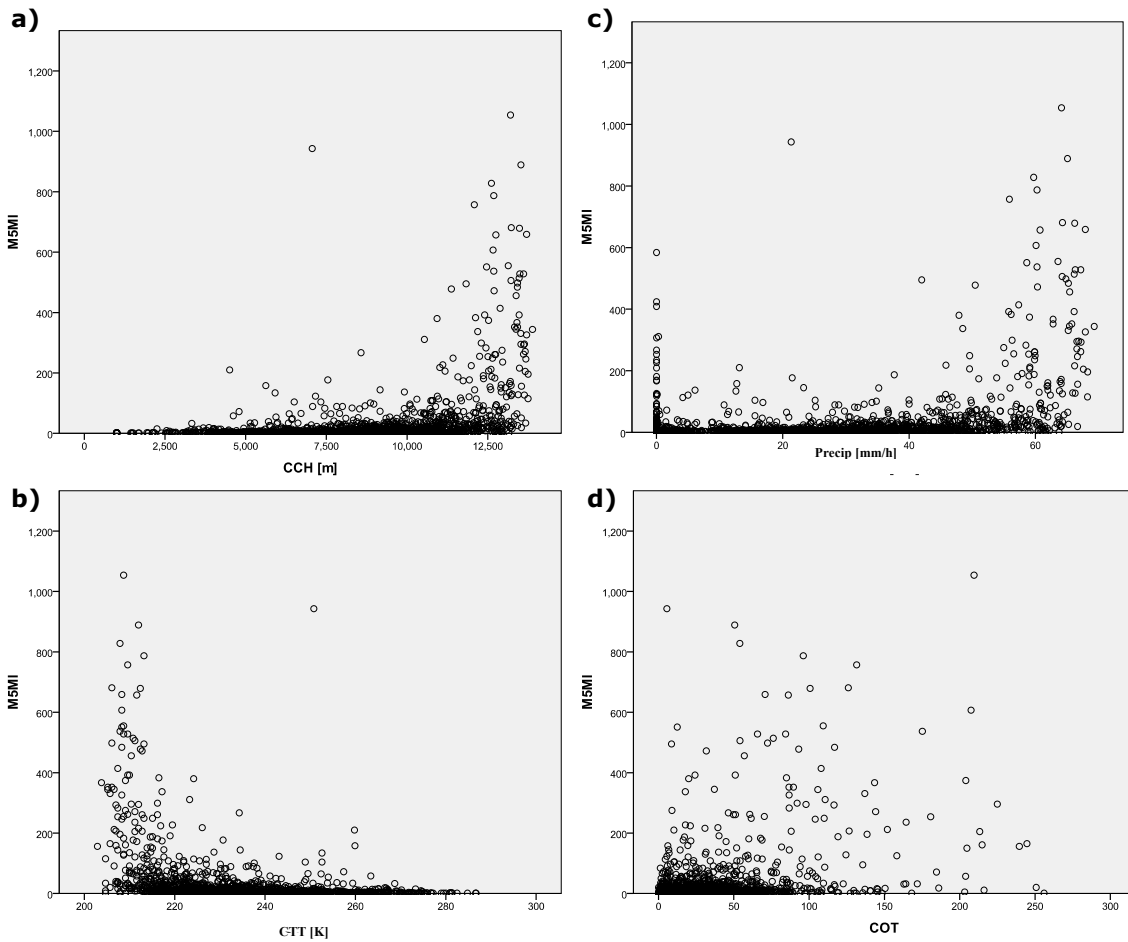


Figure 5.1 Scatter plots of  $M5MI$  versus cloud physical properties for the 15 – 21 UTC time period: cloud column height (CCH), precipitation (precip), cloud top temperature (CTT), cloud optical thickness (COT) are shown from top left to bottom right respectively.

Figure 5.2 shows an example of the relation between advected CTT and  $M5MI$  for the same time period. Although the CPP is advected and is not an instantaneous value of the variable, it still shows a similar relation to  $M5MI$ .

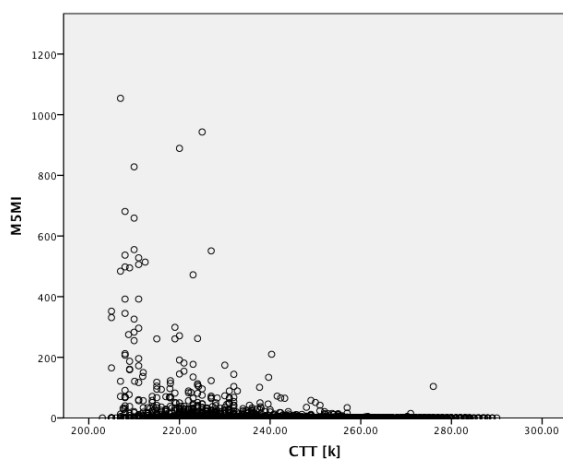


Figure 5.2 Scatter plot of  $M5MI$  versus advected CTT for the 15 – 21 UTC time period.

## 5.2 Selected Predictors

Predictors for the MOS (severe) thunderstorm forecast system have been selected from  $\frac{2}{3}$  part of the 2008 – 2010 dataset using forward stepwise selection. Thereafter, they were separately entered until the forecasting skill on the remaining part of the dataset no longer improved. The selected predictors that make up the final MOS system are presented in table 5.2. Predictors are sorted by system runtime (runtime 00 UTC indicates the forecast for 00 – 06 UTC) and are given in order of importance. Predictor coefficients have not been included, but can be found in appendix 2. The most important predictors are discussed in the text below. Definitions of all predictors can be found in appendix 1. Some similarities of predictors between different runtimes are found; they are presented below.

Runtime (UTC)	Thunderstorm Predictors	Severe Thunderstorm Predictors
00	gt2tpr, capmulma, boydave, rtcp6ec, jeffmax	gt10at, sqrt_thresh, ctt_214bin, mjefmax
03	gt2tpr, capmulma, jeffmax	ctt_214bin, sqrt_thresh, gt10a7ra, showave, maxv300
06	capmulma, jeffave, rtmaxcp6, gt10a7ra	m5mitha, boydave, sqrt_thresh, shearave, jeffmin
09	capmulma, jeffave, rtmaxcp6	bradmin, cos2dtg, sqrt_thresh, jeffmin, m5mi7ra
12	capmulma, jeffave, gt2tpr, rtavecp6	boydmax, jeffave, sqrt_thresh
15	gt2tpr, rtmaxcp6, jeffmax	ctt_213precip_20bin, bradmin, sqrt_thresh, capmulma
18	gt2tpr, capmulma, boydave, rtmaxcp3, ctotmax	m5mitha, ctt_214bin, sqrt_thresh, showave, gt10a7ra
21	gt2tprra, boydave, capemax, showmin	flima9ra, showmin, sqrt_thresh, gt2ib7ha

Table 5.2 Selected predictors for the MOS thunderstorm and severe thunderstorm forecast system, sorted by system runtime and presented in order of importance.

In the MOS thunderstorm forecasting system, 14 different predictors have been selected overall. CAPE is the most selected predictor and appears in all but one equation in two different forms:

- capmulma - maximum value of CAPE from the most unstable level of the atmosphere
- capemax - maximum value of surface based CAPE

Lightning ensemble predictors are chosen as most important predictor at 5 of the 8 forecast times; they are present in two different forms:

- gt2tpr – percentage of total advection ensemble with  $\geq 4$  lightning discharges in 6 hours
- gt2tprra – percentage of radar advection ensemble with  $\geq 4$  lightning discharges in 6 hours

CAPE and lightning ensemble predictors are always accompanied by the Jefferson index (average (Jeffave) or maximum (Jeffmax) value in 6 hours) or by the average Boyden index (Boydave). Furthermore, convective precipitation predictors are frequently included in several different forms:

- rtcp6ec – root of the maximum 6-h convective precipitation sum from the ECMWF model forecast
- rtmaxcp6(3) – root of the maximum 6-h (3-h) convective sum precipitation from the Hirlam forecast
- rtavecp6 – root of the average 6-h convective precipitation sum from the Hirlam forecast

It is noteworthy that whenever a CAPE predictor is chosen as most important, the Jefferson index and a convective precipitation predictor follow directly after. This can be explained when considering the necessary ingredients for thunderstorm development. They include: sufficient instability in the atmosphere, high levels of moisture and a source of lift. A combination of CAPE, Jefferson index and convective precipitation indicates atmospheric conditions favourable to thunderstorm development.

It is furthermore notable that lightning ensemble predictors are usually accompanied by (latent) instability indices (CAPE, Boyden index and / or Jefferson index). Advected lightning indicates that a thunderstorm is approaching, the atmosphere needs to remain unstable however for the thunderstorm to sustain itself. A combination of the previously mentioned predictors suggests that these conditions are present in the atmosphere. The fact that advected lightning ensemble predictors are most important between the 15 UTC and 03 UTC forecast can be explained by looking at thunderstorm climatology over the period of 2008 – 2010, presented in paragraph 2.5. The figure indicates the climatological probability of a thunderstorm at 8 central verification times (03 UTC belongs to the 00 – 06 UTC forecast). It shows that most thunderstorms have developed around 15 UTC. Afternoon thunderstorm may consist more often of multicell storms; they have a longer life cycle and extrapolated observations may be good indication of thunderstorm activity for forecasts between 15 and 03 UTC runtimes. Their predictive importance decreases however, as thunderstorm climatology decreases. Thunderstorms may consist mostly of single cells, which have a relatively short lifecycle and extrapolated observations become less important.

The overall pattern of the thunderstorm and severe thunderstorm predictors is similar. The most obvious difference is the predictor `sqrt_thresh`, which is selected in all severe thunderstorm forecast equations. `Sqrt_thresh` indicates the square root of the M5MI threshold, which is included because of the derivation of severe thunderstorm equations using extended logistic regression.

In most severe thunderstorm forecast equations, predictors from advected ensembles of observations are most important. These predictors come from lightning and radar ensembles, of which the following have not been defined above:

- `gt2ib7ha` – binary predictor indicating whether a particular HIRLAM advection ensemble member shows  $\geq 2$  discharges in 5 minutes
- `m5mitha` – M5MI from the HIRLAM advection ensemble
- `flima9ra` – temporal M5MI from a particular radar advection ensemble member
- `gt10at` – maximum percentage of the region covered by  $\geq 10$  mm h<sup>-1</sup> radar pixels from the total advection ensemble

CPP ensemble predictors have been selected in 4 of the 8 severe thunderstorm forecast equations. They are included in the MOS system in two different forms:

- `ctt_214bin` – a particular ensemble member with Cloud Top Temperatures  $\leq 214$  K in binary form
- `ctt_213Precip_20bin` – a particular ensemble member with Cloud Top Temperatures  $\leq 213$  K and precipitation  $\geq 20$  mm/h in binary form

`Ctt_214bin` has been selected when only CTTs were available (when zenith angles were too high). `Ctt_213Precip_20bin` is a combined cloud physical property ensemble predictor and has been selected as most important predictor for the 15 UTC runtime of the severe thunderstorm forecast system.

In the 09 and 12 UTC runs, advected observations are less important predictors. This is the time when convective systems have not developed thoroughly and instability indices become important predictors, as we have seen in the MOS thunderstorm forecasting system. At 09 UTC the minimum Bradbury index (`bradmin`) was selected, followed by `cos2dtg`. `Cos2dtg` indicates the cosine of the day in the year and states that more thunderstorms are predicted in summer and indicates a possibly less skilful forecast. The verification of different forecasts will be presented in the following paragraphs however.

The MOS systems for which CPP predictors were selected are compared in the paragraphs below to forecasts with no CPP predictors. For this purpose, separate equations have been derived from the 2008 – 2010 dataset for which CPP ensembles were excluded as a potential predictor source. Table 5.3 shows the MOS severe thunderstorm system at runtimes for which CPP predictors were selected (MOS-CPP). It also shows the MOS system that was derived excluding advected CPP ensembles as a

potential predictor source (MOS-NoCPP) and shows predictors of the currently operational MOS system (Operational KOUW).

<b>Runtime (UTC)</b>	<b>Severe Thunderstorm Predictors MOS-CPP</b>	<b>Severe Thunderstorm Predictors MOS-NoCPP</b>	<b>Severe Thunderstorm Predictors Operational KOUW</b>
00	gt10at, sqrt_thresh, ctt_214bin, mjefmax	gt10at, sqrt_thresh, sc3	m5mi7ra, gt10at, vtotave, gt2tpr
03	ctt_214bin, sqrt_thresh, gt10a7ra, showave, maxv300	m5mit, sqrt_thresh, showave, maxv300	m5mit, gt30at, LNBmulma, rtc6ec6
15	ctt_213precip_20bin, bradmin, sqrt_thresh, capmulma	capmulma, bradmin, sqrt_thresh, gt30at	flima9ra, bradave, capmulave
18	m5mitha, ctt_214bin, sqrt_thresh, showave, gt10a7ra	gt10a7ra, bradmin, sqrt_thresh	nodis7ra, bradmax, gt2ib7ha

*Table 5.3 Selected predictors for the derived MOS severe thunderstorm forecasting system, including and excluding cloud physical property ensemble predictors and the currently operational system. Sorted by system runtime and presented in order of importance.*

In MOS-NoCPP, 3 out of 4 derived equations show advected observations as the most important predictor. Two have not previously been mentioned:

- M5mit - M5MI from the total advection ensemble
- Gt10a7ra - temporal maximum percentage of the region occupied by  $\geq 10$  radar pixels from a particular ensemble member

In Operational KOUW, it is notable sqrt\_thresh is not included as a predictor; the equations were derived using logistic regression instead of extended logistic regression. Two important predictors from operational KOUW have not been defined:

- Nodis7ra - average amount of lightning discharges of a particular advected radar ensemble member
- M5mi7ra - M5MI from a particular radar advection ensemble member

It is remarkable that at 18 UTC runtime, where a CPP predictor was selected as non-primary predictor, MOS-NoCPP still contains a different primary predictor. A predictor indicating M5MI from the Hirlam advection ensemble is replaced by a predictor indicating the percentage of a region occupied by a certain precipitation threshold. This is caused by the fact that some cases are missing in the CPP dataset that are available in other predictor datasets. In the operational system all of the most important predictors were lightning ensemble predictors. It is therefore remarkable that at 15 UTC runtime, when thunderstorm climatology is high, CAPE is selected as primary predictor in the MOS-NoCPP system.

### 5.3 Example case September 10, 2011

In this section we demonstrate the derived MOS-CPP system described above. For this purpose, an example case from an independent dataset of the year 2011 is discussed. The year 2011 was not included in the development of the forecast equations and the dataset is thus entirely independent. We choose to present results that belong to September 10, 2011. We use the example case only to illustrate the MOS forecast system; an objective verification over the summer half year of 2011 will be presented in the following paragraph.

September 10, 2011 was a warm summer day with maximum temperatures up to 28 °C in the south of the Netherlands. The synoptic situation is shown in figure 5.3, which is dominated by a low-pressure system situated off the coast of Scotland. The associated flow caused air to be advected over the Netherlands from south / southwest during the entire day. An unstable atmosphere was initially present up to 4000 ft., which increased to further heights toward the end of the day. To release the associated energy, convection had to break through an inversion however. A trough, moving ahead of the cold front caused the inversion break and thunderstorms developed in the late afternoon near the French-Belgian border. KNMI issued a warning for severe weather at 18:32 UTC for the southwestern provinces of the Netherlands and later also for the central provinces.

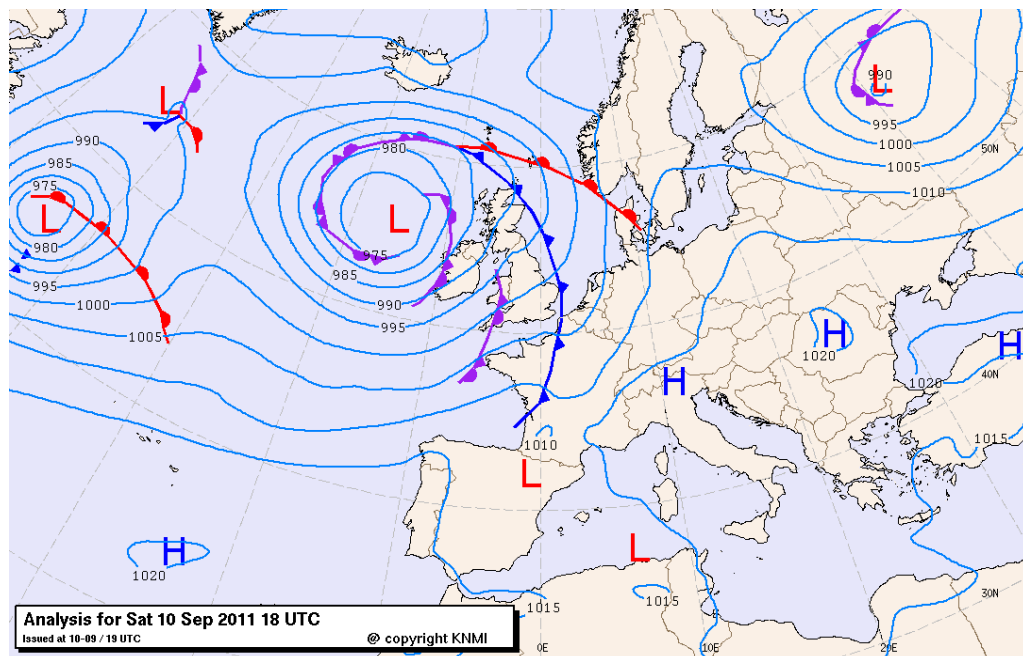


Figure 5.3 Synoptic situation on September 10, 2011.

Figure 5.4 shows the detected lightning strikes on September 10, 2011; time of detection is indicated by colour. The first lightning was detected over the southwest of the Netherlands around 17 UTC and left the northwestern part of the country around 23 UTC. It is therefore interesting to consider MOS forecasts for 15 – 21 UTC and 18 – 00 UTC. Both of these forecast periods include CPP predictors and the newly derived system (MOS-CPP), they can be compared to the operational system that meteorologists had access to on that day (Operational-KOUW).

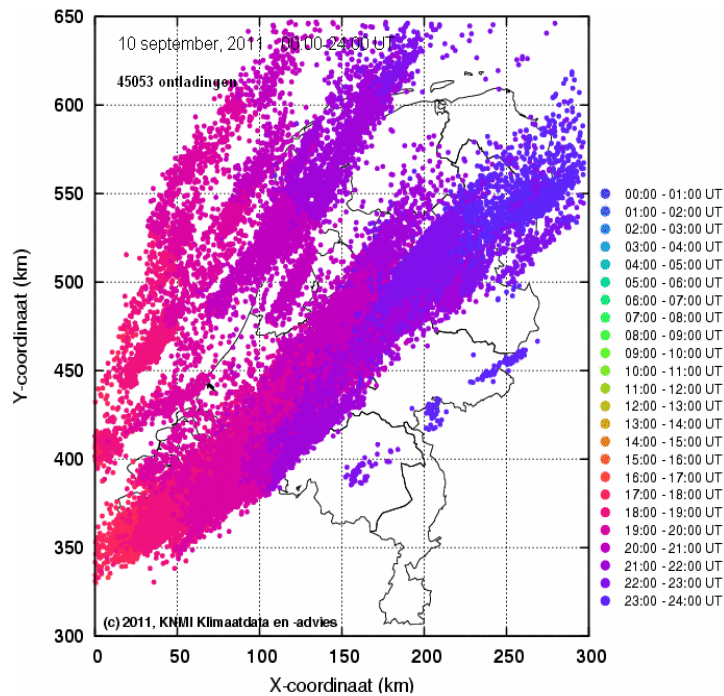


Figure 5.4 Detected lightning strikes over the Netherlands on September 10, 2011. Colours indicate the time of detection.

The severe thunderstorm forecast for 15 – 21 UTC uses a combination predictor indicating a particular ensemble member with cloud top temperatures under 213 K and precipitation rates over 20 mm/h. Figure 5.5 shows the infrared satellite image, derived CTTs and precipitation rates of 14.15 UTC, the initial CPP images used for the 15 – 21 UTC forecast.

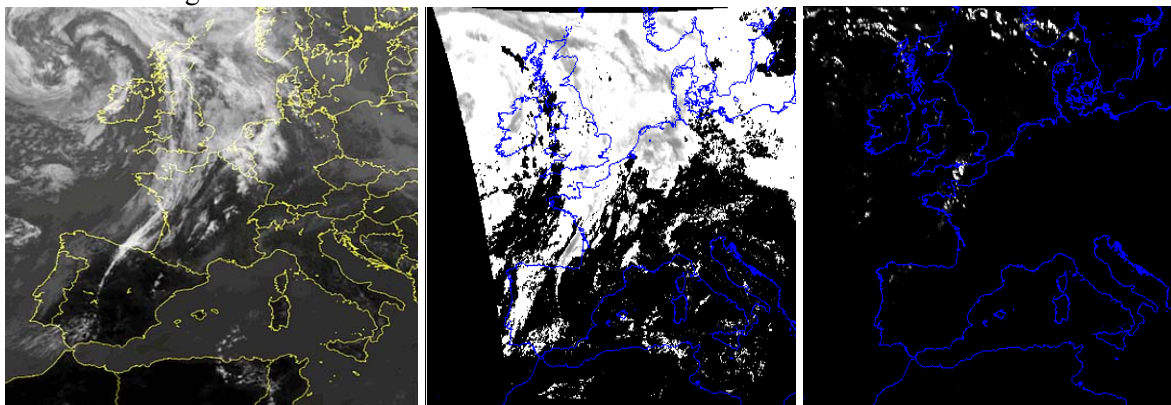


Figure 5.5. Left, infrared satellite image at 14.15 UTC (from buienradar.com). Middle and right, calculated cloud top temperatures and precipitation rates from CPP algorithm at 14.15 UTC September 10, 2011.

The low-pressure system off the coast of Scotland is clearly visible in the infrared satellite picture. The associated cold front shows up as a bright, white line running over western France, extending into Spain. Relatively cold clouds and precipitation are observed around the cold front, especially over the canal just south of England. Over the Netherlands no precipitation is calculated. The south-westerly flow used in the system does however cause the relatively low cloud top temperatures and precipitation values over the canal to be advected towards the Netherlands.

The results of the MOS-CPP system for the 15 – 21 UTC forecast can be found in Figure 5.6a. It shows the probabilities of a thunderstorm event (left), the conditional probabilities for severe thunderstorm event with  $M5MI \geq 200$  (middle) and  $M5MI \geq 400$  (right). Detected  $M5MI$  values can be found at the bottom right. The results show relatively high thunderstorm probabilities in the western and middle parts of the Netherlands. Conditional probabilities of severe thunderstorms are also high in the western regions. Most lightning discharges were detected in the southwestern and middle regions.

Figure 5.6b shows the results of the Operational KOUW system. If results of both systems are compared, we see that they both show high severe thunderstorm probabilities in areas where the highest M5MI values were detected. The probability of  $M5MI \geq 400$  is not high but high lightning intensities were detected in certain regions.

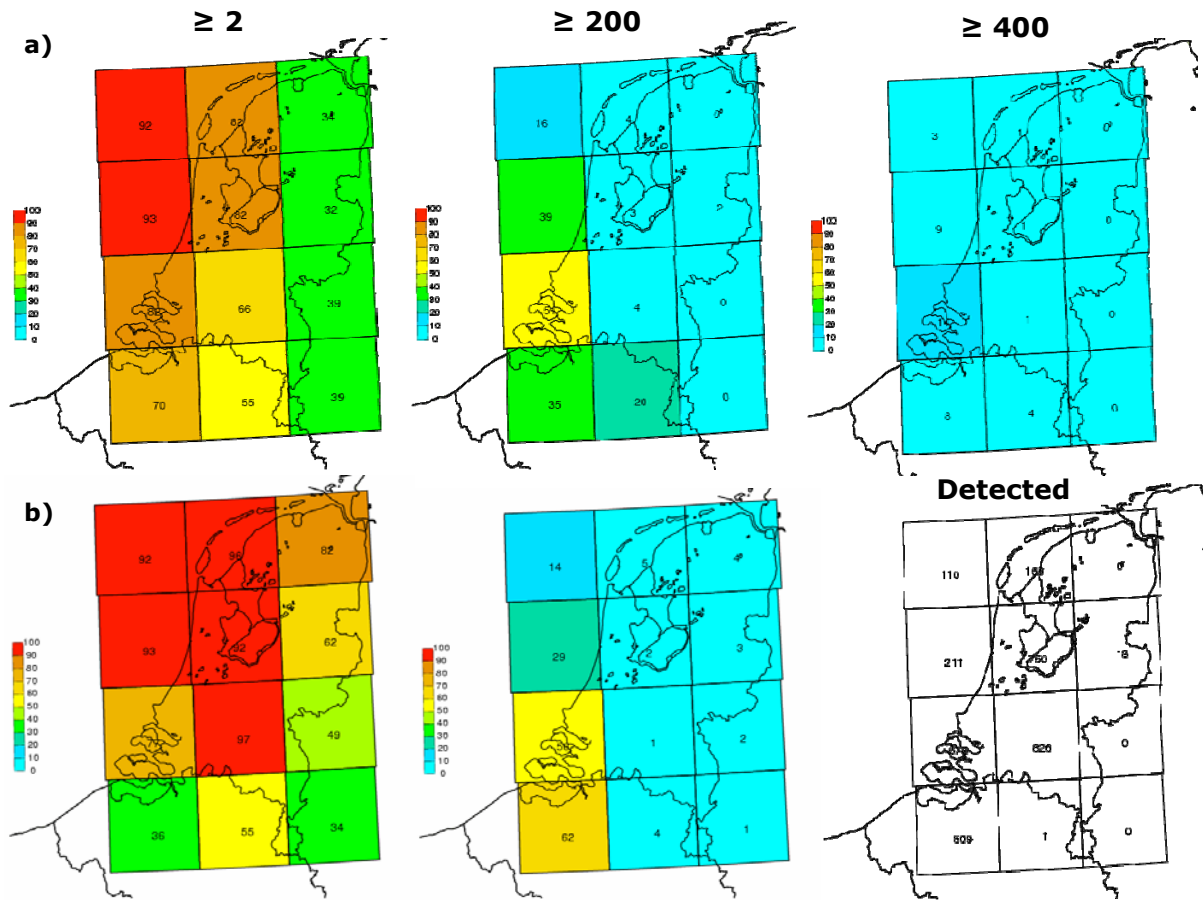


Figure 5.6 a: MOS (severe) thunderstorm forecast system including a CPP predictor. b: Operational MOS (severe) thunderstorm forecast system. Probability forecast of  $\geq 2$  lightning discharges (left), the conditional probability  $M5MI \geq 200$  (middle), and the conditional probability  $M5MI \geq 400$  (right). On the right, bottom: Detected  $M5MI$  values. Forecasts and observations are for 15 – 21 UTC on September 10, 2011.

The severe thunderstorm forecast for 18 – 00 UTC uses a CPP predictor that indicates a particular ensemble member with cloud top temperatures under 213 K. Figure 5.7 shows the initial infrared satellite image at 17.30 UTC used in the forecast. It also shows a magnification of the cloud top temperatures from the red rectangular region. In this region, very low cloud top temperatures were measured (indicated by a dark black colour). These are the CTT values that were advected and used in the forecast for this time period.

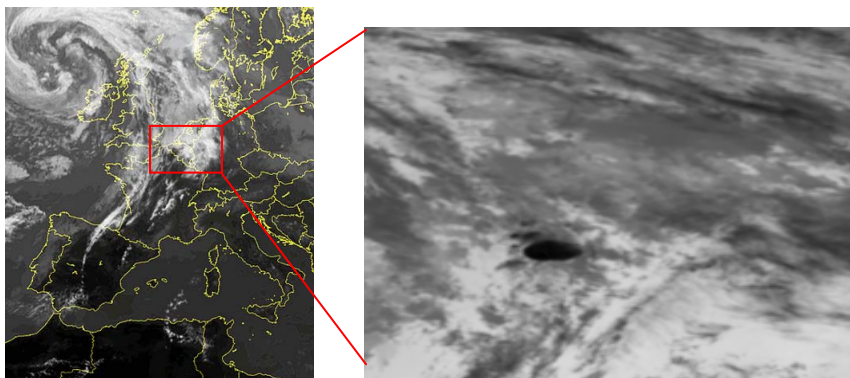


Figure 5.7 Infrared satellite image at 17.30 UTC (from Buenradar.com) and cloud top temperatures calculated by the CPP algorithm from the area indicated by a red rectangle.

The results of MOS-CPP for 18 – 00 UTC on September 10, 2011 are shown in figure 5.8a. Figure 5.8b shows the results for Operational KOUW. MOS-CPP gives higher conditional probabilities of severe thunderstorms in most regions. In all of these areas, high values of M5MI were detected. Even the M5MI  $\geq 400$  forecast shows very high probabilities in areas where high lightning intensities were detected.

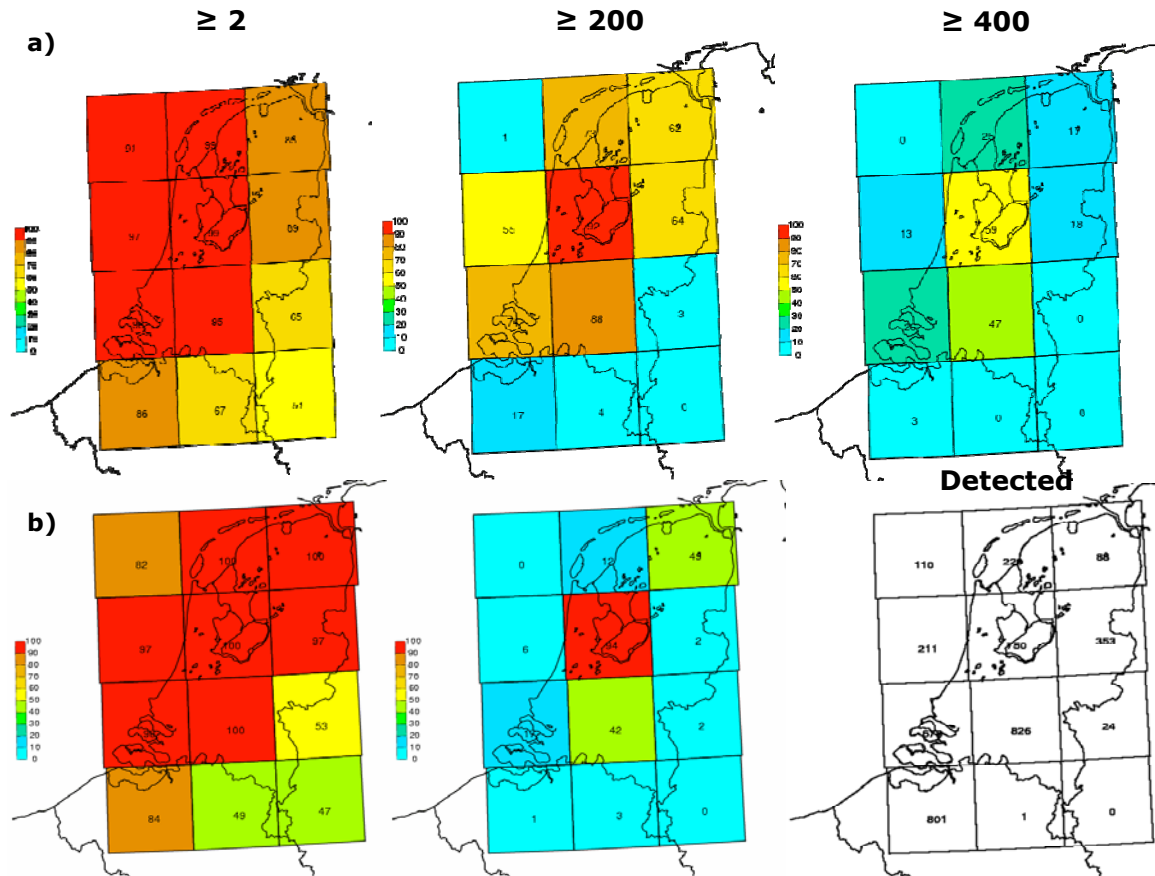


Figure 5.8 a: MOS (severe) thunderstorm forecast system including a CPP predictor. b: Operational MOS (severe) thunderstorm forecast system. Probability forecast of  $\geq 2$  lightning discharges (left), the conditional probability M5MI  $\geq 200$  (middle), and the conditional probability M5MI  $\geq 400$  (right). On the right, bottom: Detected M5MI values. Forecasts and observations are for 18 – 00 UTC on September 10, 2011.

## 5.4 Verification over 2011

In this section, the new MOS-CPP system is verified over the summer half year of 2011. First, the climatological probability of thunderstorms and climatological conditional probability of severe thunderstorms in 2011 is presented. Following are verification scores of MOS thunderstorm forecasts. These scores are discussed only briefly, as they did not include CPP predictors and is therefore of less interest for our research goals. Thunderstorm events do however form the condition for severe thunderstorm forecasts and therefore a brief verification is not left out. Subsequently, verification results for severe thunderstorm forecasts are presented. This MOS system includes CPP predictors in several forecast equations. The verification of these forecasts is of primary interest to this study and they will therefore be discussed thoroughly. MOS-CPP forecasts for which CPP predictors were selected are compared to MOS-NoCPP and Operational KOUW forecasts. They will furthermore be compared to an updated version of the KOUW system, introduced below. All systems are verified using Brier Skill Scores (BSSs). Reliability diagrams are presented for 06 UTC and 21 UTC central verification times.

Climatological probabilities of thunderstorms and climatological conditional probabilities of severe thunderstorms for the different central verification times are presented in figure 5.9 for 2011. Climatological thunderstorm probability increases throughout the daytime and decreases in the evening. The peak of climatological thunderstorm probability is in the afternoon at 15 and the lowest thunderstorm probabilities are found at 03 and 06 UTC. Severe thunderstorms are indicated by M5MI  $\geq 50$ , 100 and 200. The plot looks slightly different compared to thunderstorm climatology. When climatological thunderstorm probability decreases at the end of the day, the conditional probability of severe thunderstorms still increases. This means that although less thunderstorms occur at the end of the day, they are more severe. The severity of thunderstorms does however quickly decrease after 00 UTC, but increases again from 6 UTC onward.

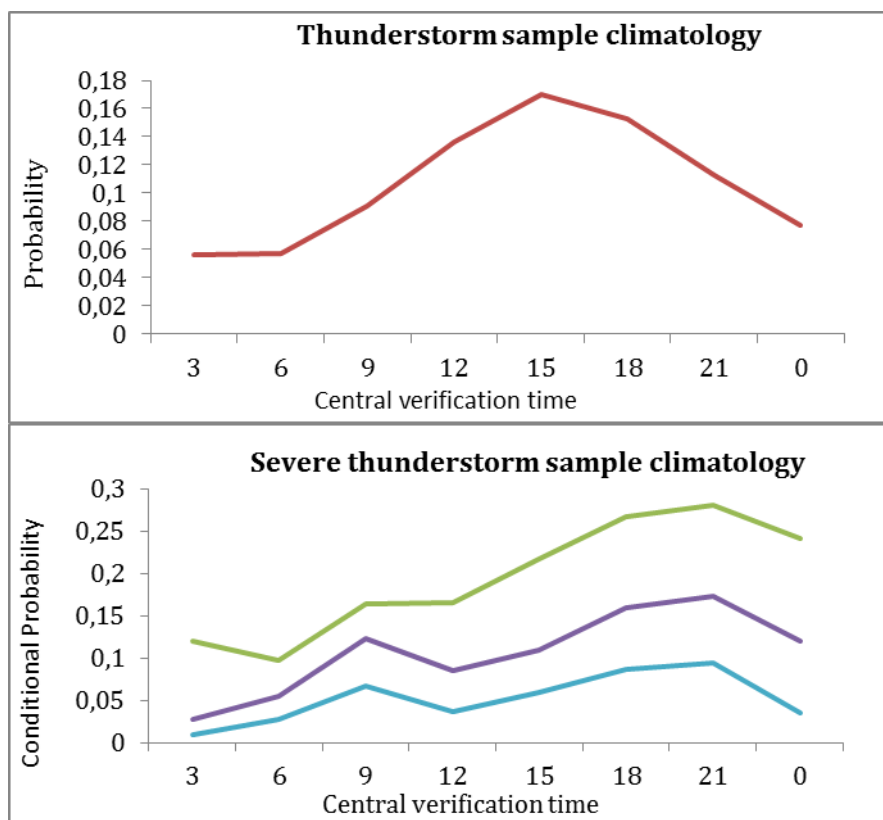


Figure 5.9 Thunderstorm and severe thunderstorm sample climatology. The climatological probability of thunderstorms and climatological conditional probability of severe thunderstorms is plotted against central verification time for the verification period of the summer half year of 2011. For severe thunderstorms, M5MI thresholds of 50 (green), 100 (purple) and 200 (blue) were included.

#### 5.4.1 Verification results of the MOS thunderstorm forecasting system

BSSs of the MOS thunderstorm forecasts are plotted against central verification time in figure 5.10. All regions were pooled to get an overall indication of forecast skill. The skill of the thunderstorm forecasting system increases throughout the day and decreases again at night. It follows thunderstorm climatology quite clearly. Higher climatological probabilities mean that there are more ‘yes’ cases included in the verification of the system. Potential outliers may have less influence on the verification and BSSs are higher.

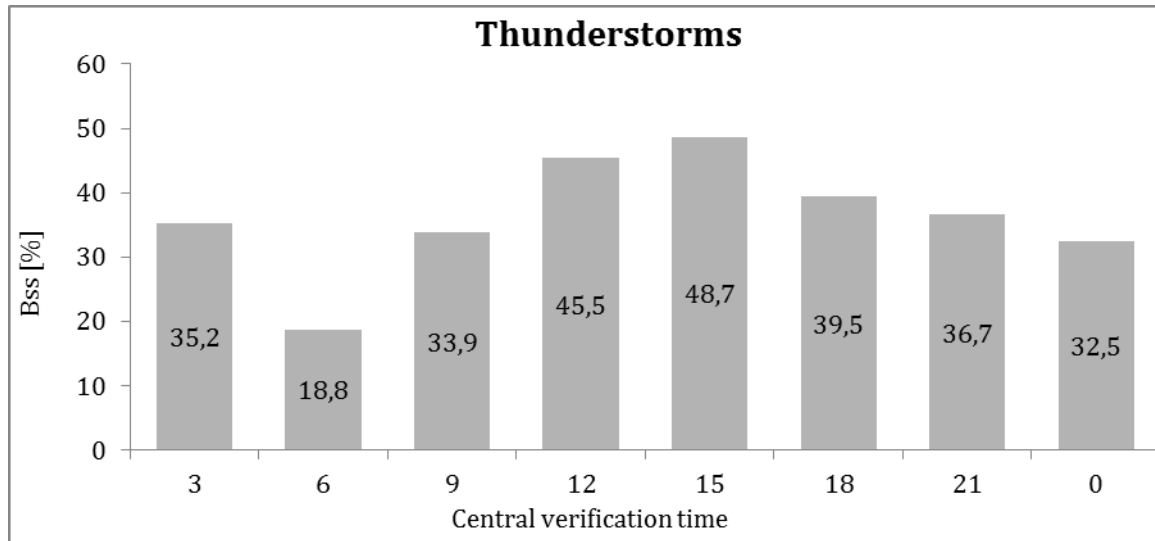


Figure 5.10 Brier skill scores [%] of the MOS thunderstorm forecasts versus central verification time [UTC].

Figure 5.11 shows the reliability diagrams that belong to the forecast of 06 UTC and 21 UTC central verification time, which showed BSSs of 18.8 % and 36.7 %, respectively. Forecast distributions have been added in the top left corner of both figures, for which predicted probabilities are divided into deciles. The desired U-shape of the distributions is however not visible, which is often the case when forecasting rare events. The 21 UTC forecast does however show higher values of predicted probabilities. In the 06 UTC forecast, a probability close to 1 is never issued.

Most points in the calibration line of the 06 UTC forecast are above the perfect-reliability line. This indicates that the forecast probabilities are too low compared to observed frequency indicating underforecasting. It is evident that the 21 UTC forecast is more reliable compared the 06 UTC forecast as most points for the 21 UTC forecast follow the perfect-reliability line closely. The 21 UTC MOS system is also better in terms of resolution.

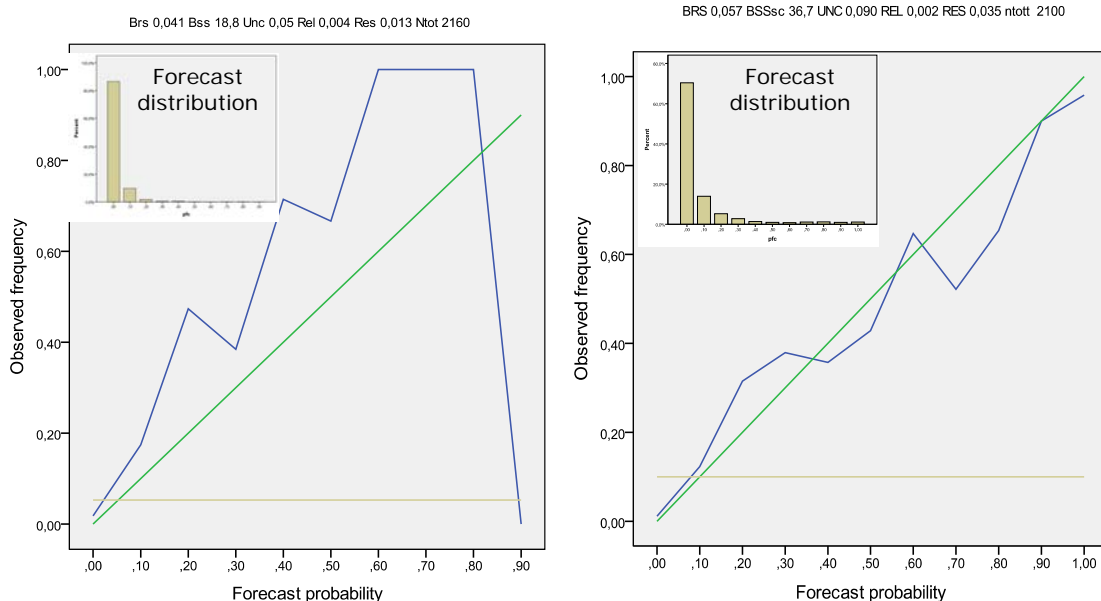


Figure 5.11 Reliability diagrams belonging to the MOS thunderstorm forecasts with central verification times 06 UTC (left) and 21 UTC (right). Brier scores (Brs), Brier Skill Scores (Bss), Uncertainty (Unc), Reliability (Rel), Resolution (Res) and total number of cases (Ntot) are also indicated.

#### 5.4.2 Verification results of the MOS severe thunderstorm forecasting system

The derived equations for the MOS-CPP system include CPP predictors at central verification times 03, 06, 18 and 21 UTC. One of our goals in this research is to quantify if forecast equations including CPP predictors are better compared to forecast equations with no CPP predictors. For this reason we will compare the verification scores of equations including CPP predictors to forecast equations with no CPP predictors. As indicated in section 5.2, this comparison will be done against the MOS-NoCPP and Operational KOUW systems. However, as the coefficients of Operational KOUW have been derived on a dataset from 2002 – 2005, they may be outdated. Model parameters have changed through time and for this reason, we have updated the operational system and derived new coefficients over the 2008 – 2010 dataset. This system will be referred to as Updated KOUW.

Verification results for the severe thunderstorm forecasts of  $M5MI \geq 50$  are shown for the central verification times of all MOS systems in figure 5.12. Operational KOUW is indicated by light grey, Updated KOUW by dark grey, MOS-NoCPP by blue and MOS-CPP by red. If we focus on the overall patterns of BSS in all MOS systems, it seems that BSS follows conditional severe thunderstorm sample climatology of the year 2011 quite closely. BSSs are high when the climatological probability of severe thunderstorms is high.

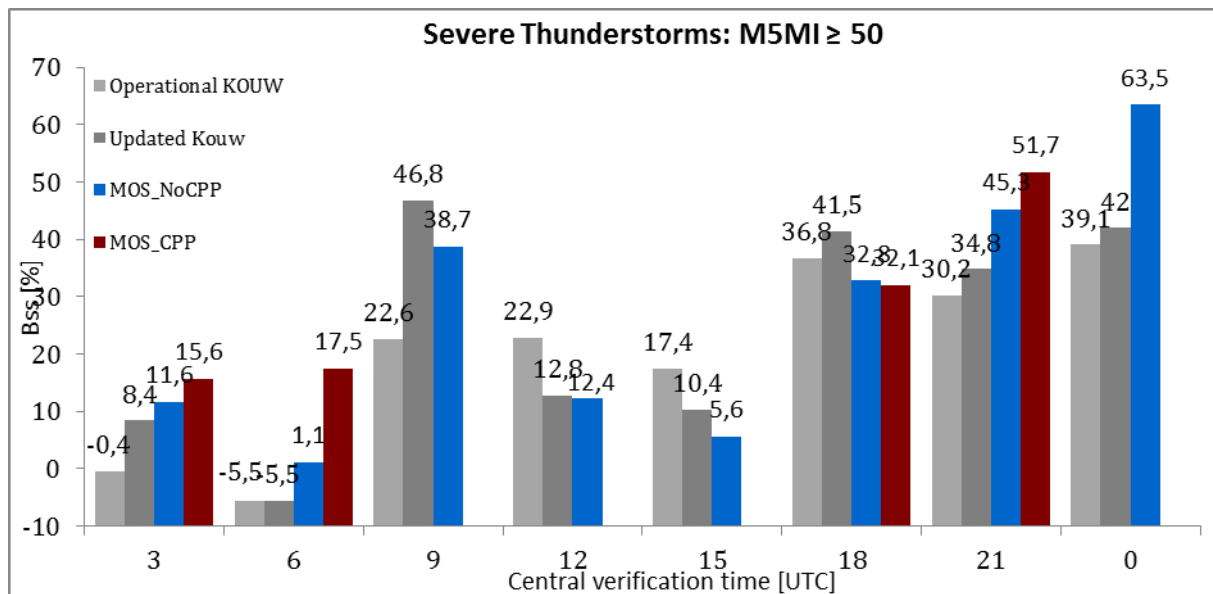


Figure 5.12 Brier skill scores of 4 different MOS severe thunderstorm forecast systems verified for thresholds of  $M5MI \geq 50$  discharges, over the summer half year of 2011. The operational MOS forecasting system at KNMI is indicated by light grey. The updated version of this system is indicated by dark grey. A MOS system derived over the years 2008 – 2010 excluding cloud physical properties is indicated by blue and a MOS system derived over the years 2008 – 2010 including cloud physical properties is indicated by red.

Figure 5.12 shows that the updated version of KOUW provides more skilful forecasts at all but 2 verification times; only at 12 and 15 UTC are the BSSs below Operational KOUW. If we compare MOS-NoCPP and MOS-CPP to Operational KOUW, we see that both new systems outperform operational KOUW at most verification times. MOS-NoCPP is more skilful than operational KOUW at 5 of 8 verification times. Only at 12, 15 and 18 UTC are the BSSs below the scores of the operational system. If MOS-CPP is compared to Operational KOUW, Updated KOUW and MOS -NoCPP, it is more skilful at 3 out of 4 central verification times. MOS-CPP outperforms all other forecasts at 03, 06 and 21 UTC. It is however outperformed at 18 UTC by all systems, but the differences are generally not large.

For the verification times of 15, 18, 21 and 00 UTC we present verification results not only at thresholds of  $M5MI \geq 50$  but also for the higher threshold of  $M5MI \geq 200$ . BSSs belonging to forecasts for  $M5MI \geq 200$  are shown in figure 5.13. For 3 of the 4 forecasts verification times, the new equations derived from the 2008 – 2010 dataset are more skilful compared to Operational KOUW and Updated KOUW. CPP predictors are included in 2 of the 4 verification times, at 18 and 21 UTC. At 18 UTC verification time, all systems excluding CPPs give better verification results compared to MOS-CPP. At 21 UTC, MOS-CPP outperforms all systems. BSSs are only a scalar measure however and not a full representation of forecast quality. Reliability diagrams give a more complete image of forecast quality; they are presented below for 06 and 21 UTC. 06 UTC has a low climatological conditional probability and 21 UTC has a high climatological conditional probability of severe thunderstorms. Reliability diagrams that belong to the verification times of 03 and 18 UTC can be found in appendix 3.

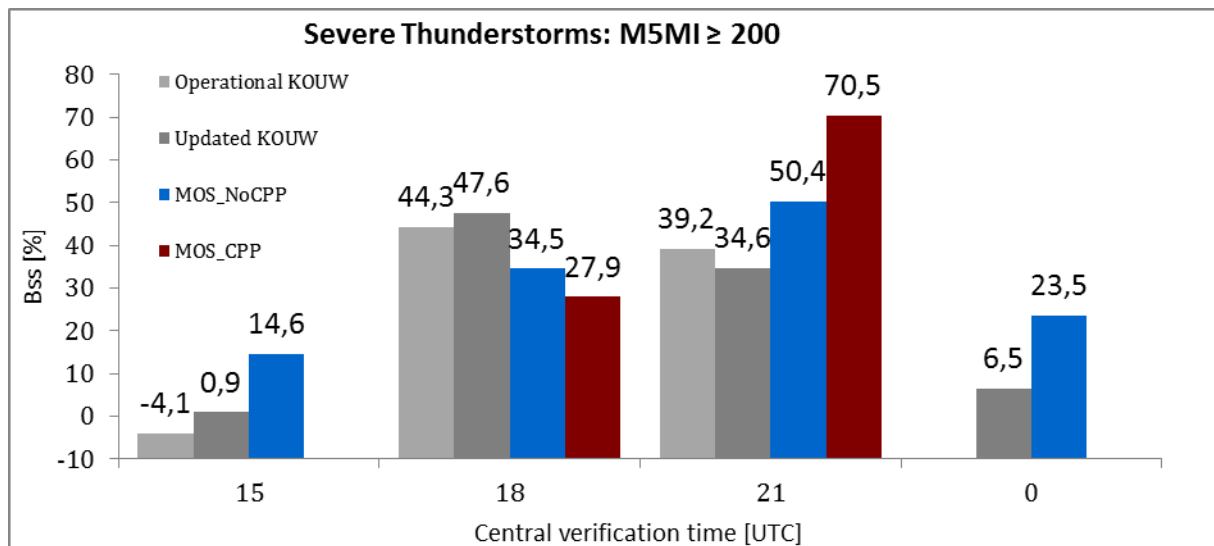


Figure 5.13 Brier skill scores of 4 different MOS severe thunderstorm forecast systems for thresholds of  $M5MI \geq 200$  discharges, verified over the year 2011. The operational MOS forecasting system at KNMI is indicated by light grey. The updated version of this system is indicated by dark grey. A MOS system derived over the years 2008 – 2010 excluding cloud physical properties is indicated by blue and a MOS system derived over the years 2008 – 2010 including cloud physical properties is indicated by red.

Reliability diagrams of the different MOS systems for the 6 UTC central verification time and  $M5MI \geq 50$  forecasts are shown in Figure 5.14. Forecast distributions are included in the figures as well as the scalar measures of the Brier score (Brs), Uncertainty (Unc), Reliability (Rel), Resolution (Res) and total number of cases (Ntot). MOS-CPP, MOS-NoCPP, Updated KOUW and Operational KOUW are shown from the top left to bottom right, respectively.

The figures show that the Operational KOUW and Updated KOUW systems only issued forecast probabilities up to 0.4. Higher forecasted probabilities are favourable as they can increase the resolution of the system. The resolution of KOUW and Updated KOUW is quite weak, with values of only 0.001 and 0.003 respectively. The resolution of the system increases when predictors are selected from the 2008 -2010 dataset. The resolution of MOS-NoCPP is 0.013; the resolution of MOS-CPP is 0.030. The higher resolution of the systems can be seen in the forecast distributions; they show that higher conditional probabilities are more often issued. MOS-CPP forecasts get up to probabilities of 0.80, the highest observed. Although reliabilities of all systems are slightly better than for MOS-CPP; MOS-CPP is still most skilful because of its combination of resolution and reliability. MOS-CPP is thus the preferred forecast system for this time based on the 2011 verification.

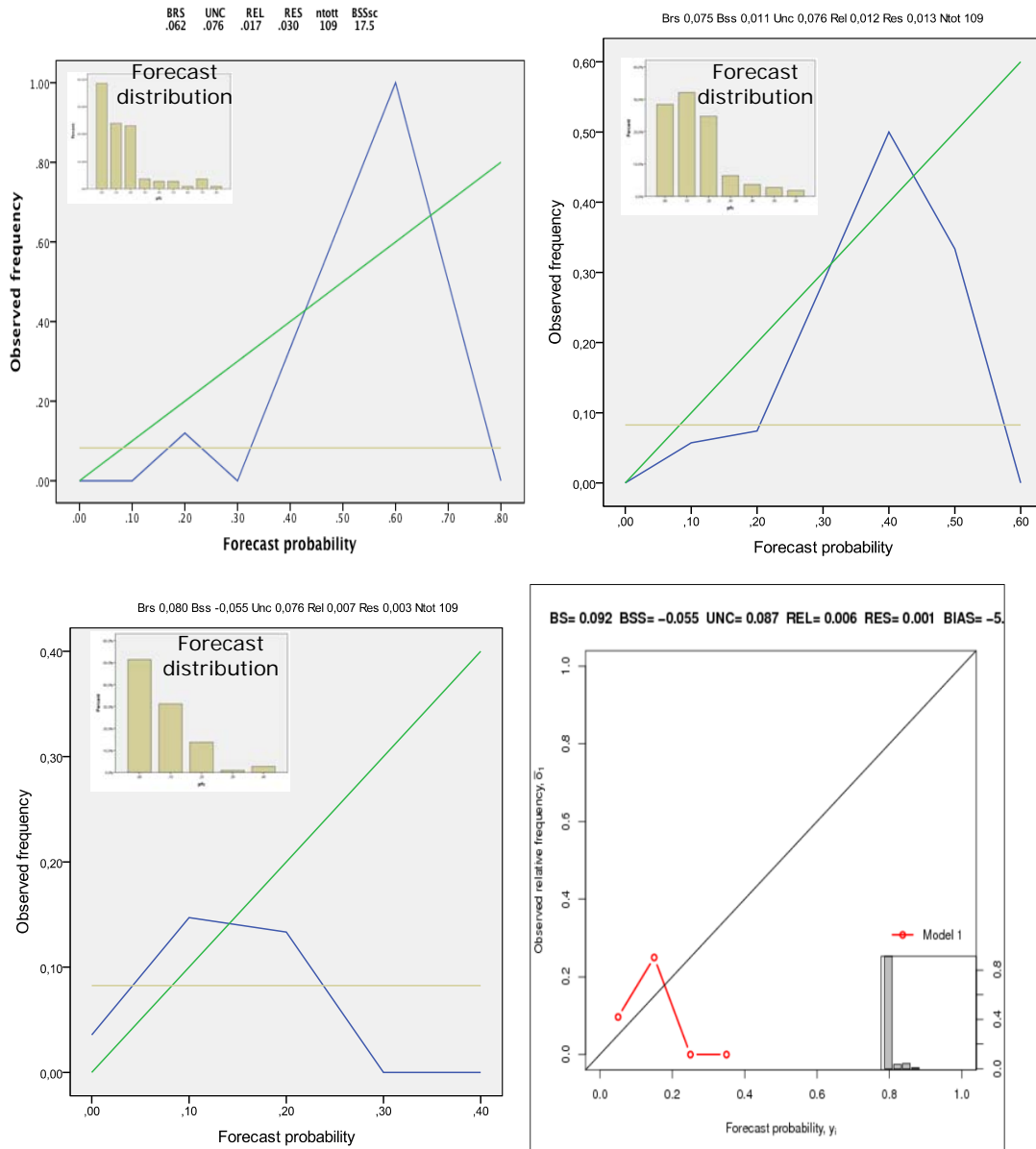


Figure 5.14 Reliability diagrams belonging to the forecast of 03 – 09 UTC for the  $M5MI \geq 50$  forecasts. MOS-CPP, MOS-NoCPP, Updated KOUW and operational KOUW systems are shown from the top left to bottom right respectively. Brier scores (Brs), Brier Skill Scores (Bss), Uncertainty (Unc), Reliability (Rel), Resolution (Res) and total number of cases (Ntot) are also indicated.

Figure 5.15 shows reliability diagrams of the 21 UTC central verification time for the  $M5MI \geq 50$  forecasts. We can see that the updated version of KOUW improved in both resolution and reliability over the operational version. Especially the 0 to 0.4 probability forecasts of Updated KOUW verify well. The operational version shows more ‘jumpy’ behaviour at these lower forecast probabilities. MOS-CPP and MOS-NoCPP seem to perform even better though compared to the KOUW systems. This was already evident from the BSS plots and becomes more clear in the reliability diagrams. The resolution of the system increases substantially and the systems are also more reliable than the operational system. MOS-CPP performs better compared to MOS-NoCPP in terms of resolution. Although MOS-NoCPP has a slightly better reliability, MOS-CPP still performs better overall.

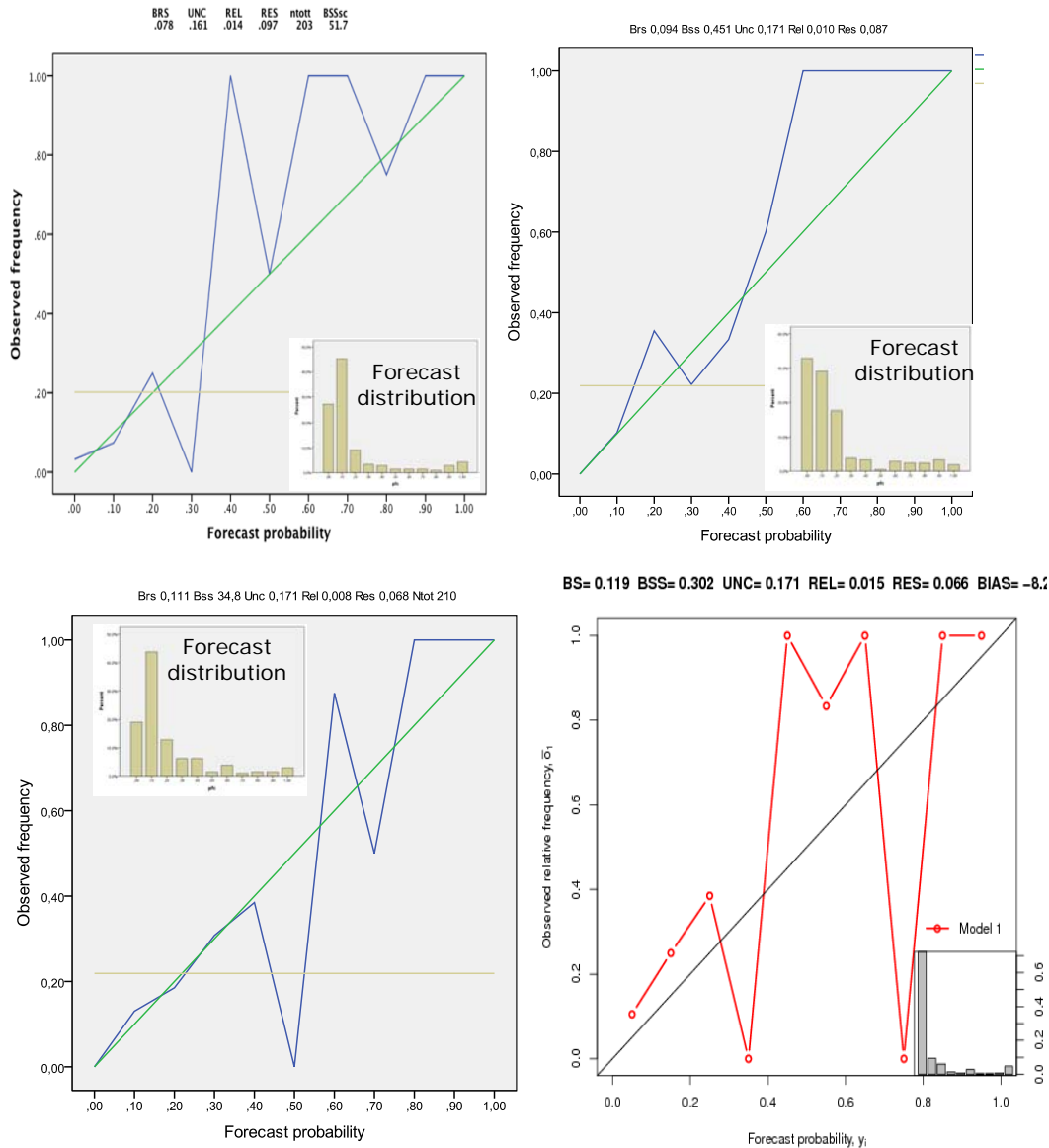


Figure 5.15 Similar to 5.14 but for the  $M5MI \geq 50$  forecast for 18 – 00 UTC.

Figure 5.16 shows the reliability diagrams for the 21 UTC verification time, for the  $M5MI \geq 200$  forecasts. It is obvious that the operational system lacks resolution at this threshold. Resolution increases slightly for the updated system but it does not reach the relatively high resolutions of the newly derived MOS systems. Operational KOUW and MOS-CPP have the best reliability. The highest BSSs were found for the equation including the CPP predictor. It is clearly visible from the reliability diagrams that the MOS-CPP forecast performs best. It has the highest resolution and reliability. MOS-NoCPP underforecasts at all forecast probabilities and including the CPP predictor in the forecast equations clearly makes the forecast better.

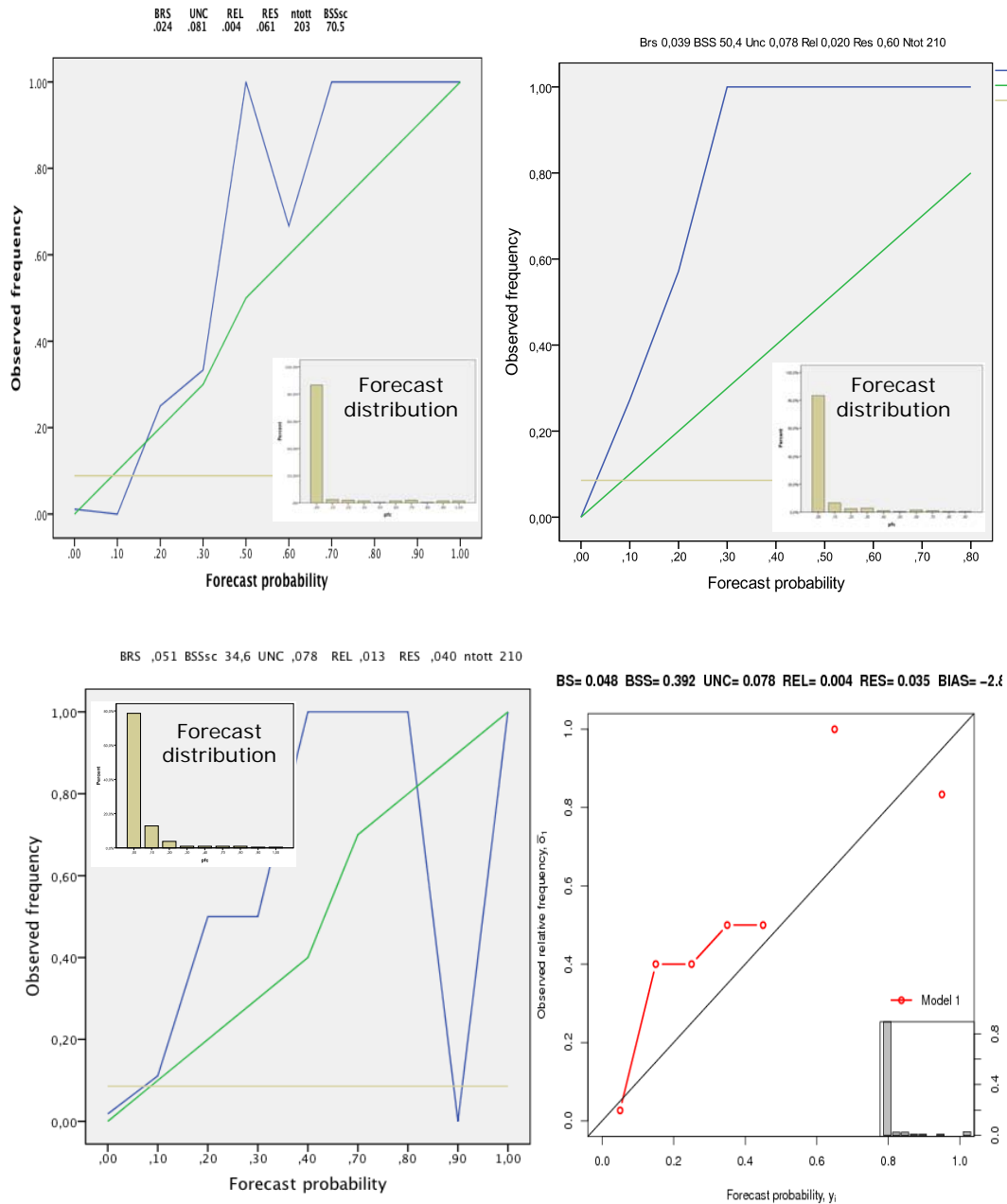


Figure 5.16 Similar to 5.14 but for the  $M5MI \geq 200$  forecast for 18 – 00 UTC.

We end this chapter by showing a very important improvement of the newly derived MOS severe thunderstorm forecast system. The improvement arises due to the use of extended logistic regression in the derivation of the forecast equations. KOUW has only been derived for 3 separate threshold values of M5MI. The threshold of  $M5MI = 200$  was used as the absolute maximum threshold and could only be used during half of the forecast times, because of the otherwise too low climatological conditional probability of such a severe thunderstorm event. Extended logistic regression however allows us to choose any arbitrary threshold of M5MI to make a forecast.

Figure 5.17 shows BSSs as a function of the M5MI threshold for the 8 central verification times of the new MOS system. BSSs are plotted versus M5MI threshold until BSSs becomes negative at more than one M5MI threshold or when no more cases were available to verify the forecast for the M5MI threshold. From the figure, it is evident that skilful forecasts are now possible for specific thresholds far over  $M5MI = 200$  discharges. This characteristic of the new MOS system can be extremely useful to meteorologists, as their main interest is in forecasting very high lightning intensity thunderstorms. A severe weather warning is issued to the public when the subjective probability of over 500 discharges /

5 minutes is more than 60 % for a 50 x 50 km<sup>2</sup> region in the Netherlands. The decision to issue a warning can be further objectified using the new MOS thunderstorm forecasting system.

Overall, BSSs decrease with M5MI threshold. This is expected, as the events become more rare and more difficult to forecast. BSS increase for most systems over the first few M5MI thresholds, however. This might be caused by the choice of M5MI thresholds in the derivation of the MOS system (see paragraph 4.2). Intermediate values of the used threshold values show the highest BSSs. Reliability diagrams that belong to the forecasts of M5MI  $\geq$  300, 400 and 500 can be found in appendix 4.

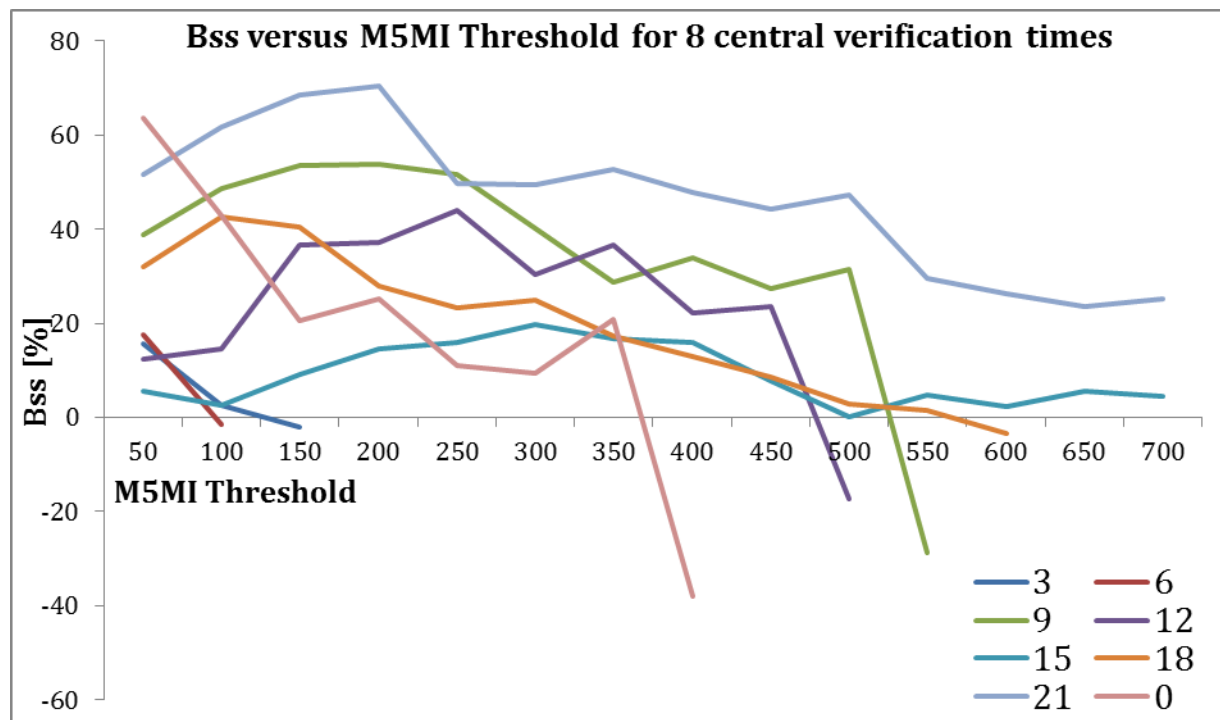


Figure 5.17 BSSs versus M5MI threshold for the newly derived MOS system for 8 central verification times [UTC]. BSS values are excluded if more than 1 M5MI threshold forecast shows BSS < 0, or when no cases were available to verify the forecast for the specific M5MI threshold.

## 6. Summary and Conclusions

In this study, the addition of advected satellite data to the currently operational (severe) thunderstorm forecasting system at KNMI is investigated. The current system is operational during the summer half year from mid-April to mid-October and uses logistic regression equations to predict both the probability of thunderstorms and the conditional probability of severe thunderstorms for twelve regions of 90 by 80 km<sup>2</sup> over the Netherlands. It makes forecasts for 6-h periods up to 2 days ahead and uses predictors from ECMWF and HIRLAM model output and from ensembles of advected radar and lightning data. The latter are used only in the 0-6 h projections.

New forecast equations are derived on a more recent dataset from 2008 – 2010. MSG data is included as an additional potential predictor source for the 0 – 6 h projections. MOS is used to develop probabilistic forecast equations, in which thunderstorm forecast equations are derived using logistic regression and severe thunderstorm forecast equations are derived using extended logistic regression. A thunderstorm is defined as an event where  $> 1$  lightning discharge is detected. A severe thunderstorm is defined as an event with  $\geq 50$ , 100 or 200 discharges / 5 minutes. Conditional probabilities of severe thunderstorms are defined under the condition of a thunderstorm event.

As a source of satellite data, cloud physical properties are used, which are derived from the SEVIRI instrument onboard the MSG satellite. They are advected using atmospheric motion fields, calculated from 30-minute subsequent IR 10.8  $\mu\text{m}$  channel images as input in the CineSat program. Varying the motion vectors in length and direction creates an ensemble, from which potential predictors are created. Of the available advected cloud physical properties, cloud top temperature, cloud column height and precipitation show the best relation to lightning intensity. Cloud column height and precipitation have a positive correlation with lightning intensity; cloud top temperature has a negative correlation.

In the MOS thunderstorm forecast system, no advected satellite predictors have been selected. CAPE was chosen as the most important predictor during runtimes of the system in the morning. Advected lightning ensemble data was chosen as the most important predictor during the afternoon and evening runtimes of the system. Both predictors are frequently accompanied by instability indices or convective precipitation predictors from models.

In the MOS severe thunderstorm forecast system, lightning ensemble predictors are most important overall. Advected satellite data is included in 4 of 8 forecast runtimes (00, 03, 15 and 18 UTC). Advected satellite data yields the second most important predictor two of four times and the most important predictor at 15 and 03 UTC runtime. This indicates that advected satellite data adds value to the forecasts on the 2008 – 2010 dataset. 15 UTC runtime includes a combined predictor indicating a particular ensemble member with minimum cloud top temperatures under 213 K and maximum precipitation values over 20 mm/h. The remaining forecast times include a predictor indicating a particular ensemble member with minimum cloud top temperatures under 214 K. This value is close to 218 K, a value that was found by Mäkelä (2006) as a threshold value, below which lightning intensity is very intense in Finland. The forecast equations change when advected satellite data is excluded in the derivation of the equations. It often includes an advected lightning ensemble predictor and instability indices.

When equations are verified over the independent dataset of 2011, forecast skill of the thunderstorm forecast system increases when the climatological probability of thunderstorms increases. This same pattern is observed for severe thunderstorm forecasts; their skill increases when the conditional probability of severe thunderstorms increases. Verification scores of forecasts including advected satellite data are compared to the currently operational system and to the forecast equations derived excluding advected satellite data. The operational system is furthermore updated on the 2008 – 2010 dataset and included in the analysis. For 00, 03, 15 and 18 UTC runtimes, verification scores of forecasts for  $M5MI \geq 50$  are compared and for 15 and 18 UTC the scores of forecasts for  $M5MI \geq 200$  are compared as well.

Forecasts including advected satellite data are more skilful compared to all other systems at 3 of 4 runtimes for the  $M5MI \geq 50$  forecast. It is only outperformed by the other systems in the forecast of 15 – 21 UTC. The systems that include advected satellite data performs best in the forecast of  $M5MI \geq 200$  for 18 - 00 UTC. For the 15 – 21 UTC forecast of  $M5MI \geq 200$  it is outperformed by all other systems.

Overall it can be concluded that the system including advected satellite data increases forecast skill compared to the currently operational system, even if the system is updated. It is generally also more skilful than a system derived over the same dataset but excluding satellite data. A very important advantage of the new system arises due to the use of extended logistic regression in the derivation of the MOS equations. Forecasts can be made for any arbitrarily chosen  $M5MI$  threshold using the new MOS system, as a function of the threshold is included in the equations. The system shows skilful forecasts up to very high  $M5MI$  thresholds. This characteristic is very useful to meteorologists and is much more difficult to achieve using ordinary logistic regression.

It would however be recommended to verify the system over more years. If the new system remains more skilful, it is recommended to change the currently operational system to the new system. For further development of the MOS thunderstorm forecast system, we recommend to include data from the new Harmonie model when a reforecasting dataset will be available. Harmonie is a non-hydrostatic model and may provide very valuable information to MOS thunderstorm forecasting, because of its very high resolution and because vertical air motion is resolved explicitly. Harmonie will replace Hirlam in the future as operational model at KNMI and Hirlam indices in MOS systems should therefore be replaced by Harmonie indices. Data from GLAMEPS may furthermore be included as potential predictors. GLAMEPS (Iversen et al., 2011) is a multi-model short range ensemble prediction system and may also yield valuable information for MOS thunderstorm forecasting.

### *Acknowledgements*

I would like to thank everyone that supported me in my research. Besides family and friends, they include my colleges Paul de Valk, Rudolf van Westrhenen and Ernst de Vreede who provided me with data and software. My supervisors Rob Roebeling and Aarnout van Delden have always been very helpful and came up with great ideas.

I would especially like to thank Maurice Schmeits. I had a great time and was very fortunate to have you as a supervisor.

## References

- Boyden, C.J., 1963: A simple instability index for use as a synoptic parameter. *Meteor. Mag.*, 92, 198 - 210
- Bradbury, T.A.M., 1977: The use of wet-bulb potential temperature charts. *Meteor. Mag.*, 106, 233 - 251
- Browning, K., Blyth, A., Clark, P., Corsmeier, U., Morcrette, C., Agnew, J., Ballard, S., Bamber, D., Barthlott, C., Bennett, L., et al. (2007). The convective storm initiation project. *Bulltin of the American Meteorological Society*, 1939 – 1955.
- CarbajalHenken, C.K., M.J. Schmeits, E.L.A. Wolters and R.A. Roebeling, 2009: Detection of Cb and TCu clouds using MSG-SEVIRI cloud physical properties and weather radar observations. KNMI publication: WR-2009-04.
- Cotton W.R., 1990: *Storms*, Geophysical Science Series, Vol. 1. Aster press. Fort Collins, CO.
- Deierling, W. K., 2006: The relationship between total lightning and ice fluxes. Ph.D. Dissertation, Univ. of Alabama Huntsville, 175 pp.
- Dosswell, C., 2001: *Severe convective storms*. American Meteorological Society, Boston, USA.
- Glahn, H. R., and D. A. Lowry, 1972: The use of model output statistics (MOS) in objective weather forecasting. *J. Appl.Meteor.*,11,1203–1211.
- Haklander, A. J. and Van Delden, A. 2003: Thunderstorm predictors and their forecast skill for the Netherlands. *Atmospheric Research*, 67-68, 273-299
- Holton, J., 2004: *An introduction to dynamical meteorology*. Academic press.
- Houze, R.A., 1993: *Cloud Dynamics*, Academic Press, 573pp
- Iribarne, J.V. and W. L. Godson, 1973. *Atmospheric Thermodynamics*, Reidel, Dordrecht Holland
- Iversen, T., Deckmyn, A., Santos, C., Sattler, K., Bremnes, J. B., Feddersen, H. and Frogner, I.-L. (2011), Evaluation of ‘GLAMEPS’ – a proposed multimodel EPS for short range forecasting. *Tellus A*: 513-530.
- Jacob, D.J., 1999: *Introduction to Atmospheric Chemistry*, Princeton University Press
- Jefferson, G. J., 1966: Instability index. *Meteor. Mag.*, 95, 381-382
- Johns, R.H., and Doswell, C.A. 1992: Severe local storms forecasting. *Wea. Forecasting*, 7, 588-612
- Jolivet, D. and Feijt, A., 2003: Cloud thermodynamic phase and particle size estimation using the 0.67 and 1.6  $\mu\text{m}$  channels from the meteorological satellites. *Atmospheric Chemistry and Physics Discussions*, 4461 - 4488
- Lilly, D. K. 1990: Numerical prediction of thunderstorms - has its time come? *Quart. J. Roy. Meteor. Soc.* 116, 779-798
- Kessler, E., 1986: *Thunderstorm morphology and dynamics*. University of Oklahoma Press

- Kruizinga, S., 1979: Objective Classification of Daily 500 mbar Patterns. Sixth conference on Probability and Statistics in Atmospheric Sciences, October 9-12 Banff, Alberta, Canada. Published by the American Met. Soc., Boston, Mass
- Lemcke, C and Kruizinga, S. 1988: Model Output Statistics Forecasts: Three Years of Operational Experience in the Netherlands. Monthly Weather Review MRWEAB Vol. 116, No. 5, p 1077-1090
- Mäkelä, A., 2006: Comparison between lightning data and cloud top temperatures in Finland. EUMETSAT Meteorological Satellite Conference paper
- Moncrieff M. W., Miller, M.J., 1976: The dynamics and simulation of tropical cumulonimbus and squall lines. J. R. Meteorol. Soc. 373-94
- Peppler, R.A. and Lamb, P.J., 1989: Tropospheric static stability and central North American growing season rainfall. Mon. Wea. Rev. 117, 1156 - 1180
- Petersen, Walter A., Wiebke K. Deierling, Michael L. Gauthier, Hugh J. Christian, 2006: Precipitation Ice and Lightning: From Global to Cell Scales
- Rakov, V.A., Uman, M.A. 2003: Lightning, Physics and Effects. Cambridge University Press, 687 pp.
- Rinehart, R., 2006: Radar for meteorologists. Rinehart Publications.
- Roebeling R. A., 2008: Cloud Properties Retrieval for Climate Studies using SEVIRI and AVHRR data, PhD Thesis
- Roebeling R.A. and I. Holleman, 2009, SEVIRI rainfall retrieval and validation using weather radar observations, J. Geophys. Res. , 114
- Roelofs G., 2010: Syllabus 'Aerosol, Clouds, Radiation' for the course: Atmospheric composition and chemical process, University of Utrecht
- Schmeits, M.J., C.J. Kok, Daan H. P. Voogelezang, 2005: Probabilistic Forecasting of (Severe) Thunderstorms in the Netherlands Using Model Output Statistics, 134. Weather and Forecasting 20
- Schmeits, M.J., C.J. Kok, D.H.P. Voogelezang and R.M. van Westrhenen, 2008: Probabilistic forecasts of (severe) thunderstorms for the purpose of issuing a weather alarm in the Netherlands. Weather and Forecasting, 1253-1267
- Showalter, A.K., 1953: A stability index for thunderstorm forecasting. Bull. Amer. Meteor. Soc, 34, 250 - 252
- Stammes, P., 2001: Spectral radiance modelling in the UV-visible range. IRS 2000: Current Problems in Atmospheric Radiation, 385 - 388
- Wessels, H.R.A., 1998: Evaluation of a radio interferometry lightning positioning system. Scientific report KNMI, WR-98-04. De Bilt, The Netherlands, 26 pp
- Wilks S., 2006: Statistical Methods in the Atmospheric Sciences, Second edition. Department of Earth and Atmospheric Sciences, Cornell University. Volume 91, International Geophysics Series
- Wilks S., 2009: Extending logistic regression to provide full-probability distribution MOS forecasts. Meteor. Appl., 16, 361-368

# Appendix 1

## Definitions of all predictors used in the MOS systems (alphabetical order)

Boydave – average value Boyden index from the Hirlam forecast

Bradave– minimum value of Bradbury index from the Hirlam forecast

Bradmax – maximum value of Bradbury index from the Hirlam forecast

Bradmin – minimum value of Bradbury index from the Hirlam forecast

Capemax - maximum value of surface based CAPE

Capmulave - average value of CAPE from the most unstable level of the atmosphere

Capmulma - maximum value of CAPE from the most unstable level of the atmosphere

Ctotmax – maximum value of Cross Totals index from the Hirlam forecast

Ctt\_213Precip\_20bin – particular ensemble member with Cloud Top Temperatures  $\leq 213$  K and precipitation  $\geq 20$  mm/h in binary form

Ctt\_214bin – particular ensemble member with Cloud Top Temperatures  $\leq 214$  K in binary form

Flima9ra – temporal Maximum 5-minute lightning intensity (M5MI) from a particular radar advection ensemble member

Gt10a7(9)ra - temporal maximum percentage of the region occupied by  $\geq 10$  radar pixels from a particular ensemble member

Gt10at – maximum percentage of the region occupied by  $\geq 10$  mm h<sup>-1</sup> radar pixels from the total advection ensemble

Gt2ib7ha – binary predictor indicating whether a particular HIRLAM advection ensemble member shows  $\geq 2$  discharges in 5 minutes

Gt2tpr – percentage of total advection ensemble with  $\geq 4$  lightning discharges in 6 hours

Gt2tprra – percentage of radar advection ensemble with  $\geq 4$  lightning discharges in 6 hours

Gt30a7ra - temporal maximum percentage of the region occupied by  $\geq 30$  radar pixels from a particular ensemble member

Gt30at – maximum percentage of the region occupied by  $\geq 30$  mm h<sup>-1</sup> radar pixels from the total advection ensemble

Jeffave – average value of Jefferson index from the Hirlam forecast

Jeffmax – maximum value of Jefferson index from the Hirlam forecast

Jeffmin – minimum value of Jefferson index from the Hirlam forecast

Lnbmulma – Maximum level of neutral buoyancy in the most unstable atmospheric level from the Hirlam forecast

M5mit – M5MI from the total advection ensemble

M5mitha – M5MI from the HIRLAM advection ensemble

Maxv300 – maximum meridional air speed at 300 hPa from the ECMWF model

Mjeffmax – maximum value of the modified Jefferson index from the Hirlam forecast

Nodis7ra - average amount of lightning discharges of a particular advected radar ensemble member

Rtavecp6 – root of the average convective precipitation from the Hirlam forecast

Rtcp6ec(6) – root of the maximum convective precipitation from the ECMWF model forecast

Rtmaxcp6(3) – root of the maximum convective precipitation from the Hirlam forecast

Sc3 – P27 score indicating the change in direction of air flow at 500 hPa in western Europe from the ECMWF model

Showave – average value of the Showalter index from the Hirlam forecast

Showmin – minimum value of the Showalter index from the Hirlam forecast

Sqrt\_thresh – square root of the M5MI threshold

Vtotave – average vertical totals index from the Hirlam forecast

## Appendix 2

### Predictor coefficients of the MOS (severe) thunderstorm forecasts

Runtime (UTC)	Thunderstorms	
0	Constant	-56.50099382779236
	gt2tpr	3.1963064072331413
	capmulma	4.896610301443581E-4
	boydave	0.04651360364184928
	rtcp6ec	0.0023368442714328526
	jeffmax	0.02826693870093056
3	constant	-16.488756241728904
	gt2tpr	0.045715324582763395
	capmulma	7.204963547411438E-4
	jeffmax	0.045715324582763395
6	constant	-16.624036806433825
	capmulma	4.6115684512635307E-4
	jeffave	0.048585156027153346
	rtmaxcp6	0.0017871055887664323
	gt10a7ra	0.3931867500321074
9	constant	-16.095044503802082
	capmulma	5.269602024530871E-4
	jeffave	0.04701578807782779
	rtmaxcp6	0.0024440426334177926
12	constant	-15.964931775196177
	capmulma	3.496048881593764E-4
	jeffave	0.04752941444788049
	gt2tpr	3.0347739857815967
	rtavecp6	0.0033112750603929097
15	constant	-17.47246454217819
	gt2tpr	0.050578417350702266
	rtmaxcp6	0.002568705601129417
	jeffmax	0.050578417350702266
18	constant	-83.35334190530673
	gt2tpr	2.5251912043001403
	capmulma	4.658246598500977E-4
	boydave	0.07997946381087305
	rtmaxcp3	0.0015694814875404997
	ctotmax	0.016921290485116005
21	constant	-61.43971870239851
	gt2tprra	3.5929076246154747

boydave	0.06209492981019245
capemax	0.0011125121270877732
showmin	-0.0545099090500864

Runtime **Severe Thunderstorms**  
(UTC)

0	constant	-10.870188
	gt10at	0.223176
	sqrt_thresh	-0.472886
	ctt_214bin	1.634883
	mjefmax	0.034910
3	constant	1.207466
	Ctt_214bin	1.304319
	Sqrt_thesh	-0.470841
	Gt10a7ra	0.238481
	Showave	-0.079924
	Maxv300	0.005026
6	constant	-93.566034346042
	m5mitha	0.02322326500743422
	boydave	0.08366014618787428
	sqrt_thresh	-0.296291423663039
	shearave	0.015173105740487875
	jeffmin	0.038727005428727236
9	constant	-12.971908221707283
	bradmin	-0.028138225620731986
	cos2dtg	0.0017865218919963209
	sqrt_thresh	-0.3181992309612173
	jeffmin	0.04331605957165632
	M5mi7ra	0.021166129028484894
12	constant	-96.86531324148727
	Boydmax	0.08379241294193356
	jeffave	0.0518352479789672
	sqrt_thresh	-0.22402050180385547
15	constant	-0.232569
	ctt_213precip_20bin	1.680819
	Bradmin	-0.092715
	sqrt_thresh	-0.311483
	Capmulma	0.000507
18	constant	1.135333
	m5mitha	0.007547

	ctt_214bin	1.070882
	Sqrt_thresh	-0.356208
	showave	-0.073381
	gt10a7ra	0.187906
21	constant	0.5157381285710331
	flima9ra	0.2266464127712116
	showmin	-0.11418138239379473
	sqrt_thresh	-0.41345055877164527
	gt2ib7ha	1.5294397397036572

**Severe Thunderstorms**  
**Runtime Excluding CPPs**  
(UTC)

0	constant	0.6295676645048837
	gt10at	0.22011556094906845
	sqrt_thresh	-0.43948665853055524
	sc3	-0.010184806766006306
3	constant	1.703309718242742
	m5mit	0.011560143125450912
	sqrt_thresh	-0.44564293337256405
	showave	-0.0818408711367755
	maxv300	0.003522966649000837
15	constant	-0.20429556618736824
	capmulma	4.8631652005625683E-4
	bradmin	-0.09629222523974193
	sqrt_thresh	-0.30517771998369775
	gt30at	0.6041870883318963
18	constant	0.6792941308051886
	gt10a7ra	0.3275738646608713
	bradmin	-0.07876228655596608
	sqrt_thresh	-0.3241071075530411

**Runtime Severe Thunderstorms**  
(UTC) **Updated KOUW**

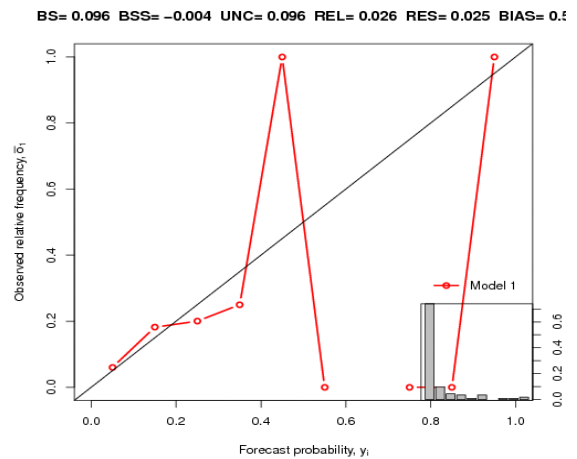
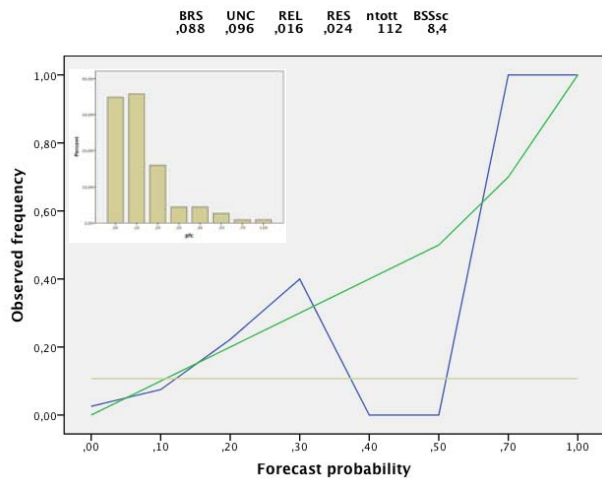
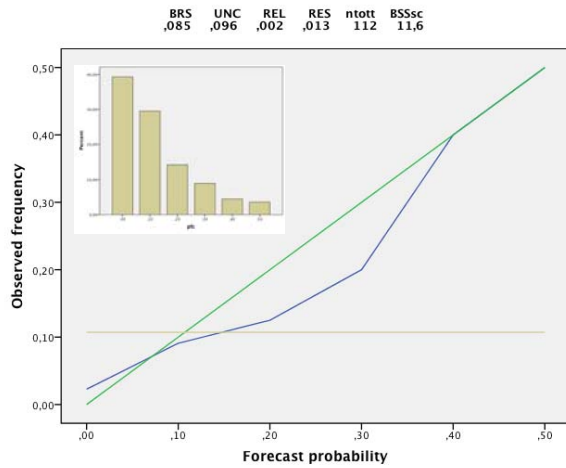
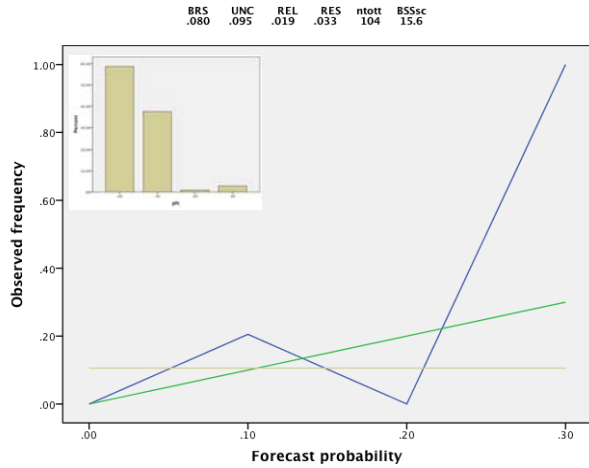
	50	100	200
0 constant	-12.194271613211134	-10.851264834291907	-13.18809996364548
m5mi7ra	0.016547675994604816	0.0033059956576232214	0.0022090211277578007
gt10at	0.09834612040391787	0.13280204993307076	0.3093738921193295
vtotave	0.033453571317185425	0.025277635858491982	0.030361363676639053
gt2tpr	0.9793421778448426	1.1281843241651877	-2.6522126882442696
3 constant	-5.163216250870481	-4.915194487524578	-6.27518682903541
m5mit	0.005981583856967592	0.006012542771149108	0.005480444441790681
gt30at	0.7985386935430917	0.48848342193241395	0.5057011762383355

	INBmulma	2.977503364605196E-5	1.397496163495065E-5	2.2342924086183703E-5
	Rtcp6ec6	0.027988542367335802	0.02554583572475636	0.03147739558501591
6	constant	-0.9227122049482616	-1.4965970391786048	-3.213891862714462
	gt30a7ra	0.9428562709734541	0.5465937195228614	0.797003130052802
	bradmax	-0.11246594371081663	-0.12192969957778452	-0.10463134940162662
	rtcp3ec3	0.0014868183857709028	0.0014633225983113523	0.0034422462576819456
9	constant	-16.793154301046485	-22.98704898224909	-22.08042441540852
	m5mitha	0.011982249700916664	0.016914019499406092	0.0162328556724491
	rtcp3ec3	8.456532819766509E-4	0.0013683073899927783	0.0037126303858542936
	mxt1000a	0.013760071128876792	0.024960476038148067	0.03337553093459597
	cos2dtg	0.0026695223825692186	0.003679728173599178	0.004602132009981552
	jeffmin	0.04174774571815981	0.05381212967928529	0.040292274967386056
12	constant	-6.492840556715094	-9.338507219871193	-12.170953935032754
	bradmin	-0.09477970374211551	-0.13512435277141052	-0.11763708091170967
	gt2tbt	0.6779477675552168	0.5326911021789599	0.7713338078536461
	maxtr850	-4.468401258308514E-4	-1.914888831550085E-4	4.074300400911714E-5
	jeffmin	0.01765033073383006	0.024197702253046738	0.030790711104439844
15	constant	-1.0098375924146032	-2.08142856946431	-3.60146405646244
	flima9ra	0.0673571164989937	0.06583924461089605	0.07137823331694435
	bradave	-0.09545628659979738	-0.1163520389306731	-0.12151362856195427
	capmulav	5.773820834597198E-4	8.144542352494217E-4	0.0010903461550433784
18	constant	-1.0690952194381769	-1.5065362750458071	-3.2514526693020134
	nodis7ra	0.028736951296633024	0.016088033574364797	0.020130308377987505
	bradmax	-0.05509820616928609	-0.0651636206405539	-0.0672876344103906
	gt2ib7ha	1.032311358467471	0.7089340839671974	1.442597838902262
21	constant	-0.2863735628788512	0.556992534941945	-0.47552571716669056
	bradmin	-0.09696871728946521	-0.09282077794266426	-0.11903967458289179
	LNBmax	1.018160045001136E-6	5.118916471080669E-6	2.834046546769096E-6
	Rtff1000	-0.14640827839803527	-0.3569237163705342	-0.46239082188374153

## Appendix 3

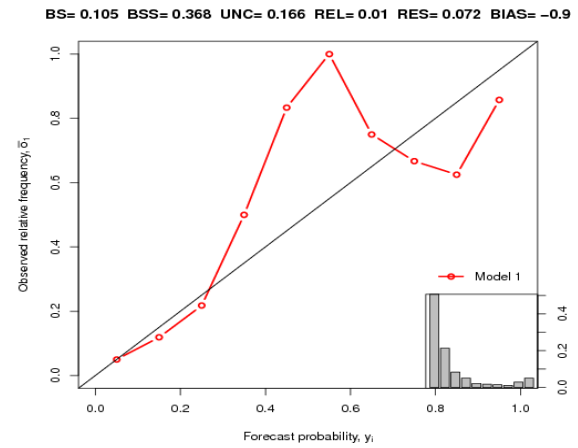
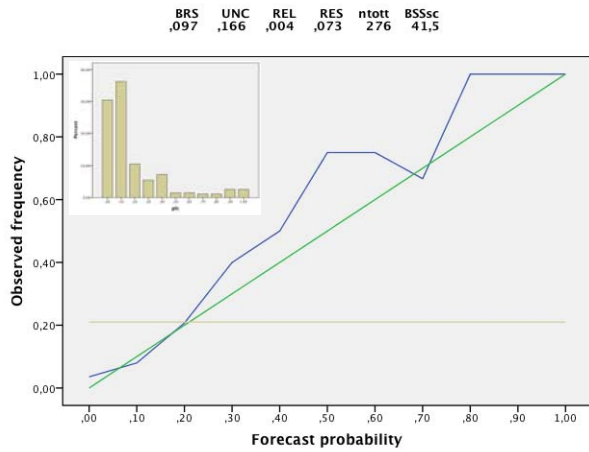
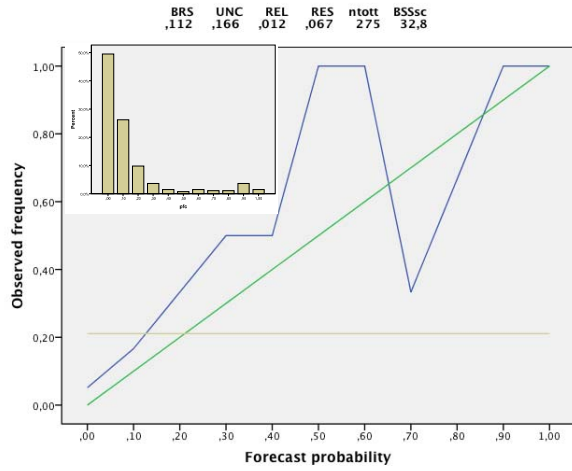
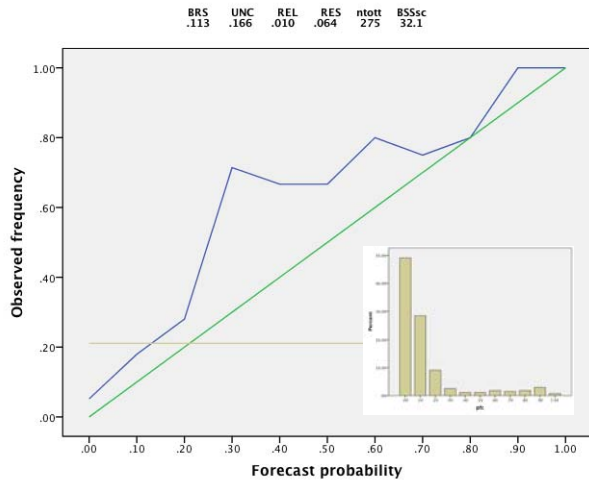
### Reliability diagrams of the MOS severe thunderstorm forecast systems at 03 and 18 UTC central verification time

**00 – 06 UTC forecast for M5MI  $\geq 50$**   
(MOS-CPP, MOS-NoCPP and Updated KOUW from top left to bottom left, respectively)



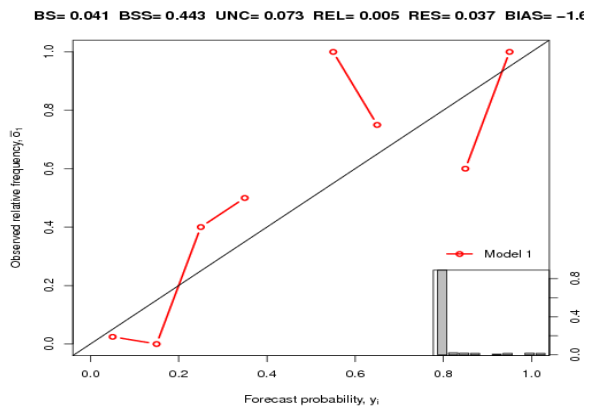
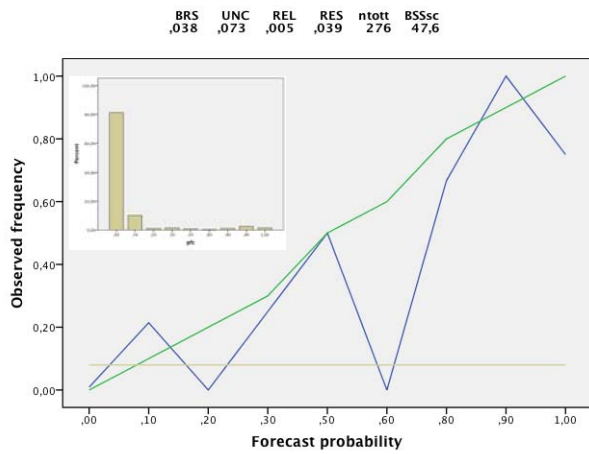
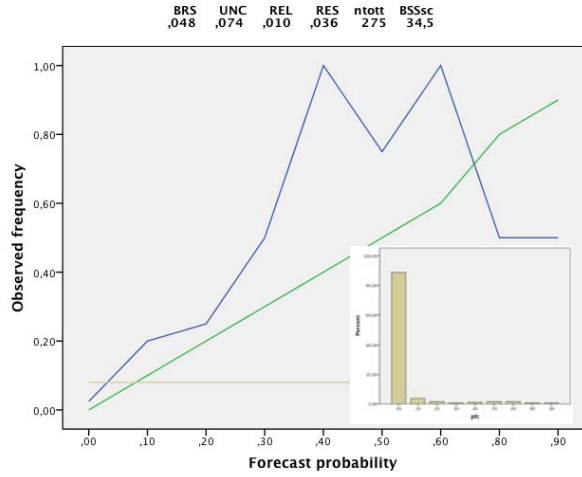
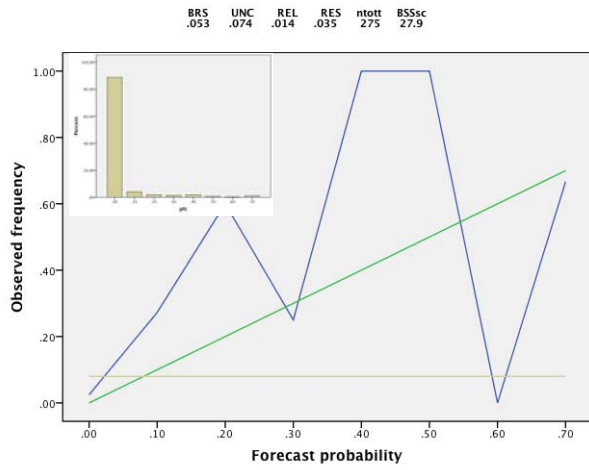
### 15 - 21 UTC forecast for M5MI $\geq 50$

(MOS-CPP, MOS-NoCPP, Updated KOUW and Operational KOUW from top left to bottom right, respectively)



**15 - 21 UTC forecast for M5MI  $\geq 200$**

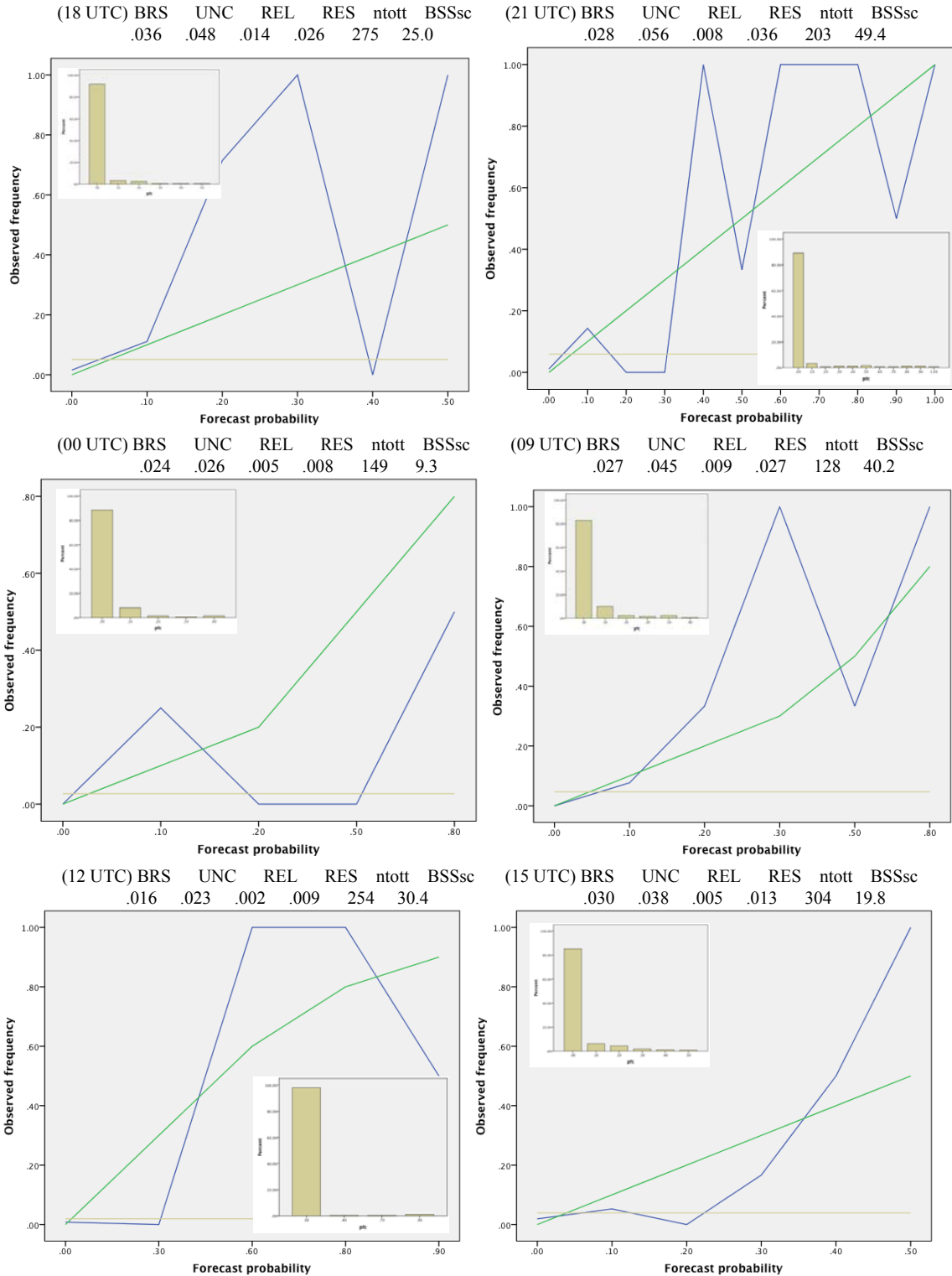
(MOS-CPP, MOS-NoCPP, Updated KOUW and Operational KOUW from top left to bottom right, respectively)



# Appendix 4

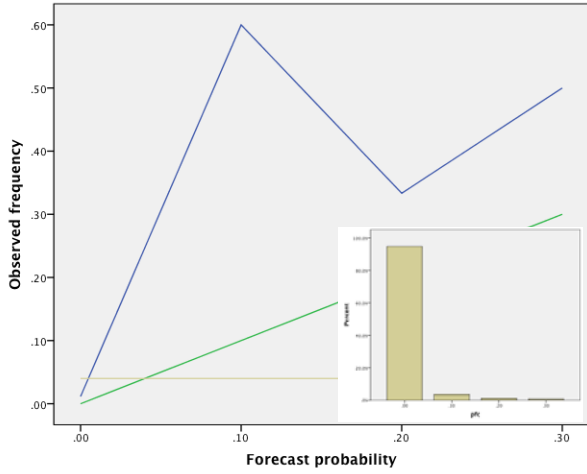
## Reliability diagrams of the MOS severe thunderstorm forecast system for M5MI $\geq$ 300, 400, 500 forecasts

### M5MI $\geq$ 300 forecast for central verification times with BSS > 0

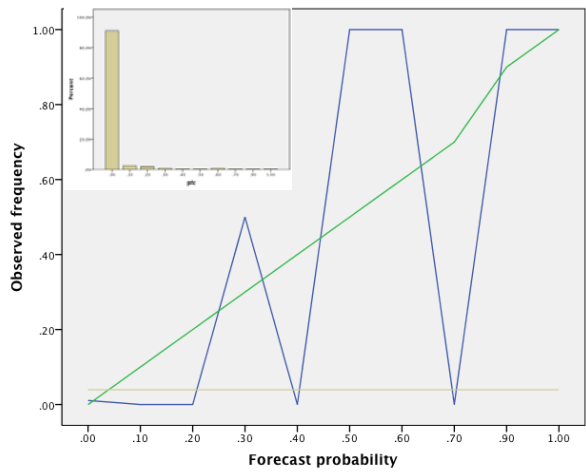


**M5MI  $\geq$  400 forecast for central verification times with BSS > 0**

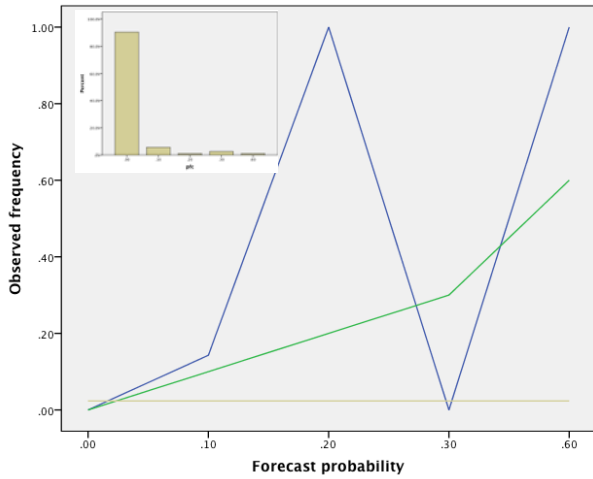
(18 UTC) BRS UNC REL RES ntott BSSsc  
 .033 .038 .010 .015 275 12.9



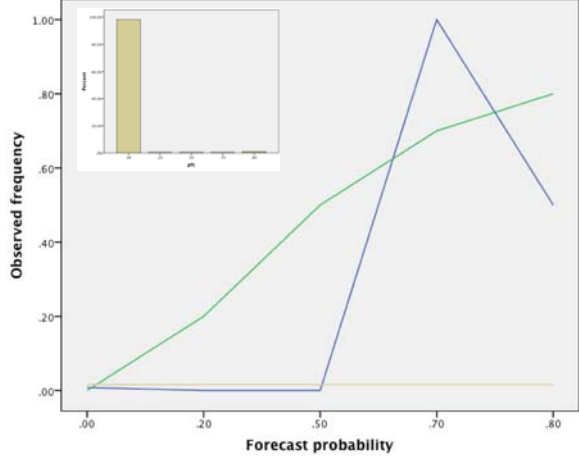
(21UTC) BRS UNC REL RES ntott BSSsc  
 .020 .038 .008 .026 203 47.7



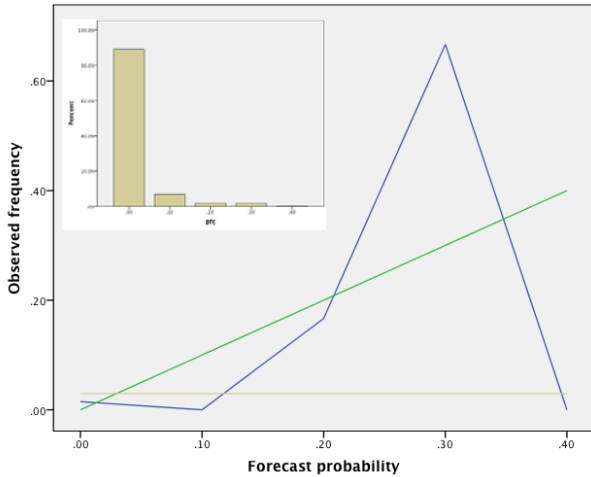
(09 UTC) BRS UNC REL RES ntott BSSsc  
 .015 .023 .008 .016 128 33.8



(12 UTC) BRS UNC REL RES ntott BSSsc  
 .012 .016 .002 .006 254 22.3



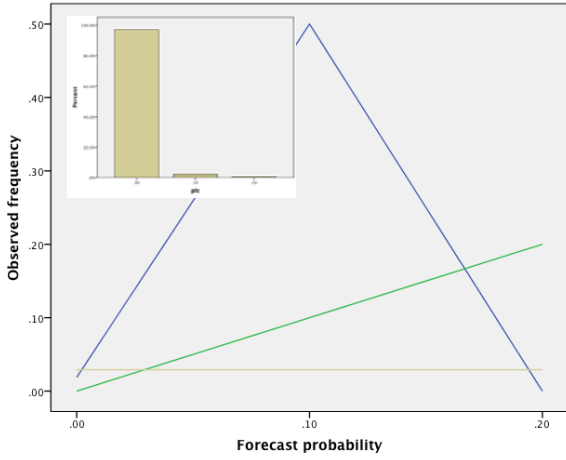
(15 UTC) BRS UNC REL RES ntott BSSsc  
 .024 .029 .004 .009 304 15.8



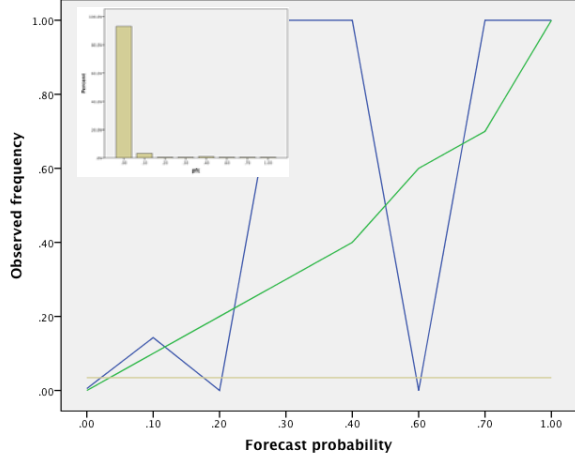
□

**M5MI  $\geq$  500 forecast for central verification times with BSS > 0**

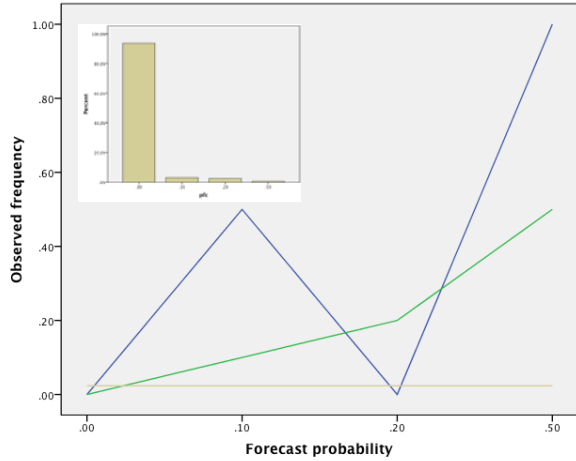
(18 UTC) BRS UNC REL RES ntott BSSsc  
 .027 .028 .004 .005 275 2.9



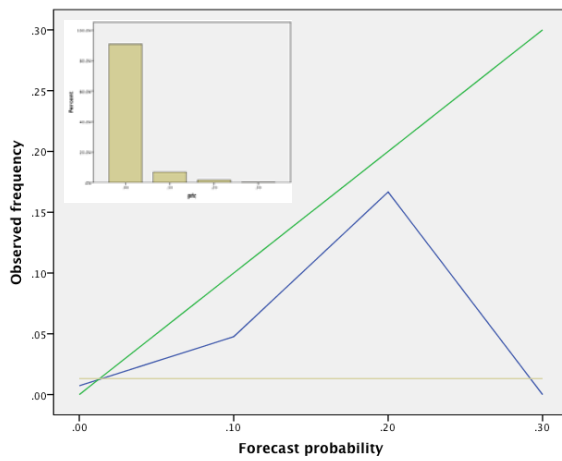
(21 UTC) BRS UNC REL RES ntott BSSsc  
 .018 .033 .008 .024 203 47.2



(09 UTC) BRS UNC REL RES ntott BSSsc  
 .016 .023 .008 .015 128 31.4

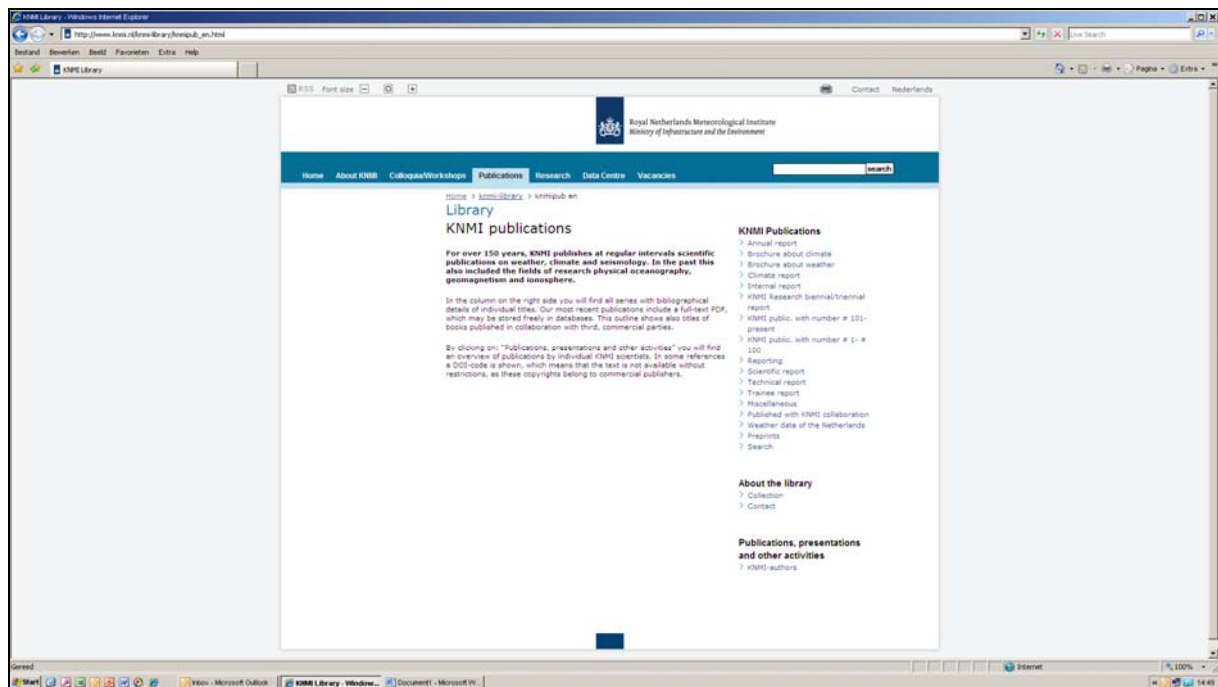


(15 UTC) BRS UNC REL RES ntott BSSsc  
 .013 .013 .001 .001 304 .2



**A complete list of all KNMI -publications (1854 – present) can be found on our website**

[www.knmi.nl/knmi-library/knmipub\\_en.html](http://www.knmi.nl/knmi-library/knmipub_en.html)



**The most recent reports are available as a PDF on this site.**

